Linking and breaking hydrocarbon chains to produce fuels and chemicals

by

Dongting Zhao

A dissertation submitted in partial fulfillment of the requirements for the degree of

Doctor of Philosophy

(Chemical Engineering)

at the

UNIVERSITY OF WISCONSIN-MADISON

2018

Date of final oral examination: February 20, 2018

George W. Huber, Professor, Chemical and Biological Engineering

Ive Hermans, Professor, Chemical and Biological Engineering & Chemistry

Manos Mavrikakis, Professor, Chemical and Biological Engineering

Christos T. Maravelias, Professor, Chemical and Biological Engineering

Reid Van Lehn, Assistant Professor, Chemical and Biological Engineering

ACKNOWLEDGEMENTS

As I complete my PhD study and begin a new journey as an independent researcher, I would like to take this opportunity to express my gratitude towards people that have loved me and supported me.

First and foremost, I am much grateful to my advisors, Professor George W. Huber and Professor Ive Hermans, for providing me with the opportunity to work with them. Their guidance throughout my graduate study is of utmost importance in completing this work. It has been a great honor working with them; I have learned a lot from their immense knowledge in the heterogeneous catalysis field as well as their attitude and passion for research.

I would like to thank Professor Manos Mavrikakis, Professor Christos T. Maravelias and Professor Reid Van Lehn for being on my thesis defense committee and I appreciate their invaluable feedback.

I also would like to thank Carlos Carrero, Zhuoran Xu, Joseph Chada, Xianhua Wang and James Miller for providing valuable technical input to my research work. I have also had the pleasure to be colleagues with Siddarth Krishna, Juan Venegas, Nat Eagen, Jiayue He, Daniel McClelland, Sam Burt, Kevin Barnette, Bo Li, Ling Li, Alessandro Chieregato, Phillip Müller, Sarah Specht, Patrick Wolf, Joseph Grant, Alyssa Love and

Lifeng Zhang. They have influenced me with their excellent research in different aspects of the field of heterogeneous catalysis.

I much appreciate the sponsorship from the Dow Chemical Company as well as the helpful feedback from Devon Rosenfeld and Jessica Rogers in the monthly research meetings.

Finally, my earnest gratitude belongs to my family. They have always supported me in my endeavors and encouraged me to pursue my ambitions.

Dongting Zhao

January 2018

TABLE OF CONTENTS

LIST OF FIGURES

LIST OF TABLES

ABSTRACT

The current olefin oligomerization technology uses homogeneous rather than heterogeneous catalysts, involving expensive and difficult to handle co-catalyst activators, complex catalyst recovery operations, and requiring a highly purified olefin feed stream. Replacing homogeneous catalysts with an efficient heterogeneous analogue could lower the capital and operating cost of olefin oligomerization. Heterogeneous catalysis for olefin oligomerization has been investigated for a number of years. However, heterogeneous catalysts reported so far suffer from poor selectivity to linear products, low activity, and rapid deactivation. In Section I of this thesis, cobalt oxide on N-doped carbon heterogeneous catalysts were studied for 1-butene oligomerization. The effects of pretreatment temperature and ammonia treatment temperature during catalyst synthesis were investigated. The mechanistic pathways for oligomerization of light olefins over this class of catalysts were proposed.

Chapter 2 investigates the effect of catalyst pretreatment temperature on the catalyst activity and active phase. Cobalt oxide on N-doped carbon catalysts were synthesized by treating activated carbon with NH_4OH solution at room temperature prior to cobalt impregnation. After the cobalt impregnation, the catalyst was treated with NH_4OH solution for a second time at 130°C. Linear octenes were produced in high (70−85%) selectivity from oligomerization of liquid 1-butene using cobalt oxide on N-doped carbon catalysts in a continuous flow reactor. The liquid products were characterized by two-

dimensional gas chromatography−mass spectrometry. Over 95% of the oligomers were C8 olefins, with the other products primarily being branched C12 olefins. The selectivity of linear octenes decreased from 84% to 78% as the oligomer yield increased from 10% to 29%. The activated catalyst contained both Co_3O_4 and CoO as confirmed by X-ray diffraction (XRD), *in situ* Raman spectroscopy, and X-ray absorption spectroscopy. The cobalt oxide particle size was estimated to be between 5 and 10 nm by high-resolution transmission electron microscopy and XRD. The Co_3O_4/CoO ratio decreased with increasing pretreatment temperature. Metallic cobalt, which has a low catalytic activity, formed at 550 °C. A Cossee-Arlma insertion mechanism was proposed for light olefin oligomerizations over cobalt oxide on N-doped carbon catalysts.

Chapter 3 investigates the role of nitrogen species within the carbon support in the catalytic activity and active phase. A series of cobalt oxide on N-doped carbon catalysts were synthesized by treating activated carbon with nitric acid and subsequently with NH_3 at 200, 400, 600 and 800 ^oC, followed by impregnation with cobalt. The 1-butene oligomerization selectivity increased with ammonia treatment temperature of the carbon support. The oligomerization selectivity of cobalt oxide on N-doped carbon synthesized at 800 ^oC (800A-CoOx/N-C) is 2.6 times higher than previously reported cobalt oxide on N-doped carbon synthesized with NH_4OH (2A-CoOx/N-C). Over 70% of the butene dimers were linear C8 olefins for all catalysts. The oligomerization selectivity increased with 1-butene conversion. The catalysts were characterized by elemental analysis, nitrogen adsorption, XRD, XAS and XPS. The nitrogen content of the catalysts increases

with ammonia treatment temperature as confirmed by elemental analysis. The surface content of pyridinic nitrogen with a binding energy of 398.4 ± 0.1 eV increased with ammonia treatment temperature as evidenced by deconvolution of N1s XPS spectra. The product distribution confirms that the oligomerization reactions over this class of cobalt oxide on N-doped carbon catalysts follow the proposed Cossee-Arlma insertion mechanism.

Section II of this thesis addresses another concern of the modern society: rapid growth in the production of commodity plastics has resulted in an increase of plastic waste deposition. Pyrolysis of polyethylene (PE) was studied using both TGA and fluidized bed reactor in Chapter 5. A random scission model with two parallel first order random scission reactions was developed to fit the TGA profile. PE pyrolysis in fluidized bed reactor was studied at a temperature range of 500-600 ^{o}C and residence time of 12.4 – 20.4 s. The gas products yield increased from 8.2 wt.% to 56.8 wt.% and the liquid products yield decreased from 81.2 wt.% to 28.5 wt.% as the temperature increased from 500 ^{o}C to 600 ^{o}C. The gas products include hydrogen, C2–C4 alkenes, C1–C4 alkanes and 1,3-butadiene. The liquid products include n-paraffins, iso-paraffins, mono-olefins, cycloalkanes/alkadiene and aromatics. Detailed gas and liquid product analyses revealed the product potential as feedstock to produce fuels and chemicals. The carbon number distribution of the fluidized bed experiments reflected contributions of non-random reaction of random-scission fragments.

Chapter 1. Introduction

1.1 Context and motivation

The annual production of linear alpha-olefins (LAOs) is estimated at 3.5 million metric tons, corresponding to a market value of roughly $5.5 billion as of 2016.[1] LAOs are currently produced by oligomerization of light olefins, like ethylene, in processes that employ expensive and difficult-to-recycle homogeneous transition metal-complex catalysts. Technological advancements in natural gas extraction have increased the US production of ethylene to an all-time high and therefore improved the competitiveness of the LAOs market in the US.[2] The largest uses of LAOs are as co-monomers for production of polyethylene, oxo alcohols (used primarily in detergents) and polyalpha-olefins (used in synthetic lubricants). Polyethylene contains between 2 and 10 wt.% 1-butene, 1-hexene and 1-octene.[1]

Olefin oligomerization remains one of the few industries that use homogeneous catalysts.[3] The technology uses an expensive and difficult-to-handle co-catalyst activator such as methylaluminoxane (MAO), complex catalyst recovery operations, and a highly-purified olefin feed stream.[4] Many researchers have studied the oligomerization of light olefins over heterogeneous catalysts such as zeolites. However, in most cases zeolites produce branched olefins with a few selected reports of linear selectivities of less than 40%.[5-7] Moreover, heterogeneous catalysts suffer from low activity and rapid deactivation compared to industrial homogeneous catalysts. Replacing homogeneous

catalysts with an efficient heterogeneous analogue could drastically lower the capital and operating costs, and hence improve the competitiveness of the US chemical industry.

As the demand for plastics production grows, the rapid growth of commodity plastics production since 1950s has surpassed most other man-made materials. Global plastic production has increased by 620% since 1975 and reached 288 million metric tons (Mt) in 2012.[8,9] As a result, the share of plastics in municipal solid waste increased from less than 1 wt.% in 1960 to more than 10 wt.% by 2005 in middle and high-income countries.[10] It was estimated that between 1950 and 2015 a total of 8,300 Mt of plastics had been produced with 6,300 Mt of plastic waste. Only 9% of these plastic waste has been recycled, 12% incinerated, and 79% was accumulated in landfills or the natural environment.[10] The accumulation of near-permanent plastic waste contamination is a growing concern. There is a critical society need to develop an economical technology that can efficiently re-use waste plastics.

1.2 Thesis scope

This thesis is divided into two sections to address the two issues above. Section I focuses on the oligomerization of light olefins over cobalt oxide on N-doped carbon heterogeneous catalysts. A combined approach that employs catalyst design, kinetics measurement and catalyst characterization is demonstrated throughout this section. Chapter 2 introduces the class of N-doped carbon catalysts for light olefin

oligomerization with high linear selectivity towards linear oligomers. The effect of pretreatment temperature on the oligomerization yield was investigated and explained by systematic characterization of the catalysts. A mechanistic pathway for oligomerization of light olefins over this class of catalysts were proposed based on the product distribution. Chapter 3 focuses on the role of nitrogen species in the active sites and catalytic activity. Improved catalyst activity was achieved by N-doping technique, and more importantly, the explanation of this correlation opens up other possibilities for further improvement of heterogeneous catalysts for light olefin oligomerization reaction.

Section II of this thesis addresses the concern of the rapid growth of the commodity plastics production and the resulting increase of plastic waste deposition. A combination of experimental and modelling aspects was implemented in this section. Pyrolysis of polyethylene (PE) was studied in Chapter 5 using both TGA and fluidized bed reactor. This chapter aims to explore the PE pyrolysis product potential as well as develop a kinetic model to describe the thermal degradation of polymers in terms of “intrinsic” kinetics.

Chapter 4 and Chapter 6 summarize the key findings of the two topics of this thesis study, as well as the author’s proposed future work in the research areas.

SECTION I: OLIGOMERIZATION OF LIGHT OLEFINS OVER COBALT OXIDE ON N-DOPED CARBON HETEROGENEOUS CATALYSTS

Chapter 2. 1-Butene Oligomerization over Cobalt Oxide on N-doped Carbon Catalysts – Effect of Pretreatment Temperature

Z. Xu, J. P. Chada, D. Zhao, C. A. Carrero, Y. T. Kim, D. C. Rosenfeld, J. L. Rogers, S. J. Rozeveld, I. Hermans, and G. W. Huber, 'Production of Linear Octenes from Oligomerization of 1-Butene over Carbon-Supported Cobalt Catalysts', *ACS Catalysis,* 6 (2016), 3815-25.

2.1 Introduction

The United States' production of natural gas has increased by 35% in the past decade due to large-scale implementation of hydraulic fracturing technology.[11] Steam cracking of the recovered C2 plus portion of the natural gas produces olefins. In the next four years, six new steam crackers are scheduled to be constructed in North America due to the abundance of low cost shale gas. These new olefin streams provide a valuable feedstock that can be used to make a variety of commodity chemicals including linear alpha olefins (LAOs). LAOs are important co-monomers in the production of polyethylene, plasticizers and surfactants.[12] The industrial production of linear alpha olefins is from polymerization of ethylene through organometallic catalysis, such as the SHOP (Ni complex) and Gulf (triethyl-aluminum) processes.[13,14] The production of linear alpha olefins typically involve homogeneous catalysts that consist of transition metals, such as Co, Fe and Cr, that produce a distribution of linear alpha olefins that range from C4 to polyethylene from a highly purified olefin feedstock (≥99% percent feed).[12,15,16] These processes produce mixtures that follow the Schultz-Flory distribution. Although several other systems have been studied for alpha olefin oligomerization, they tend to produce branched products. Solid heterogeneous catalysts have several advantages over homogeneous catalysts including: recyclability, the ability to handle olefins containing more impurities, the ability to better control the olefin chain growth, and no co-catalyst is required for activation.

Solid acid catalysts, including zeolites and solid phosphoric acids, have been used for olefin oligomerization.[17-21] These catalysts primarily produce branched olefin oligomers along with paraffins and cycloalkenes. Some researchers have observed low selectivities of linear octenes (31-37%) from butene oligomers over Co,Na,Ca-Y and HNaNi-ZSM-5[5,7] at a conversion between 70-90% and 65%, respectively. However, the production of olefins over Brønsted acid catalysts primarily forms branched species due to the higher stability of the internal (secondary and tertiary) carbocation *vs*. the primary carbocation required for linear olefin formation. Production of linear octene using acid catalysts requires the formation of primary carbocations. We have previously studied 1-butene oligomerization on H-ferrierite and observed that the predominant products are dimethyl-hexenes, which are derived from secondary carbocation transition states.[18]

Supported nickel oxide and cobalt oxide have also been used for oligomerization of short olefins such as ethylene, propylene, butene and hexene into longer chain olefins. Chauvin *et al.* reported that $NiCl_2/Al_2O_3$ after calcination at 500 ^oC in air was able to oligomerize propylene in liquid phase with 97.4% conversion and 18% *n*-hexene selectivity with the rest of the products being mono- and di-methyl branched dimers.[22] The low selectivity of linear hexenes was reported to be due to Lewis- and Brønsted-acid sites induced by the residual chloride ions.[22] A later patent reported that metal oxide supports and alkali metal doping with NiO produced *n*-octenes at 25% from butene oligomerization between 180 and 210 ^oC.[23]

Schultz *et al*. demonstrated that cobalt oxide on carbon catalysts were selective for dimerization of propylene, 1-butene and 1-hexene at 150 ^{o}C into linear olefins with selectivity of 52, 65, and 83% respectively.[24,25] The catalyst was prepared by impregnating activated carbon with cobalt nitrate solution, with the carbon wetted with NH_4OH both before and after the impregnation. The authors hypothesized that the active site was a cobalt hydride (Co(II)-H) species, as determined by a chemical titration method using wet techniques, formed after the addition of NH_4OH during catalyst synthesis. The authors reported that the cobalt hydride species was thermally sensitive and was destroyed by heating at moderate temperatures (275-350 ^{o}C). The authors used catalytic hydrogenation followed by GC to identify the compounds in the product mixture. Hydrogenation of these products prior to GC analysis removes the ability to confirm the formation of olefin products, or to identify the location of the double bond.

This chapter of the thesis investigates 1-butene oligomerization over cobalt on carbon catalysts including the identification and quantification of all of the products by 2D-GC, assessing catalyst stability in a continuous flow reactor and identifying the catalytically active site through the use of advanced characterization tools. A Cossee-Arlman insertion mechanism was proposed based on the product distribution.

2.2 Experimental

2.2.1 Catalyst preparation

Cobalt on carbon catalysts were prepared by impregnating 5 g of sieved activated carbon (Norit, Darco MRXm-1721, BET surface area: 600-800 m^2/g, 250-600 μm particle size) with a cobalt nitrate solution composed of 4.7 g $Co(NO_3)_2 \cdot 6H_2O$ (Sigma Aldrich) in 5.8 mL DI water. 2A-CoOx/N-C-XXX was prepared by treating the carbon with 4.6 ml of 30% NH_4OH solution at room temperature for 0.5 h prior to cobalt impregnation. After the cobalt impregnation, the sample was then dried on a hot plate at 130 ^oC overnight. Another 12.5 ml of 30% NH_4OH solution was dropped onto the sample and the sample was dried overnight again on a hot plate at 130 ^oC. XXX represents the pretreatment temperature for the catalyst.

2.2.2 Catalyst characterization

Powder X-ray diffraction (pXRD) patterns were collected with a Rigaku Rapid II diffractometer with Mo K_α source from 2^o to 45^o using a total exposure time of 30 min. Samples were packed in glass capillaries with 0.8 mm diameter and 0.01 mm thickness. Phase identification and crystallite size estimation were carried out using JADE 9 software. The Co_3O_4 crystallite size was calculated from the broadness of the cobalt spinel (311) peak at $2\theta=16.79°$. Samples for XRD were pretreated in flowing helium at 150

mL/min with 5.5 ºC/min ramp rate and held at a specified temperature for 2 h before the XRD measurements.

Atomic compositions for Co, H, C and N of the pretreated catalysts were determined by Galbraith Laboratories (Knoxville, TN). Thermogravimetric analysis (TGA) of the catalysts was performed with a TA instrument Q500 system. For these experiments, approximately 20 mg of sample was loaded onto a Pt pan in 80 mL/min nitrogen flow with 10 ºC/min ramp rate from room temperature to 100 ºC and held for 30 min, and then ramped to 800 ºC.

The Raman spectra were obtained with a dispersive Renishaw InVia Raman spectrometer equipped with 785, 514, and 325 nm (excitation) lasers. For this study, all measurements used a 2400 l mm^{-1} grating with an efficiency of approximately 100% at 514 nm. For *in situ* Raman studies an Olympus LMPlanFLN objective with 50× magnification and a working distance of 10.6 mm was used. The Raman was calibrated daily to an internal Si standard at 520.7 cm^{-1}. The spectra were taken with a range of 200-1200 cm^{-1} and a dispersion of 1.36565 cm^{-1} $pixel^{-1}$. *In situ* measurements were taken with a fully open aperture and a 20 s exposure time, with two accumulations. Typically, 5-10 mg of sample was placed into a Linkam CCR1000 cell. The temperature was controlled by a Linkam T95-HT system and the heating ramp was kept at 5.5 °C min^{-1}, same as that during pretreatment in the continuous flow reactor. A flow rate of 10 mL min^{-1} helium (Airgas, UHP) was used for *in situ* pretreatment of the catalyst. The spectra used in this study were taken at various temperatures during the *in situ* pretreatment. Raman spectra

of Co_3O_4, CoO and $Co(NO_3)_2$ bulk materials were taken at room temperature using a Leica N Plan EPI objective with 20× magnification and a working distance of 1.15 mm. The background was first subtracted from each spectrum and the resulting spectra were normalized to the area of the carbon signal at 1600 cm^{-1}.

X-ray absorption spectroscopy (XAS) measurements were taken at beamline 10-BM of the Advanced Photon Source (APS) at Argonne National lab (Lemont, IL). CoOx/N-C samples were crushed and diluted with boron nitride (Sigma-Aldrich). Self-supporting pellets were pressed inside a 4 mm I.D. stainless steel cylindrical sample holder. Sample weights were calculated to give an edge step of ~1. To allow for measurement without exposure to atmospheric conditions, the stainless steel holder was sealed in a 1'' O.D. Kapton-windowed quartz tube fitted with Swagelok valves. The sealed sample was pretreated in a tube furnace while the sample tube was continually purged with helium. After pretreatment, valves on the pretreatment tube were sealed and the samples were placed in the X-ray beam. Samples pretreated at 230 ^oC and 270 ^oC were analyzed without exposure to air. Samples pretreated at 350 ^oC, 550 ^oC and cobalt standards were exposed to air at room temperature prior to analysis. XAS measurements of the Co K-edge (7.709 keV) were collected in transmission mode. X-ray absorption was measured with gas ionization chambers before and after the sample holder. Energy calibration was performed with a Co reference foil after the sample chamber. Oxidation states were quantified by comparison of the x-ray absorption near edge structure (XANES) with the

experimental standards. CoOx/N-C samples were fit with a linear combination of Co foil, CoO, and Co_3O_4 in the range of -30 to +20 eV from the Co edge energy.

The transmission electron microscopy (TEM) images were obtained using a JEOL 2010F field emission gun (FEG) transmission electron microscope. The TEM was operated at an accelerating voltage 200 keV. Conventional TEM images were recorded using a Gatan multi-scan digital camera (Model Ultrascan 1000) with a CCD size of 2048 pixels × 2048 pixels.

2.2.3 Catalytic measurement

1-Butene oligomerization reactions were carried out in a down-flow fixed-bed reactor with the liquid product analyzed by a comprehensive two-dimensional gas chromatograph-mass spectrometer (2D-GC-MS) as described by our earlier work.[18] The C4 compounds in the liquid or gas products were analyzed via conventional gas chromatography (GC-FID, Shimadzu). Skeletal composition of the product mixture was verified separately by hydrogenating the liquid product prior to analysis by 2D-GC-MS. Approximately 100 mg of Pd/C catalyst was packed into the GC liner for hydrogenation. Only two C8 products were observed after hydrogenation, which are 3-methyl-heptane and *n*-octane, respectively; all the detectable hydrogenated C12 products were branched species. The thermodynamic equilibrium composition calculations were based on Benson group thermodynamic data from Alberty and Gehrig [26] by assuming that pressure has little effect on the change of the physical property of the compounds. The equilibrium

concentrations were solved by setting the change of Gibbs free energy to zero ($G_{353k}(i)=0$) for isomerization reaction between the isomers. The following octene standards were tested for our product analysis: 1-octene, *trans*-2-octene, *cis*-2-octene, 2-methyl-1-heptene, 2-methyl-2-heptene, trans-2-methyl-3-heptene, trans-6-methyl-3-heptene, 2,3-dimethyl-2-hexene, 2,3-dimethyl-3-hexene, 2,3,4-trimethyl-2-pentene, 2,4,4-trimethyl-2-pentene (Sigma-Aldrich), cis-2,5-dimethyl-3-hexene (Pfaltz & Bauer) cis-3-octene, trans-3-octene, cis-4-octene, trans-4-octene, 3-methyl-2-heptene, 3-methyl-3-heptene, 5-methyl-2-heptene, 5-methyl-3-heptene, 3,4-dimethyl-2-hexene (ChemSampCo). For all the catalytic testing, 0.5 g of the catalyst particles were packed into the tubular reactor without diluents. The catalysts were pretreated in 150 mL/min flow of helium with 5.5 ^{o}C/min ramp rate and held at the pretreatment temperature for 2 h before the reactor was cooled to reaction temperature. 1-Butene (99.9%, Matheson) was fed into the reactor at reaction pressure (450 psig) through a high-pressure syringe pump (500D, Teledyne Isco). The liquid samples were collected in a 50 mL glass pressure tube pre-chilled in dry ice filled with approximately 10 g of 0.5 wt.% heptane in hexane solvent. The variation of weight hourly space velocity (WHSV=hourly mass liquid feed flow rate (g/h)/catalyst mass (g)) was achieved by adjusting the butene flow rate at the inlet. After reaction, the spent catalysts were recovered from the reactor and exposed to the air before XRD characterization.

The oligomer yield was calculated according to Eq. 1. Butene consumption rate was calculated according to Eq. 2. The number of chain branches (NCB) was calculated

according to Eq. 3. Total C4 dimer distribution, total linear octene distribution were calculated using Eq. 4 and 5, respectively.

$$\textit{Oligomer yield (\%)} = \frac{mols\ of\ carbon\ in\ the\ detected\ products}{mols\ of\ carbon\ in\ the\ feed\ butene} \times 100\%$$

(Eq. 1)

$$\textit{Oligomer production rate (molbutene/molCo/h)} = \frac{butene\ inlet\ flow\ rate \times oligomer\ yield}{mol\ cobalt\ in\ the\ catalyst}$$

(Eq. 2)

$$NCB = [0 \times linear\ octene\ distribution\ (\%) + 1 \times methyl\text{-}heptene\ distribution\ (\%) + 2 \times dimethyl\text{-}hexene\ distribution\ (\%)]$$

(Eq. 3)

Total C4 dimer distribution (%) =

$$\frac{carbon\ moles\ in\ the\ C8\ olefins}{sum\ of\ carbon\ moles\ in\ all\ the\ detected\ products} \times 100\%$$

(Eq. 4)

$$\textit{Total linear octene distribution (\%)} = \frac{moles\ of\ linear\ octene}{moles\ of\ total\ C8\ olefins} \times 100\%$$

(Eq. 5)

2.3 Results and discussion

2.3.1 Oligomer product selectivity

The 2D-GC revealed over 94% of the non C4 products were octenes for all catalysts used in this study as shown in Table 1. The non octene products were branched C12 olefins. A small amount of C16 olefins (0.3% selectivity) was observed for the 2A-CoOx/N-C-230 catalyst run at the lowest WHSV (0.25 h^{-1}). Octene isomer identification was carried out by matching the location of the product trace in the 2D-GC image with that of standards. Hydrogenation of our product mixture and analysis with Pd/C showed that our products only contained *n*-octenes and methyl-heptenes corroborating our assignments made using the 2D-GC. The *trans* and *cis* isomers of 3-octene and 4-octene were indistinguishable. The only methyl-heptene isomers observed were 5-methyl-heptenes and 3-methyl-heptenes. The analytical technique used in this study allowed us to gain specific insight into the chemical structure of the product compounds compared to previous studies, which aided in the derivation of a reaction mechanism.

As shown in Table 1 between 77 to 90% of the products were linear octenes, which is higher than previous studies (about 65%).[25] Only minor amounts of 1-octene (less than 1%) were observed. At low WHSV the linear octene products in decreasing abundance were 3-octene > *trans*-2-octene> *cis*-2-octene > 4-octene. The 3-octene and *cis*-2-octene distribution decreases and the 4-octene distribution increases with oligomer yield. It is likely that the C8 products tend to approach equilibrium of octene isomers (Table 2) at

higher oligomer yield. Aside from linear octenes, all four catalysts produced *trans*-3-methyl-2-heptene, *trans*- and *cis*-5-methyl-3-heptene, and *trans*- and *cis*-5-methyl-2-heptene. No alpha methyl-heptene products were detected. The octene product distribution is similar among the four different catalysts.

Table 1. Average product selectivity for butene oligomerization (Reaction conditions: 80ºC, 450 psig.)

Catalyst	2A-CoOx/N-C-230			2A-CoOx/N-C-270			2A-CoOx/N-C-350	
WHSV(h^{-1})	14.14	0.71	0.25	14.14	0.71	0.25	14.14	0.71
TOS/h	40	94	37	40	91	35	40	75
Oligomer yield (%)	9.77	11.42	29.00	3.94	5.74	21.4	1.27	6.74
Total C4 dimer selectivity (%)	98.5	96.6	94.4	98.7	96.6	97.6	99.6	97.6
Total C12 selectivity (%)	1.5	3.4	5.3[a]	1.3	3.4	2.3[b]	0.4	2.4
Specific C4 dimer distribution(%)								
cis-2-octene	12.3	7.1	6.9	11.6	6.02	12.8	7.75	5.3
trans-2-octene	17.7	19.7	19.8	17.3	16.9	17.6	24.66	16.4
cis/trans-3-octene	52.9	45.4	43.9	52.5	42.5	54.7	46.08	39.6
cis/trans-4-octene	1.3	5.3	7.7	1.4	8.7	2.2	5.42	13.4
cis-5-methyl-3-heptene	1.7	2.2	1.8	2.2	2.7	1.5	1.65	1.0
trans- 5-methyl-3-heptene	1.9	2.5	2.7	2.0	2.9	2.2	1.97	3.2
trans-3-methyl-2-heptene	3.3	9.8	9.6	4.9	12.3	3.6	5.58	12.7
trans-5-methyl-2-heptene	2.6	4.0	4.3	3.2	4.6	2.7	3.40	5.0
cis-5-methyl-2-heptene	6.1	4.0	3.2	5.9	3.4	2.8	3.3	2.8
NCB	0.16	0.23	0.21	0.18	0.26	0.14	0.16	0.25
Total linear octene distribution (%)	84.2	77.5	78.4	82.8	74.1	87.2	83.9	74.7
Carbon balance (%)	90.4	103.2	98.3	89.4	90.3	104.2	96.5	103.6

a. C16 olefin was also observed with 0.3% selectivity.
b. C16 olefin was also observed with 0.1% selectivity.

Table 2. Experimental and Equilibrium linear octene distribution (%) (Reaction conditions: 80ºC, 450 psig)

	2A-Co/C-230			Equilibrium
WHSV(h^{-1})	14.14	0.71	0.25	
Oligomer yield (%)	9.77	11.42	29	
1-octene	0	0	0	0.83
cis-2-octene	14.61	9.16	8.81	8.49
trans-2-octene	21.02	25.42	25.29	35.25
cis/*trans*-3-octene	62.83	58.58	56.07	34.76
cis/*trans*-4-octene	1.54	6.84	9.83	20.67
cis-2-octene/*trans*-2-octene	0.69	0.36	0.35	0.24

Figure 1 shows the octene product distribution as a function of time on stream for 2A-CoOx/N-C-270. Similar trends were observed for all the other catalysts (Figure A1-A3). The octene distribution was nearly constant at 14.14 h^{-1} WHSV even though the oligomer yield was slightly decreasing during this time (see Figure 2a). At lower WHSV of 0.71 h^{-1}, the selectivity of linear octenes, except *trans*-4-octene, decreases and the selectivity of *trans*-3-methyl-2-heptene increases with time on stream.

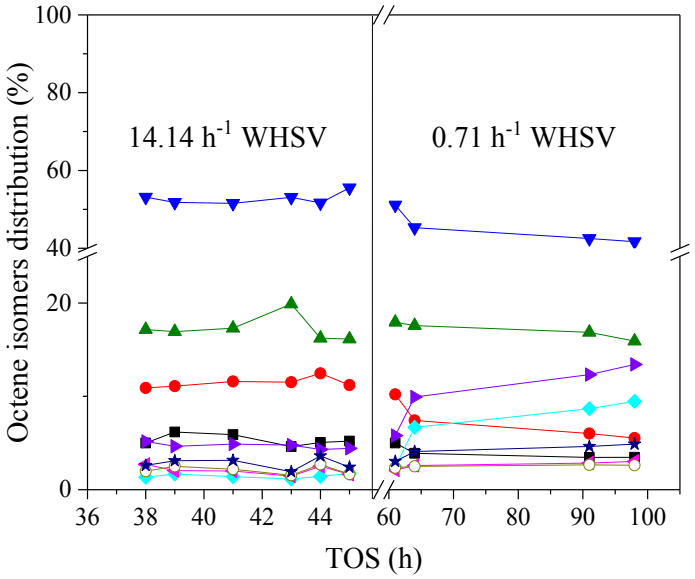

Figure 1. Octene isomers distribution with time on stream over 2A-CoOx/N-C-270, including: (▼) *trans*-3-octene, (▲) *trans*-2-octene, (●) cis-2-octene, (■) *cis*-5-methyl-2-heptene, (►) 3-methyl-2-heptene, (◆) *trans*-4-octene, (◄) *trans*-5-methyl-3-heptene, (○) *cis*-5-methyl-3-heptene and (★) *trans*-5-methyl-2-heptene at 80 ^{o}C and 450 psig.

The hydrocarbon selectivity we determined is fairly consistent with the analyses of Schultz *et al*. who reported a hydrogenated mixture composition of 65.3% *n*-octane, 34.4% 3-methyl-heptane and 0.3% 3,4-dimethyl-hexane at 13.6% oligomer yield.[25] Key differences are that we did not observe the formation of dimethyl-hexene and the selectivity to linear octene was 8.8-21.9% higher in our study. The observed linear octene selectivity was also higher compared to the ion-exchanged zeolites (below 40%).[5,7] Unlike olefin oligomerization with homogeneous catalysts, no 1-octene was detected.[12,13,15,16]

2.3.2 Catalytic activity

The effect of pretreatment on the catalytic activity was studied by activating the catalyst at different temperatures in helium. Figure 2a and Figure 2b compare the butene consumption rate of 2A-CoOx/N-C-230, 2A-CoOx/N-C-270, 2A-CoOx/N-C-350 and 2A-CoOx/N-C-550 catalysts at 14.14 h^{-1} and 0.71 h^{-1} WHSV, respectively. All catalysts were tested by the following reaction sequence: 0.71 h^{-1} WHSV for approximately 36 h, then 10 h of operation at 14.14 h^{-1} WHSV, followed by 40 h of operation at 0.71 h^{-1}. Rapid catalyst deactivation was observed if the catalyst was tested starting at the higher WHSV.

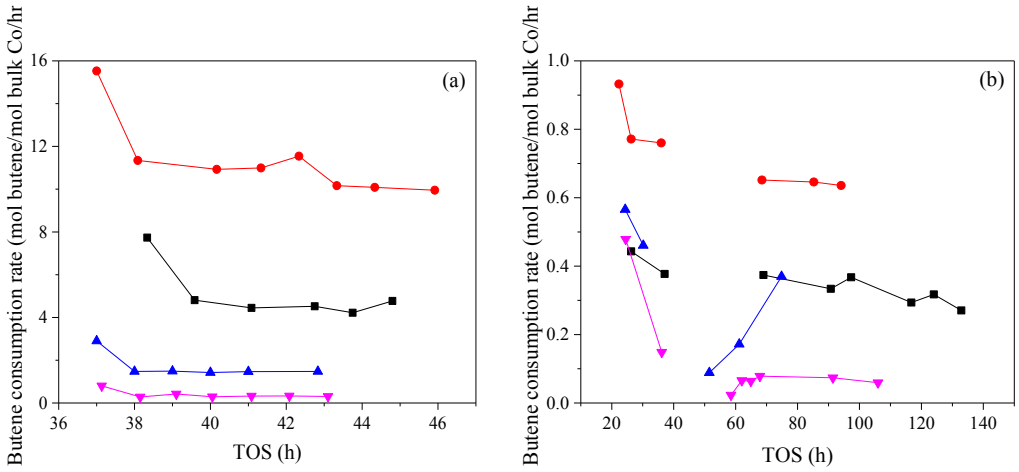

Figure 2. Butene consumption rate as a function of time on stream for (●) 2A-CoOx/N-C-230, (■) 2A-CoOx/N-C-270, (▲) 2A-CoOx/N-C-350 and (▼) 2A-CoOx/N-C-550, at (a) 14.14 h^{-1} WHSV and (b) 0.71 h^{-1} WHSV. Reaction conditions: 1-butene feed, 450 psig, 80 ºC

Average oligomer yield, deactivation rate and average butene consumption rate for each catalyst are summarized in Table 3 at both space velocities. At 14.14 h^{-1} WHSV, the activity of the catalysts decreased with increasing pretreatment temperature. It is worth noting that by lowering the pretreatment temperature from 270 to 230 ^{o}C, the reaction rate doubled. A steady catalytic performance was observed for each catalyst after the first sampling point. The average rate for each catalyst decreased at a lower WHSV of 0.71 h^{-1} (Figure 2b). 2A-CoOx/N-C-230 is the most active catalyst at both 14.14 and 0.71 h^{-1} WHSV. A slow deactivation was observed at the higher WHSV with 2A-CoOx/N-C-230 while no deactivation was observed with the other catalysts. At the lower WHSV, a much slower deactivation rate was observed.

Table 3. Average reaction rates and deactivation rates for 1-butene oligomerization. Reaction conditions: 1-butene feed, 450 psig, 80 °C, 14.14 h^{-1} and 0.71 h^{-1} WHSV

Catalyst	14.14 h^{-1} WHSV			0.71 h^{-1} WHSV		
	Average oligomer yield (%) [a]	Deactivation rate at steady state (h^{-2}) [b]	Average rate ($mol_{butene}/mol_{Co}/h$) [c]	Average oligomer yield (%) [a]	Deactivation rate (h^{-2}) [b]	Average rate ($mol_{butene}/mol_{Co}/h$) [c]
2A-CoOx/N-C-230	10.11	0.19±0.07	10.78	13.10	$(3.20\pm0.89)\times10^{-3}$	0.73
2A-CoOx/N-C-270	5.08	-	5.08	6.06	$(1.26\pm0.23)\times10^{-3}$	0.35
2A-CoOx/N-C-350	1.50	-	1.71	6.02	N.A.	0.33
2A-CoOx/N-C-550	0.36	-	0.39	2.20	$(3.53\pm1.51)\times10^{-3}$	0.12

a, c. Mathematical average of the data taken with TOS shown in Figure 2a (14.14 h^{-1}) and Figure 2b (0.71 h^{-1}).
b. The value of the slope calculated from Figure 2a except for the first sampling point.
c. The value of the slope calculated from Figure 2b, accounting for all the data points collected.

The butene distribution is shown in Figure 3 for 2A-CoOx/N-C-230. At the higher WHSV (Figure 3a) these products were not in thermodynamic equilibrium with 1-butene being the main butene isomer. The three butene isomers deviate further from their equilibrium compositions with increasing time-on-stream. At 0.71 h^{-1} WHSV the butene isomers were in thermodynamic equilibrium as shown in Figure 3b. Schultz *et al.* also observed isomerization of 1-butene to *cis*- and *trans*-2-butene during 1-butene dimerization in a batch reactor,[25] with the butene isomers compositions close to their equilibrium (10.6% 1-butene, 31.1% *cis*-2-butene and 58.2% *trans*-2-butene).

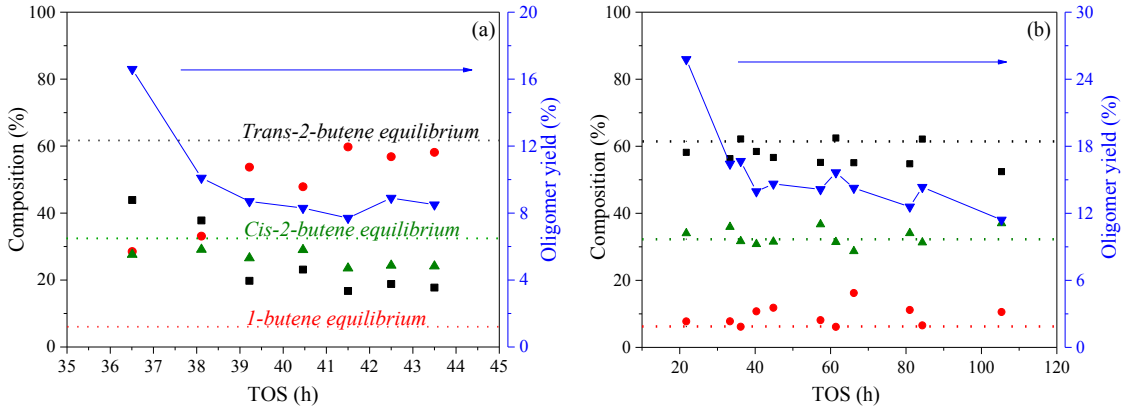

Figure 3. Total butenes oligomer yield (▼) and C4 olefin distribution as a function of time on stream: (■) *trans*-2-butene, (●) 1-butene, (▲) *cis*-2-butene, and butene distribution equilibrium (dotted lines) at 80 ºC, 450 psig, 1-butene feed at (a) 14.14 h^{-1} WHSV (b) at 0.71 h^{-1} WHSV over 2A-CoOx/N-C-230.

The absence of heat and mass transport limitations were verified by commonly-accepted calculations for heterogeneous catalysts systems.[23] Heat effects due to interphase, interparticle and intraparticle heat transport were evaluated. The heat of reaction (42 kJ/mol) was determined from the heat of formation of reactants and products at reaction temperature. An activation energy (E_a) of 70 kJ/mol was used based on the work of Toch *et al*. for ethylene oligomerization.[27] The heat transfer coefficient (300 W $m^{-1}K^{-1}$) for the liquid-phase was determined by assuming a stagnant hydrocarbon film. The thermal conductivity of the catalyst was estimated to be the same as the carbon support (0.1Wm^{-2} K^{-1}). An energy balance of the heat generated and removed showed a negligible temperature rise between the bulk phase and the catalyst surface.

For mass transfer effects, it was assumed that diffusion within the porous support or interparticle mass transport would be the limiting regime. The Weisz-Prater criterion was evaluated to ensure the absence of concentration gradients within the catalyst particles. In the absence of an absolute value for the diffusivity of liquid-phase 1-butene through its oligomer products, the diffusivity was estimated to be within the range of liquid systems (8×10^{-6} cm^2/s). The concentration of 1-butene at the surface of the particle was conservatively estimated to be 80% of the concentration in the unreacted stream. Based on the calculations (Table 4), the reaction is not limited by transport phenomena for the data collected in this paper.[28]

Table 4. Mass and heat transfer evaluation

	Formula	Computed Values		Target
		14.14 h^{-1} WHSV	0.71 h^{-1} WHSV	
Interphase heat	$\frac{\lvert\Delta H\rvert r''' r_p}{hT_b} < 0.15\,\frac{RT_b}{E}$	7.8×10^{-3}	1.0×10^{-4}	$<1.1\times10^{-2}$
Interparticle heat	$\frac{\lvert\Delta H\rvert r''' r_p^2}{k_e T_w} < 0.4\,\frac{RT_w/E}{\left[1+8\left(\frac{r_p}{R_0}\right)Bi_w\right]}$	1.4×10^{-2}	1.8×10^{-4}	$<1.6\times10^{-2}$
Intraparticle heat	$\frac{\lvert\Delta H\rvert r''' r_p^2}{\lambda T_s} < 0.75\,\frac{RT_s}{E}$	1.4×10^{-2}	1.8×10^{-4}	$<3.1\times10^{-2}$
Interphase mass	$\frac{r_{obs}R_p}{C_B k_D}$	1.1×10^{-5}	1.4×10^{-7}	<0.15
Intraparticle mass	$\frac{r_{obs}R_p^2}{C_s D_{eff}}$	0.4	5.3×10^{-3}	<0.6

2.3.3 Catalyst characterization

Table 5 shows the elemental analysis and Co_3O_4 crystallite size for the fresh and spent catalysts. The amount of cobalt was consistant with the theoretically added amount. All catalysts and the activated carbon contained nitrogen. The nitrogen comes from three potential sources: undecomposed cobalt nitrate, activated carbon support, and NH_4OH. Similar amounts of nitrogen are observed on the spent catalyst (2A-CoOx/N-C-270) demonstrating that nitrogen is not lost from the catalyst during reaction.

Table 5. Elemental analysis and crystallite size estimation of fresh and spent catalysts. (Spent catalyst values are put in parenthesis if available)

Catalyst	Elemental Analysis wt%			Co_3O_4 Crystallite size (nm) by XRD [a]
	Co	C	N	
2A-CoOx/N-C-230	13.20	51.83	1.24	7.2 ± 0.2 (6.2 ± 0.2)
2A-CoOx/N-C-270	12.30 (13.20)	63.41 (56.90)	1.64 (1.76)	6.4 ± 1.6 (5.4 ± 0.2)
2A-CoOx/N-C-350	12.3	54.61	1.37	5.7 ± 0.2 (5.8 ± 0.2)
2A-CoOx/N-C-550	15.4	58.31	1.41	N.A.
A-C-270	-	71.22	0.96	-
Activated carbon	-	65.59	0.60	-

a. The number in the bracket specifies the particle size for the corresponding spent catalyst. The errors were estimated by JADE software.

X-ray diffraction identified three phases on all catalysts (except for 2A-CoOx/N-C-550) as shown in Figure 4: graphite (largest 2θ peak at 12.15°), Co_3O_4 (largest 2θ peak at 16.79°) and CoO (largest 2θ peak at 19.26°). An extra high intensity peak was observed over 2A-CoOx/N-C-550 at 2θ=19.90°, which is for metallic cobalt. The Co_3O_4 crystallite size calculated by Scherrer equation with the peak at 16.79° was shown to be between 5-8 nm (Table 5). The Co_3O_4 crystallite size for 2A-CoOx/N-C-550 could not be obtained from this data. HRTEM images of 2A-CoOx/N-C-270 (Figure 5) exhibit overlapping cobalt oxide particles supported on carbon, with a particle size ranging from 5 and 10 nm. The Co_3O_4 crystallite size was not measured using HRTEM due to the overlapping cobalt oxide particles. The Co_3O_4 crystallite size calculated by XRD showed a slight decrease with increasing pretreatment temperature. The XRD results of the spent catalysts showed similar cobalt phase composition, with no distinguishable change in Co_3O_4 crystallite size compared to the fresh catalysts (Figure A4). Some changes of the crystallite size may not be observable with XRD because small (< 4nm) Co_3O_4 crystallite sizes are not detected with this method. [29]

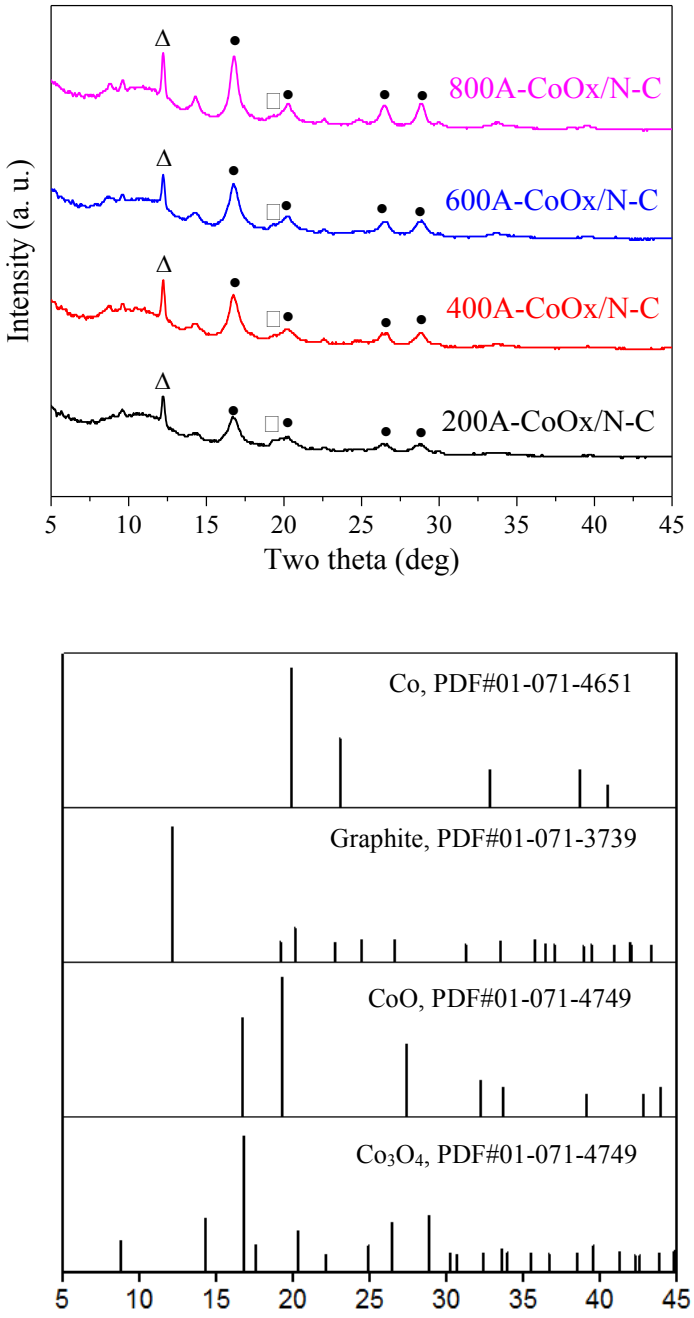

Figure 4. Mo-XRD of 2A-CoOx/N-C catalyst pretreated at different temperatures, with characteristic peaks of ▵graphite, ●Co_3O_4, □CoO, ◆Co.

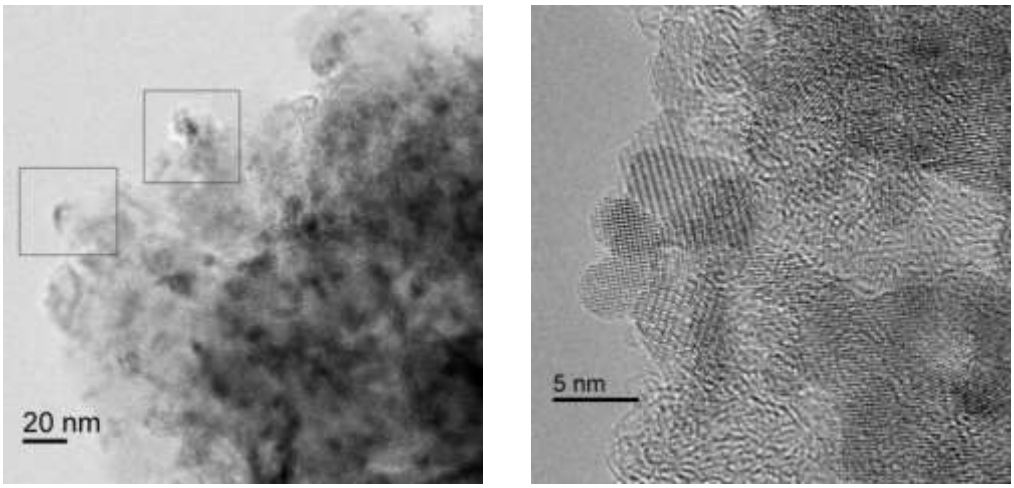

Figure 5. HRTEM image for 2A-CoOx/N-C-270. Left: overlapping cobalt oxide particles. Right: Zoomed-in image showing the lattice fringes of the cobalt particles.

The *in situ* Raman spectra of the 2A-CoOx/N-C catalyst during pretreatment are shown in Figure 6. Spectrum (a) shows characteristic peaks of Co_3O_4 bulk material at 481, 519, 621 and 690 cm^{-1}, whereas spectrum (b) shows CoO bulk material characteristic peaks at 517 and 684 cm^{-1}. Characteristic peaks of bulk $Co(NO_3)_2$ at 740, 1034, 1321 and 1442 cm^{-1} are present in the spectrum (c). Due to the highly intense Raman spectra for the bulk materials, spectra (a) and (c) are divided to 1/2 intensity. Spectrum (d) shows that at room temperature, before pretreatment, a mixture of $Co(NO_3)_2$ and cobalt oxides coexist on the catalyst surface. Raising the temperature from 25 to 150 °C leads to a decrease in the intensity of the $Co(NO_3)_2$ peaks at 740 and 1034 nm^{-1} (d-f), and to the emergence of new Raman signals at 481 and 690 cm^{-1} (g), indicating the decomposition of the $Co(NO_3)_2$ precursor and the formation of Co_3O_4 and CoO. The decomposition temperature of the precursor observed by spectrum (f) is about 50 ^oC lower than that obtained by TGA

(Figure 8). This indicates that cobalt oxides on the catalyst surface reduce at a lower temperature than in the bulk.[30] Since the characteristic peaks of CoO (broad signal at 517 and 684 cm $^{-1}$) and Co_3O_4 (481, 519 and 690 cm^{-1}) overlap, the precise composition of cobalt oxide on the catalyst surface cannot be determined. The signal intensity of CoO at 684 cm^{-1} is much lower and broader than Co_3O_4.[31] Hence by monitoring the decrease and, more importantly, the broadening of the peak (Figure A5), the change of the CoO content can be qualitatively observed. As temperature increases from 150 to 550 ºC ((f)-(n)), the peak at 690 cm^{-1} decreases and broadens, suggesting less Co_3O_4 and an increased CoO content.

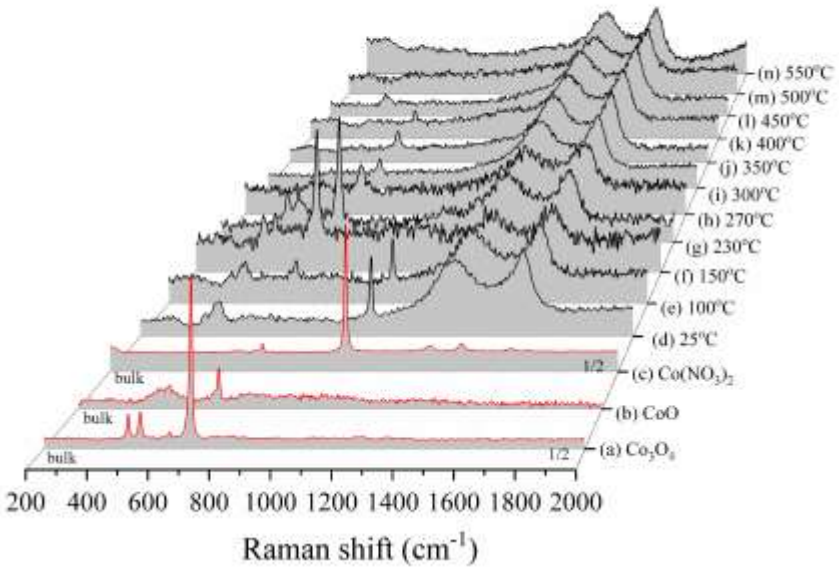

Figure 6. *In situ* Raman spectra of cobalt nitrate, Co_3O_4, CoO, and 2A-CoOx/N-C pretreated at different temperatures. Helium flow = 20 mL/min.

The composition of the cobalt phases was further investigated with XANES. Figure 7 shows the XANES spectra of 2A-CoOx/N-C pretreated in helium at different temperatures. The catalysts pretreated at 230 and 270 ºC were analyzed immediately after helium pretreatment without being exposed to the air. The cobalt standards and the catalysts pretreated at 350 and 550 ºC were exposed to air at room temperature before analysis. The phase compositions of these different catalysts after linear combination fitting are summarized in Table 6. 2A-CoOx/N-C-230 and 2A-CoOx/N-C-270 showed similar XANES to a Co_3O_4 standard, while 2A-CoOx/N-C-350 and 2A-CoOx/N-C-550 curves clearly shifted to a lower edge energy, as shown in Figure 7. The gradual reduction to metallic cobalt is apparent with samples pretreated at higher temperatures and observable as a large pre-edge feature and decreasing edge peak or "white line". There is a clear trend of decreasing oxidation with increasing pretreatment temperature.

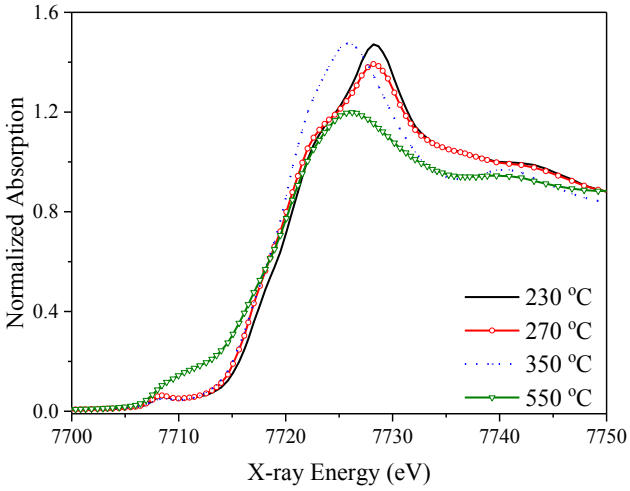

Figure 7. XANES spectra of 2A-CoOx/N-C catalysts pretreated at different temperatures

The ratio of Co(III)/Co(II) for each sample was calculated based on XANES fitting results and summarized in Table 6. Co_3O_4 contains both Co(II) and Co(III) in the molecular formula of $Co_2O_3 \cdot CoO$. The Co_3O_4 content decreases with an increasing pretreatment temperature. Metallic cobalt starts to form when the pretreatment temperature is 550 ^oC. As shown in Table 3, the catalyst activity decreases with increasing pretreatment temperature, suggesting the Co_3O_4 phase is the more active site.

Table 6. XANES fitting results.

Sample	Edge Energy (eV)	XANES fit wt.%			Co(III)/Co(II)
		CoO	Co	Co_3O_4	
2A-CoOx/N-C-230	7720.7	27.5	-	72.5	1.64
2A-CoOx/N-C-270	7720.1	32.0	-	68.0	1.32
2A-CoOx/N-C-350	7720.5	61.7	-	38.3	0.39
2A-CoOx/N-C-550	7720.5	40.1	36.2	23.7	0.37
CoO	7720.1	-	-	-	
Co_3O_4	7724.2	-	-	-	
Co	7708.2	-	-	-	

Figure 8 shows the TGA analysis of the non-pretreated catalysts in flowing nitrogen. The 2A-CoOx/N-C catalyst showed two weight loss peaks at 208 °C and 621 °C. The peak at 208 °C can be assigned to the complete decomposition of cobalt nitrate.[32,33] The weight loss at 621 °C is caused by the reduction of Co_3O_4 to a lower oxidation state (metallic cobalt or CoO), as indicated by XRD and XAS.

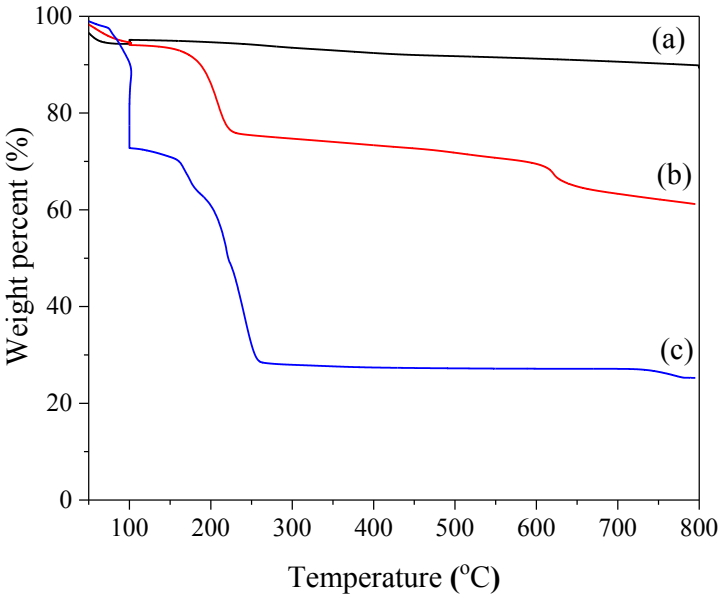

Figure 8. TGA analysis of (a) ammoniated carbon (no weight loss); (b) 2A-CoOx/N-C (18.61 wt.% loss at 208 °C, 6.11 wt.% loss at 621 °C); (c) cobalt precursor: $Co(NO_3)_2 \cdot 6H_2O$ (total 73.76 wt.% loss between 100 and 254 °C) in nitrogen with 10 °C/min ramp rate.

2.3.4 Discussion of reaction mechanism

Schultz *et al*. proposed that a cobalt hydride species is the active catalytic site and mediates the olefin oligomerization.[24,25] Our results indicate that the active site is probably a particular crystallographic plane of Co_3O_4. The Co_3O_4 structure is a normal spinel structure of Co(II) in tetrahedral interstices and Co(III) in octahedral interstices of cubic close packed lattices of oxide anions.[34] Different crystallographic planes will have different distributions of Co(II) and Co(III). A proposed reaction mechanism for butene oligomerization over cobalt oxide on carbon catalyst is shown in Figure 9. Our results suggest that the Co(II) or Co(III) is the most active phase of the cobalt and we will represent the active site in Figure 9 as [Co].

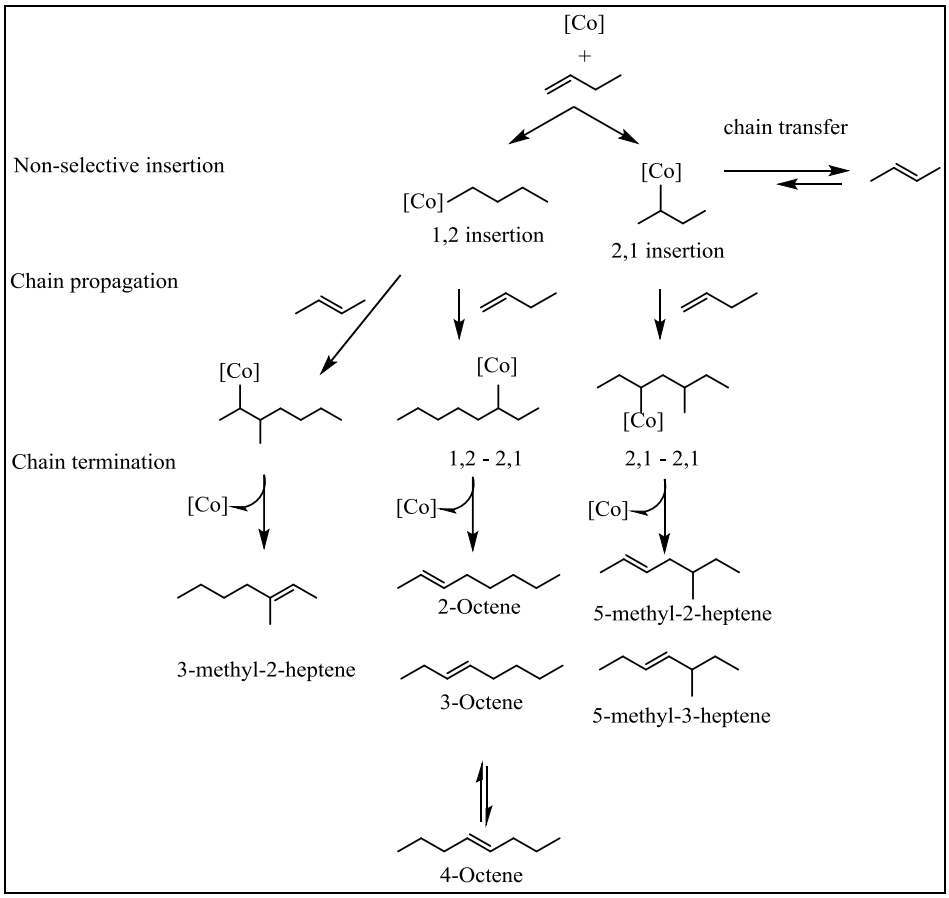

Figure 9. Proposed mechanism for 1-butene oligomerization over cobalt oxide on N-doped carbon catalysts.

The first step in this mechanism is initial non-selective insertion of 1-butene into the cobalt active site. The species formed after 2,1 insertion can either undergo β-hydrogen elimination giving 2-butene, or have another 1-butene inserted between the cobalt-alkyl species followed by a non-selective β-hydrogen elimination giving 5-methyl-2- and 5-methyl-3-heptene. The species formed after 1,2 insertion can react with both 1-butene or 2-butene molecule, forming linear internal octene and 3-methyl-2-heptene, respectively.

Table 7 shows the product distribution from 14.14 h^{-1} WHSV, 1.92 h time on stream. 1-butene was isomerized into linear internal isomers with above 80% selectivity at the reaction conditions. The mechanism is able to account for the formation of all the species detected in the reaction.

Table 7. Experimental and equilibrium methyl-heptene distribution (%) (Reaction conditions: 80 ºC, 450 psig, 14.14 h^{-1} WHSV, 1.92 h time on stream).

Butene isomer distribution (89.2%)		Dimer products selectivity (10.6%)	
1-butene	25.0	*cis*-5-methyl-3-heptene	0.2
trans-2-butene	34.3	*trans*-5-methyl-3-heptene	0.2
cis-2-butene	29.9	*trans*-5-methyl-2-heptene	0.3
		cis-5-methyl-2-heptene	0.6
		4-octene	0.3
		3-octene	5.4
		trans-2-octene	2.0
		trans-3-methyl-2-heptene	0.5
		cis-2-octene	1.1

2.4 Conclusions

Cobalt oxide on carbon catalysts have greater than 80% selectivity towards linear octenes for 1-butene oligomerization. The 1-butene undergoes double bond isomerization to form an equilibrium mixture with *trans*- and *cis*-2-butene. The main linear oligomers from butene oligomerization with a decreasing order of distribution are 3-octene > 2-octene > 4-octene. These internal linear octenes are formed by two steps of 1,2 insertion of 1-butene molecules. The 5-methyl-heptene products can be formed through 2,1 insertion of a 1-butene molecule followed by 1,2 insertion of another 1-butene molecule. 3-methyl-2-heptene was formed through 1,2 insertion of an 1-btuene molecule followed by 1,2 insertion of a 2-butene molecule. The activity of the catalyst increases with increasing Co_3O_4 content. The cobalt composition change was monitored with *in situ* Raman and TGA, which show that cobalt nitrate fully decomposes at about 200 ^oC, and forms overlapping Co_3O_4 and CoO particles, as shown in the XANES, XRD and HRTEM results. XANES result confirms that high pretreatment temperature (550 ^oC) in helium partially reduced the cobalt oxide to metallic cobalt, with a decreasing Co_3O_4 content. The cobalt oxide on carbon catalysts reported in this paper are highly selective for linear octenes and can be used to make internal linear oligomers with a targeted carbon chain length.

Chapter 3. 1-Butene Oligomerization over Cobalt Oxide on N-doped Carbon Catalysts – Effect of Nitrogen Functionalities

D. Zhao, Z. Xu, J. P. Chada, C. A. Carrero, D. C. Rosenfeld, J. L. Rogers, I. Hermans, and G. W. Huber, 'Cobalt Oxide on N-Doped Carbon for 1-Butene Oligomerization to Produce Linear Octenes', ACS Catalysis, 7 (2017), 7479-89.

3.1 Introduction

It was demonstrated in Chapter 2 that cobalt oxide on N-doped carbon catalysts are active for 1-butene oligomerization.[35] The catalysts were prepared by impregnating activated carbon with cobalt nitrate solution, where the activated carbon was treated with concentrated ammonium hydroxide solution both before and after cobalt impregnation. The doubly ammoniated cobalt oxide on carbon catalyst (2A-CoOx/N-C) was reported to exhibit high linear C8 olefin selectivity (70 – 85%). This linear oligomer selectivity is almost two times as high as that of other heterogeneous catalysts including solid acid catalysts,[5,21] supported nickel oxide and cobalt oxide on other supports.[24,36] The low linear selectivity (less than 30%) of solid acid catalysts is due to the existence of Brønsted acid sites that create tertiary and secondary carbocations. Our postulated mechanism for 1-butene oligomerization by our cobalt oxide on N-doped carbon catalyst is a Cossee-Arlman insertion mechanism (Figure 9). This mechanism is principally supported by the product distribution resulting from ethylene, propylene, 1-butene and 1-hexene oligomerization.[37] After adsorption of 1-butene to the cobalt surface, possibly through binding of the olefin's π system to cobalt, it undergoes 1,2 insertion or 2,1 insertion into a cobalt-hydride generating n-butyl- and sec-butyl-cobalt alkyl species, respectively. The sec-butyl-cobalt species can undergo chain transfer to form 2-butene. Linear dimer species are formed via 2,1 insertion of 1-butene into the n-butyl-cobalt species followed by β-H elimination regenerating Co-H. The branched dimer species we observed are formed via 1) insertion of 2-butene into n-butyl-cobalt species or 2) 2,1 insertion of 1-

butene into sec-butyl-cobalt species. Branched dimers containing ethyl groups would form via consecutive 1,2 insertions however we only observed methyl branched C8 species.

2A-CoOx/N-C catalysts were first synthesized by Schultz *et al*. and tested for dimerization of propylene, 1-butene and 1-hexene with linear selectivities of 52, 65 and 83%, respectively.[24,25] The ammoniated catalysts exhibited more than a fourfold increase in activity for propylene dimerization compared to catalysts synthesized without an ammonium hydroxide treatment. Elemental analyses showed that impregnation of the carbon with ammonium hydroxide caused an increase in nitrogen content (from 0.55 to 1.12 wt.%).[24] The authors hypothesized that a cobalt (II) hydride species was the active site and the ammonium hydroxide treatment stabilized the cobalt (II) valence state. However, neither detailed characterization of the nitrogen species, nor an elucidation of the interaction between the nitrogen containing carbon support and cobalt oxide were included in the study.

The ammonium hydroxide treatment of the carbon produces a wide range of carbon-nitrogen structures. Since Schultz's reports, methods for controlled introduction of nitrogen into carbon frameworks have been reported. These methods include synthesis of N-doped mildly reduced graphene oxide;[38-40] soft templating method with nitrogen and carbon source to synthesize N-doped mesoporous carbon;[41] catalytic chemical vapor deposition (CCVD) of nitrogen-containing hydrocarbons over supported transition metal catalysts to synthesize N-doped nanocarbon [42,43] and amination of carbon with long chain

organic amines, NH_3 or HCN. [44-47] These synthesis methods have been proposed to create materials that have tailored chemical properties[48,49] and electronic properties.[40,50] Improved activity, selectivity and stability of cobalt, cobalt oxide and palladium supported on N-doped carbon materials have been observed for oxygen reduction reaction (ORR) and oxygen evolution reaction (OER) for fuel cells,[39,51-53] CO_2 reduction [46] and liquid phase selective oxidation catalysis.[47,54] Various N chemical configurations with substantially different chemical properties such as pyridinic N, pyrrolic N and quaternary N can be effectively introduced by treating activated carbon with long chain organic amines, NH_3 or HCN.[44,45] These N sites are able to alter the local electronic properties of the carbon material and interact with supported nanoparticles.[55]

3.2 Experimental

3.2.1 Sample synthesis

Synthesis of N-doped carbon. Acid washed carbon (AWC) was prepared by treating activated carbon (Norit, Darco MRXm-1721, BET surface area: 600-800 m^2/g) with 10% HNO_3 to generate oxygenated functional groups as reactive sites for nitrogen. Five grams of sieved activated carbon (250-600 μm particle size) was submerged in 140 mL 10% HNO_3 at 150 ^oC for 2 h under continuous stirring. Afterwards the carbon was rinsed several times with DI water and dried at 130 ^oC overnight. N-doped carbon (XXX-N-C) was obtained by treating 2 g of the pre-oxidized activated carbon with flowing ammonia gas at 200, 400, 600, 800 ^oC for 4 h, where XXX represents the ammoniation temperature.

Synthesis of Cobalt on N-doped carbon catalysts. Cobalt on N-doped carbon catalysts (XXXA-CoO_x/N-C) were prepared by impregnating 5g of N-doped carbon with cobalt nitrate solution composed of 4.7 g $Co(NO_3)_2 \cdot 6H_2O$ (Sigma Aldrich) and 3 mL DI water. The impregnated samples were dried at 130 ^oC overnight. A doubly-ammoniated cobalt on carbon catalyst (2A-CoOx/N-C) was synthesized according to Chapter 2. [35] Five grams of sieved activated carbon was treated with 4.6 mL of 30% NH_4OH solution at room temperature for 0.5 h and dried at 130 ^oC for 2 h prior to cobalt impregnation. The NH_4OH-treated carbon was impregnated with cobalt nitrate solution and dried 130 ^oC overnight. After the impregnation, another 12.5 mL of 30% NH_4OH solution was added drop wise onto the sample and the sample was dried overnight on a hot plate at 130 ^oC.

3.2.2 Catalytic measurement

1-butene oligomerization reactions were carried out in an up-flow fixed-bed reactor. Typically 0.5 – 1 g catalyst without diluents was packed into stainless steel tubular reactor (3/8 in. O.D., 0.049 in. wall). The catalyst was pretreated in flowing helium (150 mL/min) with 5.5 ºC/min ramp rate and held at 230 ºC for 2 h. After the pretreatment, the reactor system was cooled to 80 ºC and pressurized to 450 psig with helium using a backpressure regulator. 1-butene (99.9%, Matheson) was fed into the reactor through a high pressure syringe pump (500D, Teledyne Isco). Flow rates were varied from 0.01 to 0.2 mL/min to achieve different weight hourly space velocity (WHSV = hourly 1-butene feed flow rate (g/h)/catalyst mass (g)). Liquid samples were collected with a chilled 50-mL stainless-steel gas–liquid separator and sampled with chilled 50 mL glass vials filled with approximately 10 g of 0.5 wt.% heptane in hexane solvent.

The liquid reaction product was analyzed by a comprehensive two-dimensional gas chromatograph – mass spectrometer (2D GC – MS) as described in our previous work. [18] The gas product was analyzed by online gas chromatograph (GC – FID, Shimadzu). The liquid products were hydrogenated by Pd/C catalyst to determine the skeletal composition.[35] The following standards were tested for product identification: 1-octene, trans-2-octene, cis-2-octene, 2-methyl-1-heptene, 2-methyl-2-heptene, trans-2-methyl-3-heptene, trans-6-methyl-3-heptene, 2,3-dimethyl-2-hexene, 2,3-dimethyl-3-hexene, 2,3,4-trimethyl-2-pentene, 2,4,4-trimethyl-2-pentene (Sigma-Aldrich), cis-2,5-dimethyl-

3-hexene (Pfaltz & Bauer), cis-3-octene, trans-3-octene, cis-4-octene, trans-4-octene, 3-methyl-2-heptene, 3-methyl-3-heptene, 5-methyl-2-heptene, 5-methyl-3-heptene, 3,4-dimethyl-2-hexene (ChemSampCo). The carbon balance for all the reactions were 95% - 105%.

Total 1-butene conversion, isomerization and oligomerization selectivity, oligomerization product distribution, specific and linear octene distribution as well as number of chain branches (NCB) were calculated from Eq. 6-12.

$$\textit{Total 1-butene conversion (\%)} = \frac{moles\ of\ carbon\ in\ detected\ products}{moles\ of\ carbon\ in\ 1-butene\ feed} \times 100\% \quad \text{(Eq. 6)}$$

$$\textit{Isomerization selectivity (\%)} = \frac{moles\ of\ carbon\ in\ 2-butene}{moles\ of\ carbon\ in\ detected\ products} \times 100\% \quad \text{(Eq. 7)}$$

Oligomerization selectivity (%) =

$$\frac{moles\ of\ carbon\ in\ oligomerization\ products}{moles\ of\ carbon\ in\ detected\ products} \times 100\% \quad \text{(Eq. 8)}$$

Oligomerization product distribution (%) =

$$\frac{moles\ of\ carbon\ in\ specific\ oligomerization\ products}{moles\ of\ carbon\ in\ oligomerization\ products} \times 100\% \quad \text{(Eq. 9)}$$

$$\textit{Specific octene distribution (\%)} = \frac{moles\ of\ carbon\ in\ specific\ octene\ product}{moles\ of\ carbon\ in\ all\ octene\ product} \quad \text{(Eq. 10)}$$

$$\textit{Linear octene distribution (\%)} = \frac{moles\ of\ carbon\ in\ linear\ octene\ product}{moles\ of\ carbon\ in\ all\ octene\ product} \quad \text{(Eq. 11)}$$

NCB = 0×linear octene distribution (%) +1×methyl-heptene distribution (%)

+ 2×dimethyl-hexene distribution (%) (Eq. 12)

3.2.3 Catalyst characterization

All catalyst characterization was done on samples pretreated in flowing helium with 5.5 ^{o}C/min ramp rate and held at 230 ^{o}C for 2 h. Elemental analysis of the pretreated catalysts were performed by Galbraith Laboratories, Inc. Inductively Coupled Plasma Atomic Emission Spectrometry (ICP-AES) and Suppressed Ion Chromatography methods were used for the analysis.

Nitrogen adsorption analysis was performed on Gemini VII (Micromeritics) at -196^{o}C. The samples were degassed under vacuum at 120 ^{o}C for 12 h prior to the measurements. Brunauer-Emmett-Teller (BET) surface areas were obtained from nitrogen adsorption data in the relative range (P/P_o) of 0.05 to 0.41. Total pore volume was based on single point adsorption at P/P_o of 0.98.

Powder X-ray diffraction (XRD) patterns were collected in a Rigaku Rapid II diffractometer with Mo Kα source operating at 50 kV and 50 mA. The diffraction angle was varied from 2^{o} to 45^{o} during a total exposure time of 30 min. Crystallite phase identification was carried out using JADE 9 software. The Scherrer equation was used to calculate the crystallite size based on line broadening of the peak at $2\theta=16.79^{o}$ corresponding to (311) plane in spinel Co_3O_4.

X-ray photoelectron spectroscopy (XPS) was performed on K-alpha XPS spectrometer (Thermo Scientific) with monochromated Al Kα X-ray source. The N1s envelopes were fitted using mixed Gaussian-Lorenzian profiles after subtraction of Shirley background

using Avantage (Thermo Scientific) software. The binding energies were calibrated based on the graphite C1s peak at 284.8 eV. The fitting was performed by fixing the peak maximum within ± 0.2 eV and applying a full width half-maximum (FWHM) of 1.4-1.6 eV.[48] For each sample, XPS spectra were measured and analyzed for three different spots. Standard deviations were calculated based on the three analyses.

X-ray absorption spectroscopy (XAS) measurements of the cobalt K-edge (7709 eV) were collected at beamline 12-BM of the Advanced Photon Source at Argonne National Laboratory (Lemont, Il). Catalyst samples were crushed, diluted with boron nitride (Sigma Aldrich), and pelletized in a stainless-steel sample cylinder. The cylinder was then sealed in a kapton-windowed quartz tube under the flow of helium. The pelletized sample was pretreated in a tube furnace at 230 ^{o}C, sealed, and transferred to the beamline hutch without exposure to air. All spectra were collected at room temperature in the transmission geometry utilizing three ion chamber detectors. A cobalt foil placed between the last two ion chambers was used for energy calibration. Spectra of CoO and Co_3O_4 were collected and used as experimental standards. All spectra were processed and analyzed with the Athena and Artemis software packages using IFEFFIT.[56] An average oxidation state was calculated by a linear combination fitting of experimental cobalt standards in the range of -20 to 30 eV above the edge energy. The first two coordination shells within the EXAFS region were fit with Fourier transforms of the theoretical scattering paths generated for a model Co_3O_4 spinel structure in R space. The amplitude

reduction factor (S_0^2) of 0.829 was determined from fitting a cobalt foil and fixed for all cobalt catalyst samples.

3.3 Results and discussion

3.3.1 Catalyst activity and selectivity

Table 7 shows the inlet and outlet concentrations, conversion and selectivity of the different catalysts at 64.0 to 68.6 hours time on stream. All catalysts were able to catalyze the isomerization and oligomerization of 1-butene. At the WHSV's reported in Table 7, the 1-butene conversion was above 86.2%. 2-butene was the primary product from this reaction with isomerization selectivities ranging from 51.3% to 81.42%. The oligomerization selectivity was 2.6 times higher for the 800A-CoOx/N-C catalyst compared to the 2A-CoOx/N-C catalyst. The oligomerization selectivity increased with increasing NH_3 treatment temperature of the carbon support. The 1-butene to 2-butene ratio for 2A-CoOx/N-C catalyst was near equilibrium while the 1-butene to 2-butene ratio was further from equilibrium for the NH_3 treated carbon catalyst. The oligomer products were composed mostly of C8 olefins (>92%), branched C12 olefins (3-7%) and trace amount of C16 olefins (<1%). The linear C8 olefin distribution ranged from 66.6% to 73.7%. No products were observed for 1-butene conversion over 800A-N-C at the same reaction conditions, demonstrating that the N-C support is inert.

Table 7. 1-butene oligomerization over different CoO_x/N-C catalysts. (Reaction conditions: 1-butene feed, 80 ^oC, 450 psig, 0.71 h^{-1} WHSV)

Catalyst		2A-CoOx /N-C	200A-CoO_x /N-C	400A-CoOx /N-C	600A-CoOx /N-C	800A-CoOx /N-C
Time on stream (h)		66.2	68.6	64.0	67.2	67.6
1-butene feed concentration (mol/L)		10.5	10.5	10.5	10.5	10.5
Outlet concentration (mol/L)	1-butene	1.5	1.0	0.7	0.9	0.9
	2-butene	7.7	7.6	7.5	6.7	5.4
	Linear C8 olefins	0.6	0.9	0.8	1.2	1.8
	Branched C8 olefins	0.2	0.3	0.6	0.5	0.6
	C12 olefins	2.2×10^{-2}	3.1×10^{-2}	0.05	0.1	0.1
	C16 olefins	0	0	9.7×10^{-5}	1.9×10^{-3}	5.5×10^{-3}
$(1\text{-butene}/2\text{-butene})_{reaction}/(1\text{-butene}/2\text{-butene})_{equilibrium}$[a]		2.9	1.9	1.3	2.0	2.5
1-butene conversion (%)		86.2	91.3	94.2	91.8	92.0
Oligomerization Selectivity (%)		18.6	23.8	28.1	34.8	48.8
Isomerization Selectivity (%)		81.42	76.21	71.92	65.17	51.25
Oligomerization product distribution (%)	Linear C8 olefins	73.8	71.7	71.5	66.5	68.2
	C8 olefins	97.3	96.1	95.4	94.0	92.5
	C12 olefins	2.7	3.9	4.6	5.8	7.1
	C16 olefins	0	0	1.3×10^{-2}	0.2	0.4

a. The thermodynamic equilibrium composition was calculated with Aspen using Peng-Robinson method.

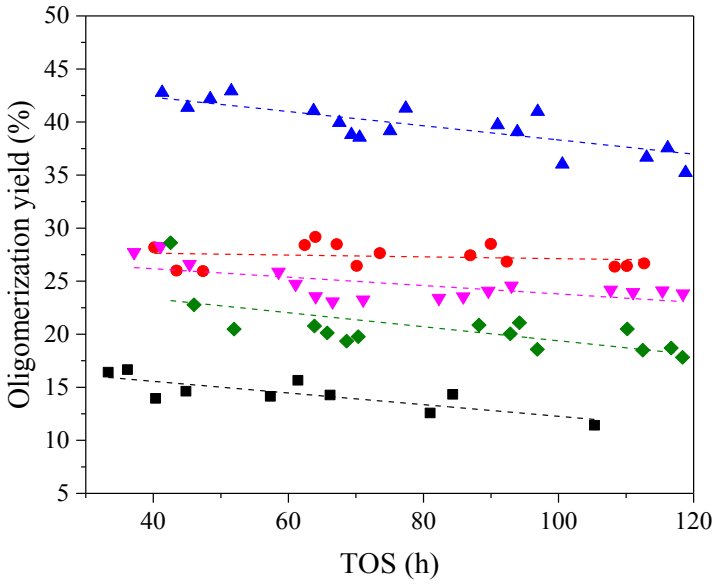

Figure 10. Oligomerization yield as a function of time on stream for (■) 2A-CoOx/N-C, (◆) 200A-CoOx/N-C-X, (▼) 400A-CoOx/N-C-X, (●) 600A-CoOx/N-C-X, (▲) 800A-CoOx/N-C-X. Reaction condition: 1-butene feed, 80 ºC, 450 psig, 0.71 h^{-1} WHSV. Dotted lines: linear fitting of time-on-stream data.

Figure 10 shows the oligomerization yield as a function of time on stream for the different catalysts. The oligomerization yield increases with the ammonia treatment temperature. The distribution of C8 products did not change with time on stream. Xu *et al.*[37] hypothesize that the observed deactivation is due to deposition of heavier oligomer products on the catalyst surface. Deactivation rates are not reported here due to the high overall 1-butene conversions. The oligomerization yield for 2A-CoOx/N-C decreased from 18.4% to 12.8% which is a 5.6% decrease over 34 hours to 105 hours time-on-stream. Under similar conditions, the oligomerization yield for 200A-CoOx/N-C, 400A-CoOx/N-C, 600A-CoOx/N-C and 800A-CoOx/N-C decreased by 5.6%, 4.4%, 0.2% and

5.8% respectively. This demonstrates that 200A-CoOx/N-C, 400A-CoOx/N-C and 800A-CoOx/N-C have similar deactivation trend as catalysts prepared by NH_4OH. 600A-CoOx/N-C had the slowest deactivation of any catalyst tested.

The C8 olefin distributions are shown in Table 8. High linear C8 distributions (70.8 to 75.8%) were observed with the linear C8 olefin concentration decreasing in the order 3-octene > *trans*-2-octene > *cis*-2-octene ~ 4-octene. We were not able to distinguish between *cis* and *trans* isomers for 3- and 4- octene. Branched C8 products included *trans*-3-methyl-2-heptene, *cis*- and *trans*-5-methyl-2-heptene, as well as *cis*- and *trans*-5-methyl-3-heptene. All the catalysts investigated herein exhibited similar C8 olefin distributions, suggesting that the reaction proceeds via the same reaction pathway (Figure 9) for all catalysts studied in this chapter. These catalysts are the most selective heterogeneous catalysts for the production of linear olefins that have been reported in the literature with over 70% of the oligomers being linear. In contrast, the linear oligomer selectivity is less than 30% for other heterogeneous catalysts including solid acid catalysts,[5,21] supported nickel oxide, and supported cobalt oxide.[24,36]

Table 8. C8 olefin distribution for 1-butene oligomerization (reaction conditions: 80 ºC, 450 psig, 0.71 h^{-1} WHSV)

Catalyst		2A-CoOx /N-C	200A-CoOx /N-C	400A-CoOx /N-C	600A-CoOx /N-C	800A-CoOx /N-C
Time on stream (h)		66.2	68.6	64.0	67.2	67.6
C8 olefin Distribution (%)	*cis*-2-octene	6.8	7.1	6.7	6.2	6.5
	trans-2-octene	18.0	16.8	16.6	15.6	15.6
	3-octene	45.8	46.0	45.4	43.8	45.1
	4-octene	5.3	4.8	6.2	5.1	6.6
	cis-5-methyl-3-heptene	2.1	2.4	2.4	2.3	2.2
	trans-5-methyl-3-heptene	2.3	2.5	2.7	2.9	3.0
	trans-3-methyl-2-heptene	11.7	12.2	11.9	15.1	12.8
	trans-5-methyl-2-heptene	4.2	4.3	4.4	4.7	4.6
	cis-5-methyl-2-heptene	4.0	3.9	3.6	4.3	3.7
Linear C8 distribution (%)		75.8	74.7	75.0	70.8	73.8
Number of chain branches		0.3	0.3	0.3	0.3	0.3

The reaction was carried out at different WHSV's over 600A-CoOx/N-C and 2A-CoOx/N-C. Table 9 tabulates the inlet and outlet concentrations, conversion and selectivities at similar number of turnovers. The C4 isomer composition approached thermodynamic equilibrium with increasing 1-butene conversion for both catalysts. The oligomerization selectivity increased with increasing conversion for 600A-CoOx/N-C as shown in Figure 11. The outlet 2-butene concentration increased with increasing 1-butene

conversion for both catalysts at 1-butene conversions less than 90%. At conversions above 90% the 2-butene concentration decreased. This suggests that at longer contact times the 2-butenes are oligomerized. Table 10 lists the specific C8 olefin product concentrations at different WHSV's over 600A-CoOx/N-C and 2A-CoOx/N-C. The increase in the concentration of 3-methyl-2-heptene with 1/WHSV also proves the oligomerization of 2-butene as 3-methyl-2-heptene can only be formed via the oligomerization of 1-btuene and 2-butene. The oligomerization selectivity went through a slight minimum as a function of conversion for the 2A-CoOx/N-C catalyst. As the conversion increases, the linear C8 olefin distribution decreases and the branched C8 olefins increase. As shown in Figure 9, branched C8 olefins can be produced in two ways: 1) 1, 2 insertion of 1-butene forming an n-butyl-cobalt alkyl followed by its reaction with 2-butene to form 3-methyl-2-heptene or 2) re-adsorption and insertion of 2-butene forming sec-butyl-cobalt followed by its reaction with 1-butene to form 5-methyl-2-heptene and 5-methyl-3-heptene. The C12 and C16 distribution increased for both catalysts with increasing conversion. The degree of branching of the C12 and C16 products was not analyzed.

Table 9. Effect of WHSV for 1-butene oligomerization over 600A-CoOx/N-C and 2A-CoOx/N-C catalysts. (Reaction conditions: 1-butene feed, 80 ºC, 450 psig)

Catalyst		600A-CoOx/N-C					2A-CoOx/N-C		
WHSV (h^{-1})		14.1	7.1	3.6	0.7	0.4	14.1	0.7	0.4
Time on stream (h)		5.9	8.2	13.9	92.3	120.5	4.1	66.2	82.8
Number of Turnovers [a] ($mol_{1\text{-butene}}/mol_{Co}$)		402.1	354.8	347.0	324.2	346.3	354.9	349.9	221.3
1-butene Feed concentration (mol/L)		10.5	10.5	10.5	10.5	10.5	10.5	10.5	10.5
Outlet Concentration (mol/L)	1-butene	3.6	3.5	2.4	0.8	0.4	3.1	1.5	0.6
	2-butene	5.6	5.7	6.3	6.9	5.8	6.3	7.7	7.5
	Linear C8 olefins	0.6	0.6	0.8	1.1	1.8	0.6	0.6	1.1
	Branched C8 olefins	0.2	0.2	0.3	0.5	0.7	0.1	0.2	0.3
	C12 olefins	1.4×10^{-2}	2.0×10^{-2}	3.3×10^{-2}	0.1	0.1	0	0	0.1
	C16 olefins	0	0	7.1×10^{-4}	3.0×10^{-3}	6.2×10^{-3}	0	0	0
$(1\text{-butene}/2\text{-butene})_{reaction}$/ $(1\text{-butene}/2\text{-butene})_{equilibrium}$		9.6	9.1	5.6	1.6	1.0	7.4	2.9	1.1
1-butene conversion (%)		66.8	68.1	78.6	93.2	96.5	71.1	90.3	94.9
Oligomerization selectivity (%)		23.1	23.2	26.9	33.5	47.7	17.7	18.6	28.4
Isomerization selectivity (%)		76.9	76.8	73.1	66.5	52.3	82.3	81.4	71.7
Oligomerization product distribution (%)	Linear C8 olefins	76.6	74.1	70.9	65.7	66.9	82.3	73.8	75.2
	C8 olefins	97.4	96.5	95.5	93.7	92.8	98.5	97.3	95.2
	C12 olefins	2.6	3.5	4.5	6.0	6.7	1.5	2.7	4.6
	C16 olefins	0	0	0	0.4	0.5	0	0	0.2

a. Turnover number = (time on stream) × (1-butene feed rate) × (total 1-butene conversion)/(moles of cobalt loading)

Table 10. Concentration of specific C8 olefin products at different WHSV's over 600A-CoOx/N-C and 2A-CoOx/N-C catalysts. (Reaction conditions: 1-butene feed, 80 ºC, 450 psig)

catalysts		600A-CoOx/N-C					2A-CoOx/N-C		
WHSV (h^{-1})		14.1	7.1	3.6	0.7	0.4	14.1	0.7	0.4
1/WHSV (h)		0.1	1.4	0.3	1.39	2.9	0.1	1.4	2.9
Time on stream (h)		5.9	8.2	13.9	92.3	120.5	4.1	66.2	82.8
Number of Turnovers (mol $_{1\text{-butene}}$/mol $_{Co}$)		402.1	354.8	347.0	324.2	346.3	354.9	349.9	221.3
Outlet Concentration (10^{-2} mol/L)	4-octene	2.6	3.0	5.9	7.9	14.5	3.2	4.2	9.4
	3-octene	40.4	38.8	50.9	71.6	109.0	32.0	36.0	62.5
	trans-2-octene	13.9	13.4	17.5	24.8	37.9	12.7	14.1	28.1
	cis-2-octene	7.4	8.3	7.7	10.0	14.7	5.9	5.3	10.0
	cis-5-methyl-3-heptene	1.9	1.7	2.8	3.8	5.4	1.3	1.5	2.7
	trans-5-methyl-3-heptene	2.0	1.9	3.2	4.9	7.5	1.0	1.6	3.7
	trans-5-methyl-2-heptene	3.0	3.0	5.1	8.2	13.0	2.4	3.0	5.9
	cis-5-methyl-2-heptene	4.6	4.1	4.9	7.1	9.1	2.6	2.8	4.8
	trans-3-methyl-2-heptene	6.0	8.5	12.4	24.7	33.1	4.4	8.4	13.2

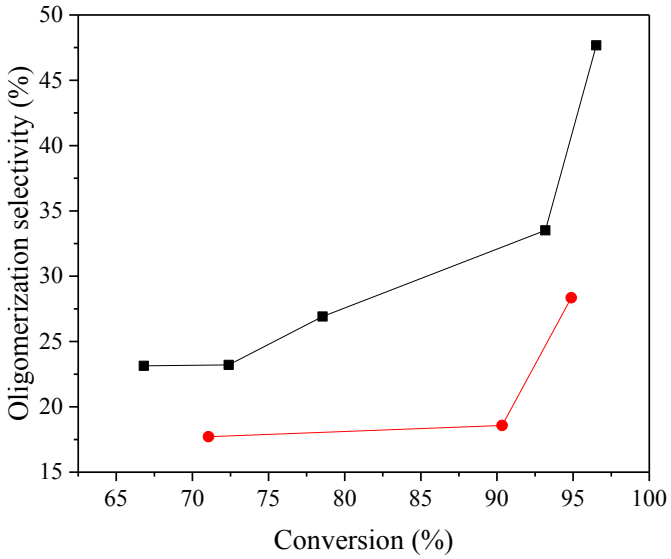

Figure 11. Oligomerization selectivity vs. 1-butene conversion for (●) 2A-CoOx/N-C and (■) 600A-CoOx/N-C.

Figure 12 illustrates the outlet concentration as a function of 1/WHSV. At shorter contact time (i.e., 1/WHSV < 1.4 h), the concentration of 1-butene decreased and the concentration of 2-butene and oligomers increased. As the contact time increased (1/WHSV > 1.4 h), the concentration of 1-butene and 2-butene decreased while the oligomer concentration increased.

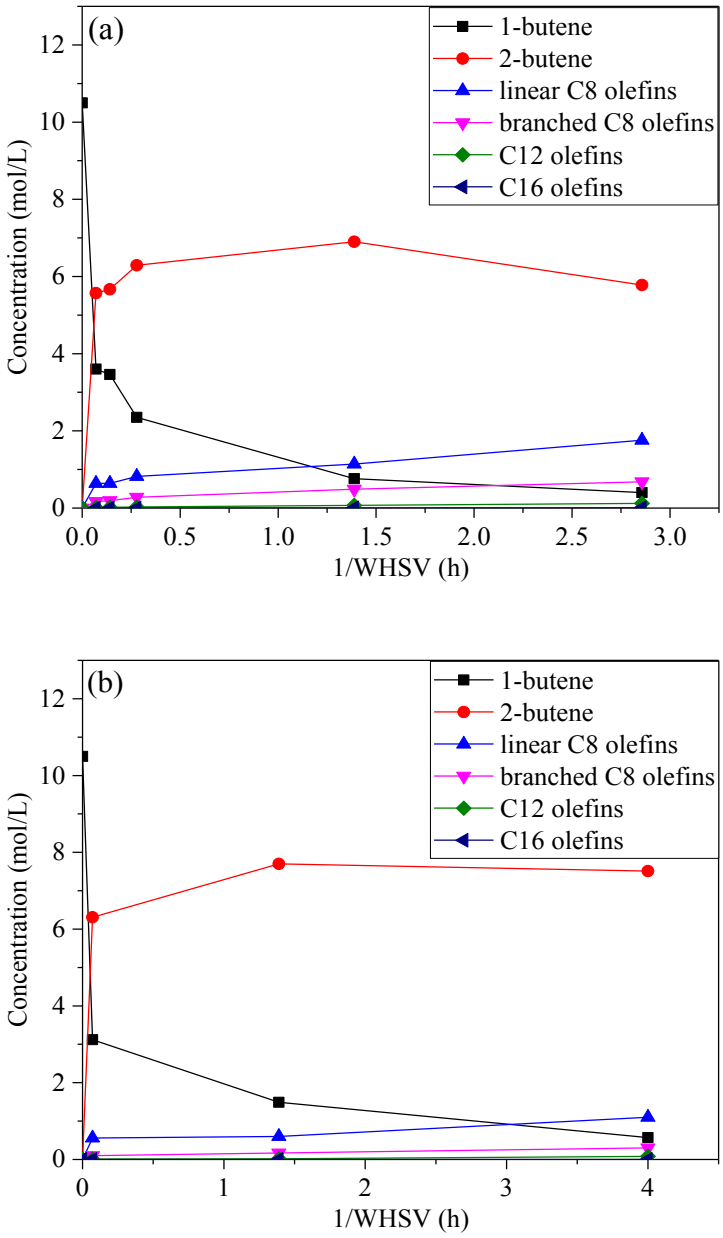

Figure 12. Reaction species concentration change as a function of 1/WHSV for (a) 600A-CoOx/N-C and (b) 2A-CoOx/N-C.

3.3.2 Catalyst characterization

Table 11 compares the elemental composition, BET surface area, total pore volume and Co_3O_4 crystallite size of the different catalysts prior to reaction. Elemental analysis showed similar cobalt loadings (~13 wt.%) for all catalysts. Silicon is an impurity in the activated carbon. Upon treatment of activated carbon with nitric acid, graphitic carbon can be oxidized to form oxygenated surface species such as carboxyl groups.[57-60] Nitrogen insertion occurs via the reaction of NH_3 with oxygenated surface species during the ammonia treatment.[44,48,61] The amount of nitrogen incorporated into the activated carbon increased with the NH_3 treatment temperature as evidenced by the elemental analysis results. The BET surface area and total pore volume also increased with NH_3 treatment temperature, consistent with other studies.[44,62] This increase in BET surface area and pore volume can be attributed to the formation of micropores in the carbon framework. The characteristic peaks of Co_3O_4 crystalline and graphite were present in the XRD patterns (Figure 4). An average crystallite size of 5-7 nm was observed for the different catalysts indicating that for these catalysts there is no correlation between crystallite size observed from XRD and oligomerization activity. However, XRD only measures crystallite size larger than 4nm.[35] Moreover, the Scherrer equation estimates the crystallite size instead of particle size as demonstrated by Munnik *et al.*[63] and Borg *et al.*.[64] In their work, aggregates (or particles) of cobalt oxide crystallites were observed for cobalt oxide on silica from TEM. The aggregate size is different from crystallite size measured by XRD. Attempts to investigate the morphology of these catalysts with TEM were unsuccessful

due to overlapping of cobalt oxide particles at high cobalt loading and the poor contrast between the cobalt oxide and the carbon support. [35]

Table 11. Elemental analysis, BET surface area, total pore volume and crystallite size of pretreated catalysts

Catalyst		2A-CoOx/N-C	200A-CoOx/N-C	400A-CoOx/N-C	600A-CoOx/N-C	800A-CoOx/N-C
Elemental Analysis (wt.%) [a]	C	51.83	55.88	53.7	56.67	54.88
	Co	13.20	12.40	13.00	12.40	12.90
	N	1.24	1.13	1.77	1.57	2.21
	H	1.43	1.33	1.45	1.46	1.42
	Si	NA	3.16	4.57	2.76	4.03
BET surface area (m^2/g) [b]		341.7 ± 16.0	349.9 ± 17.8	375.2 ± 17.8	373.6 ± 18.3	409.0 ± 20.2
Total pore volume (cm^3/g)		0.44	0.41	0.43	0.46	0.47
Co_3O_4 Crystallite size by XRD (nm)[b]		7.2 ± 0.2	4.7 ± 0.2	4.9 ± 0.2	4.9 ± 0.2	7.0 ± 0.2

a. The remainder of the reported elemental composition is assumed to be oxygen.
b. The mean square errors were calculated from the data fitting.

The bulk cobalt oxidation state and local structure of the most active catalyst (800A-CoOx/N-C) were probed by XAS without exposure to air after catalyst pretreatment. Both the X-ray absorption near-edge structure (XANES) and the extended x-ray absorption fine structure were analyzed. CoO and Co_3O_4 were used as experimental standards to determine an average cobalt oxidation state. The linear combination fit (LCF), shown in Figure 13a, resulted in an average composition of 21.7% Co(II) and 78.3% Co(II,III). The

LCF suggests a partially reduced sample compared to the most thermodynamically stable oxide, Co_3O_4. This was consistent with a recent analysis of Co_3O_4 nanocrystals grown on N-doped graphene sheets.[65] Wang *et al.* suggested that there was likely a strong covalent interaction between the N-doped graphene support and the small crystallites. Even with the partial reduction suggested by the LCF, the EXAFS structure was most appropriately fitted by a model based on Co_3O_4 scattering paths as can be seen in Figure 13b-c. The corresponding fitting parameters are given in Table 12. The two inequivalent scattering lengths for the second coordination shell was apparent as would be expected in a spinel structure. The fit suggests that the bulk structure is most similar to Co_3O_4, in agreement with XRD, while some fraction of the cobalt is partially reduced. Any Co-N coordination was not able to be determined by analysis of the Co K-edge as the path length for Co-N and Co-O are nearly identical. Future analysis of the bonding orbitals (N K-edge and Co L-edge) would likely provide more conclusive evidence of this proposed Co-N interaction. 800A-CoOx/N-C did not show measurable differences in cobalt bulk oxidation state or coordination compared to 2A-CoOx/N-C.[35]

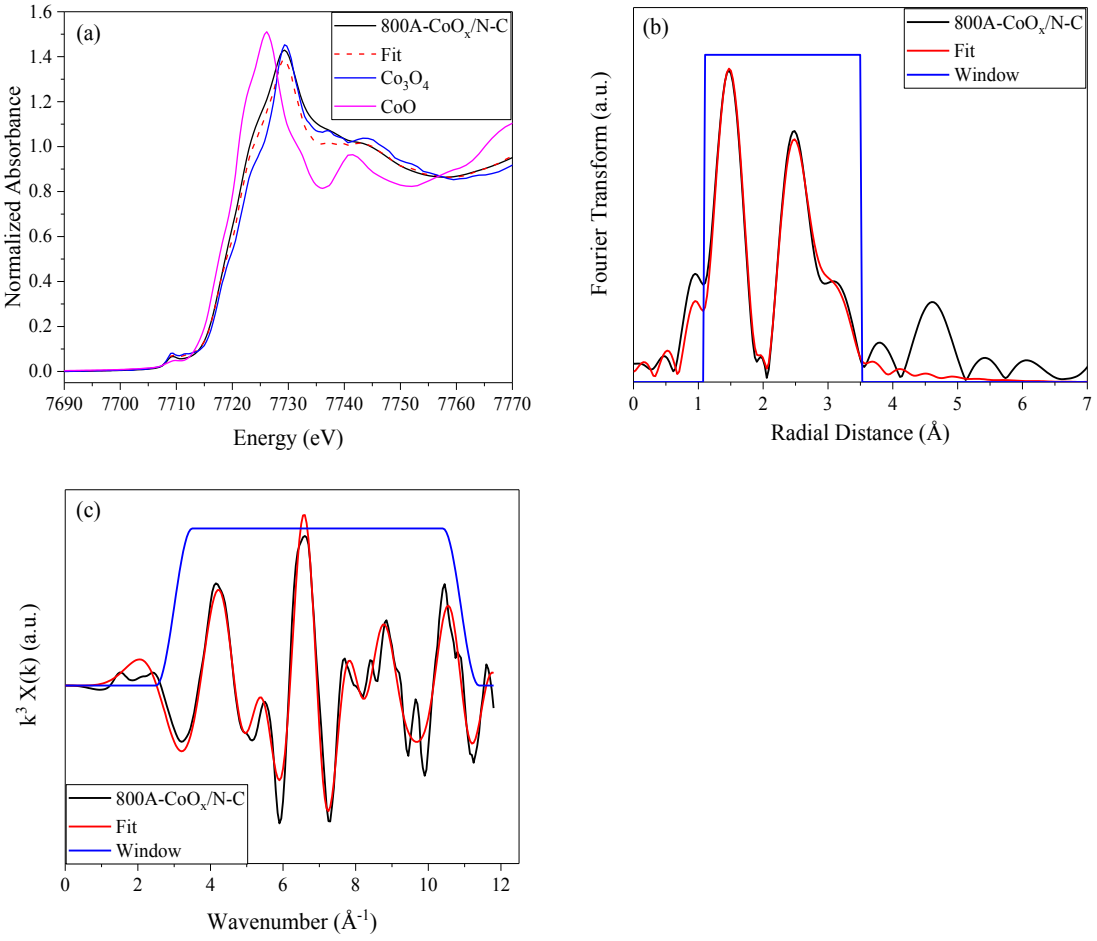

Figure 13. Processed XAFS fits of 800A-CoOx/N-C (a) Linear combination XANES along with the two cobalt oxide experimental standards (b) k^3-weighted Fourier transform of the EXAFS in R space without phase correction (c) Extracted EXAFS of data and fit in k space

Table 12. EXAFS fitting parameters for first two shells of 800A-CoOx/N-C

	Shell	CN[a]	R,[b] Å	σ^2,[c] Å^2	ΔE,[d] eV
1st Shell	Co-O(O)	2.6 ± 0.4	1.91 ± 0.01	0.003 ± 0.001	-1.3 ± 1.0
	Co-O(T)	1.3 ± 0.5	1.96 ± 0.01	0.003 ± 0.001	-1.3 ± 1.0
2nd Shell	Co-Co(O)	3.4 ± 0.8	2.86 ± 0.01	0.007 ± 0.002	-1.3 ± 1.0
	Co-Co(T)	3.6 ± 0.8	3.34 ± 0.01	0.007 ± 0.002	-1.3 ± 1.0

a. CN: Average coordination number
b. R: Interatomic distance
c. σ2: Debye-Waller factor
d. ΔE: Energy shift

The surface chemistry of the catalysts was investigated by XPS and the bulk compositions are shown in Table 11. An XPS survey scan of a pretreated catalyst is shown in Figure 14. The results of the XPS are tabulated in Table 13. The increase of N surface atomic content provided further evidence for the increase of N content in N-doped carbon with the ammonia treatment temperature.

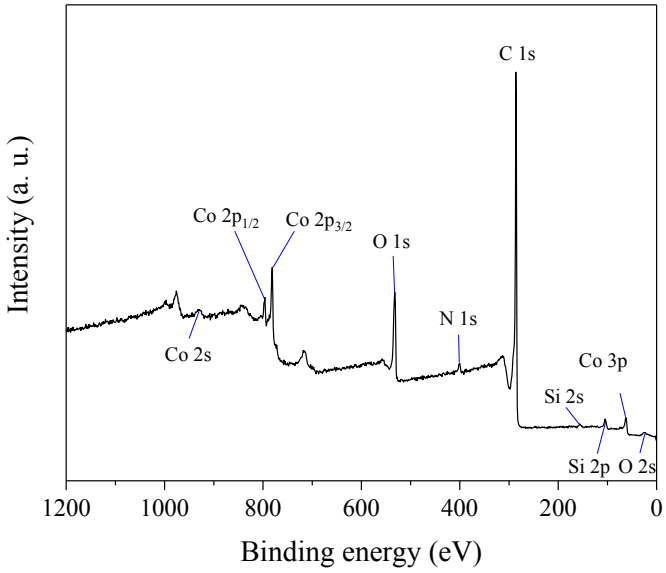

Figure 14. XPS survey scan of 600A-CoOx/N-C.

Table 13. Atomic content of catalysts from XPS survey scan

Element	2A-CoOx/N-C	200A-CoOx/N-C	400A-CoOx/N-C	600A-CoOx/N-C	800A-CoOx/N-C
C (%)	69.88 ± 0.49	78.22 ± 0.40	76.76 ± 1.62	78.93 ± 0.21	79.04 ± 1.28
Co (%)	5.69 ± 0.40	2.67 ± 0.07	3.61 ± 0.40	3.21 ± 0.32	2.72 ± 0.70
N (%)	2.26 ± 0.09	2.67 ± 0.32	3.10 ± 0.53	2.95 ± 0.09	2.82 ± 0.10
O (%)	17.44 ± 0.49	13.72 ± 0.18	14.13 ± 0.23	12.31 ± 0.17	12.36 ± 0.65
Si (%)	4.75 ± 0.28	2.72 ± 0.33	3.41 ± 0.47	2.61 ± 0.68	3.06 ± 0.25

A shift of the N1s binding energy to lower values with increasing NH_3 treatment temperature is observed in the XPS of N1s shown in Figure 15. Deconvolution of the N1s spectra further revealed the presence of six types of nitrogen species for each catalyst (Figure 16a-e). N1s spectra were taken for three different spots for each sample to get statistically relevant data. The six different types of nitrogen species are shown in (Figure 16f. The binding energies (eV) of the six nitrogen species are as follows: N1, 398.4 ± 0.1; N2, 399.3 ± 0.1; N3, 400.5 ± 0.1; N4, 401.9 ± 0.1; N5, 403.7 ± 0.2; N6, 405.8 ± 0.2. These binding energies were fixed in analyzing the concentration of different nitrogen species. The N1 species with binding energy below 399 eV are assigned to pyridine.[41,66-69] N2 species with binding energy between 399 and 400 eV are assigned as an amide,[66,70,71] amino[72] or nitroso functionality.[73] N3 corresponds to pyrrole-like N, a 3-fold coordinated N atom in a pentagonal ring.[41,54,68,70,74] N4 is usually assigned to quaternary/graphitic N, a nitrogen atom substituting a C atom in graphene structure.[41,68-70,74] At the higher binding energy region (>403eV), N5 and N6 are assigned to pyridine oxide and nitro groups respectively where nitrogen atoms are bonded to oxygen atoms.[73,75]

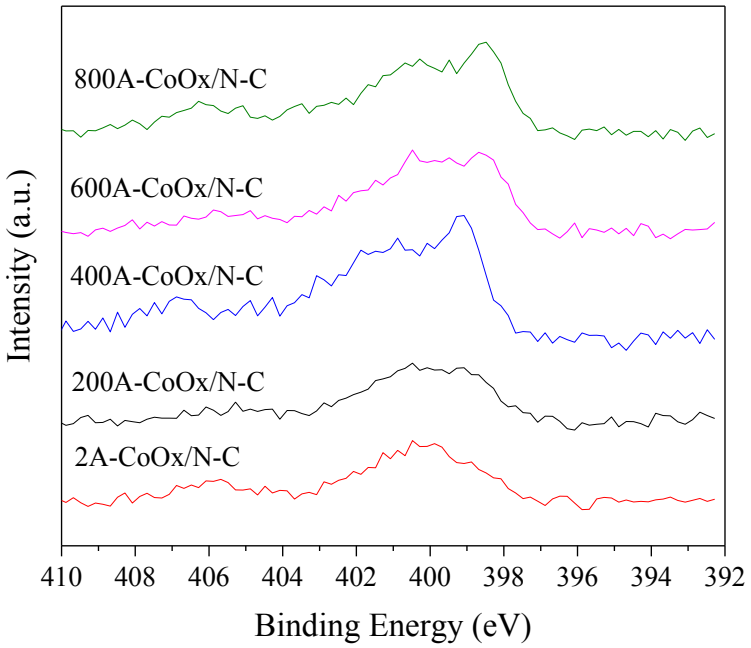

Figure 15. N1s XPS spectra of 2A-CoOx/N-C, 200A-CoOx/N-C, 400A-CoOx/N-C, 600A-CoOx/N-C and 800A-CoOx/N-C after treatment at 230 ^{o}C for 2 h in helium

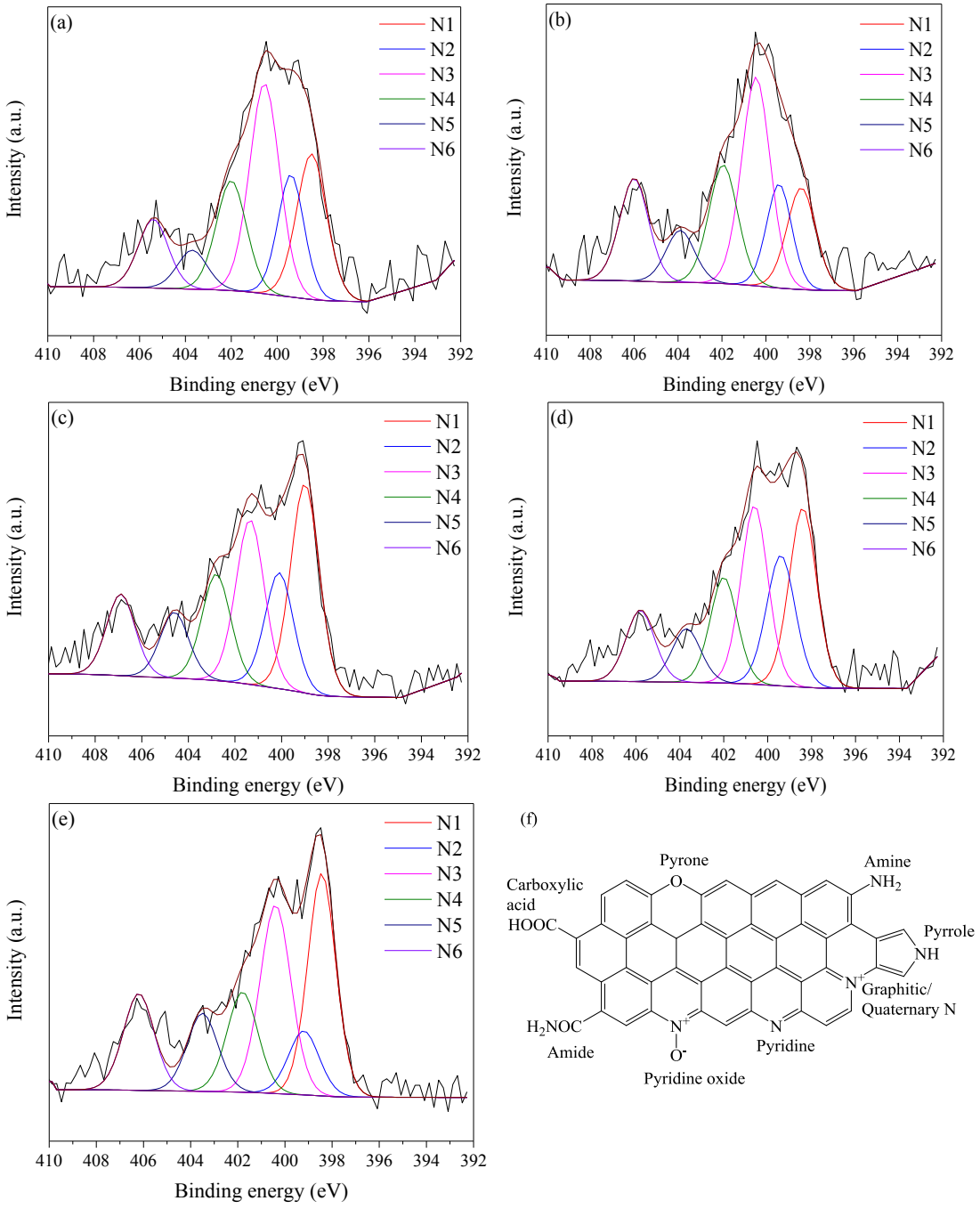

Figure 16. Deconvolution of N1s XPS spectrum of (a) 2A-CoOx/N-C, (b) 200A-CoOx/N-C, (c) 400A-CoOx/N-C, (d) 600A-CoOx/N-C, (e) 800A-CoOx/N-C and (f) N functionalities in carbon materials (adapted from Arrigo *et al.*[48])

XPS spectra were also collected for the ammonium hydroxide treated carbon (AC), nitric acid treated carbon (AWC), and N-doped carbon synthesized at different temperatures in NH_3 (200A-N-C, 400A-N-C, 600A-N-C, 800A-N-C) as shown in Table 14, Table 15 and Figure 17. Table 14 summarizes the surface elemental atomic content of these six materials. Table 14 shows an increase in the N surface atomic content with increasing ammonia treatment temperature. The deconvolution of N1s spectra in N1-N6 is shown in Figure 17 and their content in Table 15. The most abundant nitrogen species in AWC (Figure 17b) is N6. It has been shown that nitric acid treatment of activated carbon introduces nitro functionalities.[48,69] Under NH_3 environment at low temperatures (<400 ^oC), nitrogen insertion occurs via the reaction between NH_3 and carboxyl groups to form amide groups ($(C=O)NH_2$). At higher NH_3 treatment temperatures, the amide groups are likely to undergo dehydration or decarbonylation to form pyridine or pyrrole groups.[48] Since N2 is the dominant species in 200A-N-C and 400A-N-C (Figure 17c-d), N2 probably corresponds to amide-like N. As the NH_3 treatment temperature increased, the N2 content decreased, accompanied by the increase in N1 content (Figure 17e-f).

Table 14. Atomic content of supports from XPS survey scan

Element	AWC	AC	200A-N-C	400A-N-C	600A-N-C	800A-N-C
C (%)	87.8	92.6	87.3	84.9	89.7	89.9
O (%)	10.0	5.3	8.0	9.0	5.1	5.2
N (%)	1.1	0.9	2.9	3.4	3.4	3.6
Si (%)	1.0	1.1	1.2	2.4	1.3	1.1

Table 15. Nitrogen species content of supports from deconvolution of N1s spectra (%)

Nitrogen species	BE (eV)	AWC	AC	200A-N-C	400A-N-C	600A-N-C	800A-N-C
N1	398.3 ± 0.1	0.11	0.08	0.37	0.68	1.06	1.30
N2	399.3 ± 0.2	0.13	0.08	0.89	1.15	0.83	0.38
N3	400.6 ± 0.2	0.26	0.11	0.76	0.76	0.77	0.94
N4	401.9 ± 0.1	0.19	0.26	0.32	0.38	0.35	0.47
N5	403.5 ± 0.2	0.16	0.14	0.24	0.27	0.22	0.31
N6	405.5 ± 0.2	0.06	0.44	0.32	0.16	0.17	0.21

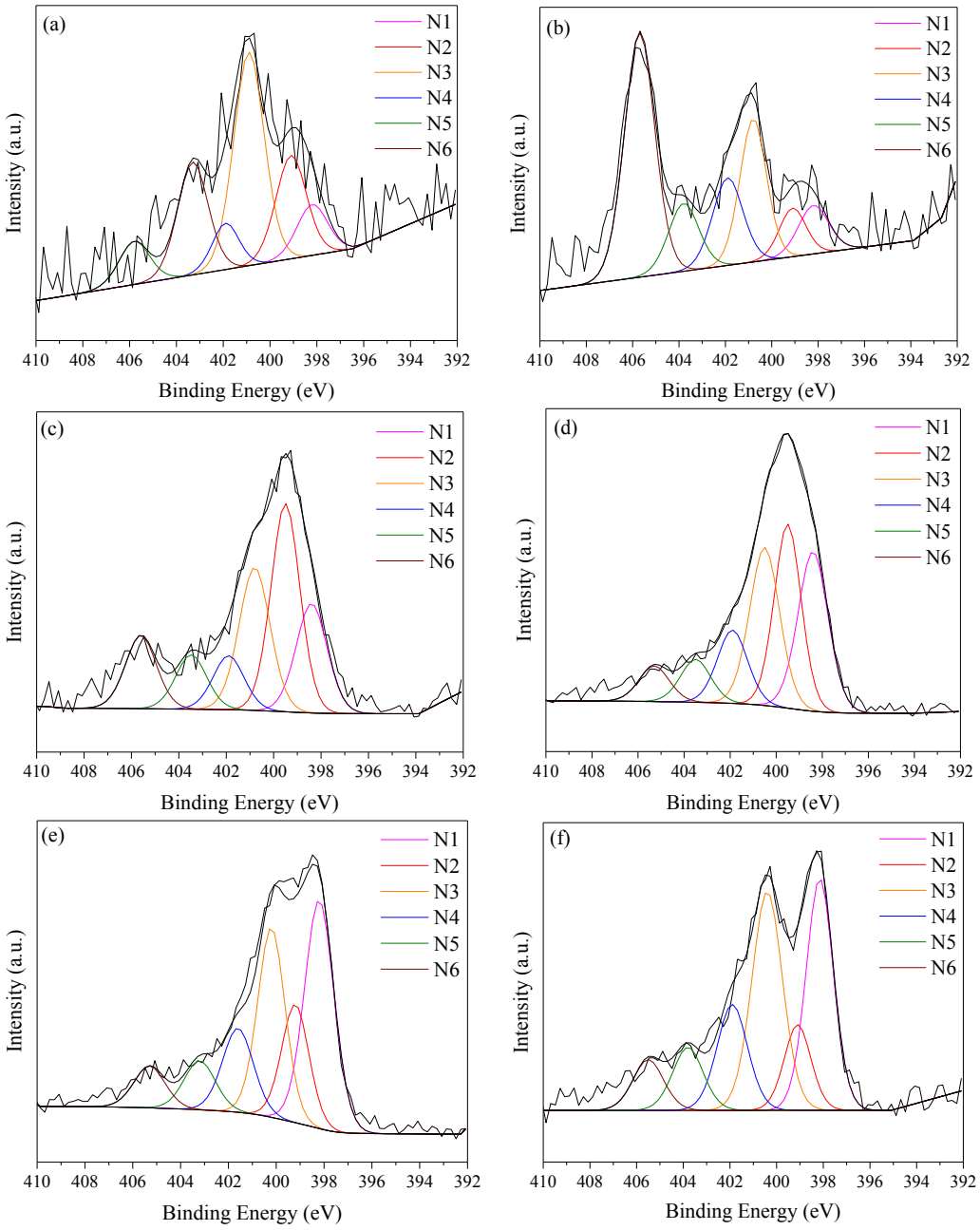

Figure 17. Deconvolution of N1s XPS spectrum of (a) ammonia solution treated carbon (AC), (b) nitric acid washed carbon (AWC), (c) acid washed carbon treated with ammonia gas at 200 ºC (200A-N-C), (d) acid washed carbon treated with ammonia gas at 400 ºC (400A-N-C), (e) acid washed carbon treated with ammonia gas at 600 ºC (600A-N-C), (f) acid washed carbon treated with ammonia gas at 800 ºC (800A-N-C)

Table 16 lists the content of the nitrogen based species in the catalysts at different binding energies. Figure 18a shows the variation in atomic percentage as a function of the NH_3 treatment temperature. The N1 species concentration increases with NH_3 treatment temperature. The N1 species is the most abundant nitrogen species in the 800A-CoOx/N-C catalyst. The abundance of N2 initially increased with NH_3 treatment temperature (200 ^oC to 400 ^oC) but decreased as the temperature increased further (600 – 800 ^oC). This indicates that the N2 (amide) is converted into other nitrogen species at higher temperature. The N3 species also decreased with increasing temperature. Arrigo *et al.* [76] have shown that N3 (pyrrole) can be converted to pyridine (N1) above 400 ^oC.[76]

Table 16. Nitrogen species content of catalysts from deconvolution of N1s spectra (%) [a]

Nitrogen species	BE (eV)	2A-CoOx /N-C	200A-CoOx /N-C	400A-CoOx /N-C	600A-CoOx /N-C	800A-CoOx /N-C
N1 (pyridinic nitrogen)	398.40 ± 0.10	0.37	0.40	0.63	0.71	0.78
N2 (amide)	399.30 ± 0.10	0.54	0.36	0.54	0.55	0.37
N3 (pyrrole/pyridone)	400.50 ± 0.10	0.57	0.82	0.81	0.68	0.67
N4 (quaternary nitrogen)	401.90 ± 0.10	0.39	0.47	0.44	0.49	0.38
N5 (pyridine oxide)	403.70 ± 0.20	0.18	0.21	0.24	0.22	0.24
N6 (nitro)	405.80 ± 0.20	0.22	0.40	0.29	0.30	0.37

a. Calculated from the product of nitrogen surface abundance from XPS survey scan and percentage of specific N species among all nitrogen species.

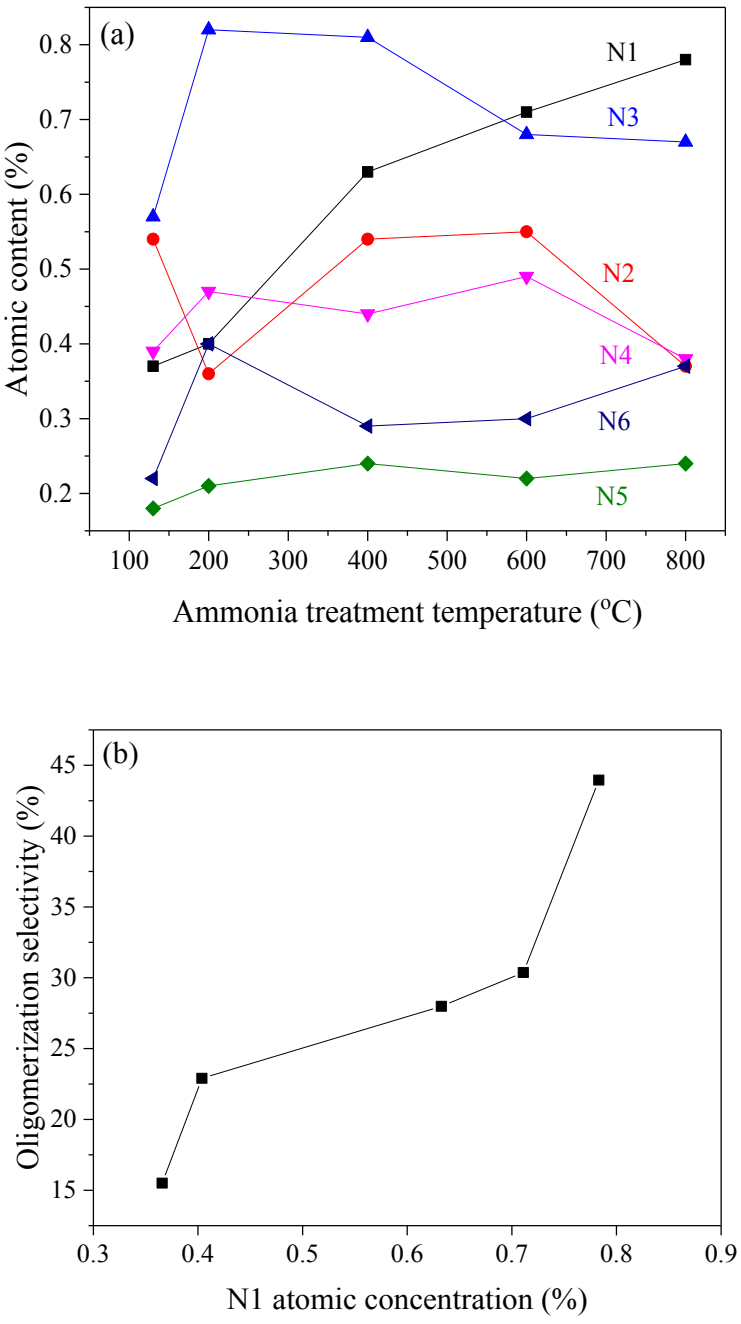

Figure 18. (a) Atomic content as a function of ammonia treatment temperature for the six nitrogen species. (b) Oligomerization selectivity as a function of N1 atomic concentration

3.3.3 Discussion of the role of N species

Figure 18 shows that the oligomerization selectivity increases with an increasing pyridinic N (N1) content in the catalyst. The oligomerization selectivity has no clear correlation to the amount of N2-N6. We can thus infer that the increase of oligomerization activity with N1 content is induced by some type of interaction between the nitrogen species and supported cobalt oxide nanoparticles. This interaction appears to stabilize (or increase the concentration of) the intermediates after initial 1-butene insertion and promotes chain growth (relative rate of chain growth closer to that of β-hydrogen elimination). This increase in oligomerization activity of the Co_3O_4 particles with an increased pyridinic N content could be due to two reasons: 1) The pyridinic N stabilizes smaller Co_3O_4 particles which increases the oligomerization activity or 2) the pyridinic N induces an electronic effect to the Co_3O_4 particles. No difference in Co_3O_4 crystallite size was detected with XRD, however smaller crystallites (<4nm) cannot be detected with this method.[35] In addition, as shown by Munnik *et al.*[63] and Borg *et al.*,[64] XRD does not accurately measure Co_3O_4 particle size, which is more important than crystallite size in determining activity. In their work, aggregates (or particles) of cobalt oxide crystallites were observed for cobalt oxide on silica from TEM. The aggregate size is different from crystallite size measured by XRD. Attempts to investigate the morphology of these catalysts with TEM were unsuccessful due to overlapping of cobalt oxide particles at high cobalt loading and the poor contrast between the cobalt oxide and the carbon support.[35]

Several researchers have reported that there is an electronic effect between N-doped carbon and metal and metal-oxide nanoparticles. Wang *et al.*[65] reported that Co(III) is partially reduced to Co(II) for CoOx on N-doped graphene. In this study, the interaction between cobalt oxide nanoparticles and N-doped graphene was suggested by the less resolved π^* feature and significantly reduced $\sigma^*_{C\text{-}N}$ feature in the N K-edge XANES spectra of the hybrid material. The partial reduction of Co_3O_4 to CoO was determined by a reduction in intensity and shift of Co 3d/O 2p peak in the O K-edge as well as the appearance of CoO state in the Co L-edge and the Co K-edge XANES. Similar interactions between pyridinic N and cobalt oxide was reported by He *et al.*,[38] where cobalt oxide coupled with N-doped graphene was investigated for ORR. The XAS of N K-edge and DFT calculations suggested that the pyridinic nitrogen stabilized Co(II). Arrigo *et al*.[54] studied the N–Pd interaction in Pd nanoparticle (<5 nm) supported on N-doped carbon nanotubes catalysts. They used NEXAFS of N K-edge to show that pyridine-like nitrogen induces charge localization on the N atom and a charge transfer between N and metal sites. The change in Pd oxidation state induced by this charge transfer was further confirmed by XPS analysis of Pd 3d core level spectra. Liu *et al.*[77] studied $ZnCo_2O_4$ particles (~3.5 nm) on N-doped carbon nanotubes for oxygen reduction reactions (ORR). They proposed that the C=N functional group lead to electron cloud migration at the metal oxides and support interfaces. These electronic interactions between metal/metal oxide and nitrogen species were observed via the analysis of N K-edge and Co L-edge. However, we did not observe a significant difference in cobalt

oxidation state between different N containing catalysts with increasing pyridinic nitrogen content from XAS analysis of the Co K-edge.

3.4 Conclusions

N-doped carbon materials were synthesized via functionalization with NH_3 at high (200-800 ^oC) temperatures. Cobalt oxide was added by impregnation to the N-doped carbon supports and tested for 1-butene oligomerization. Over 70% of the oligomer products were linear olefins. 2-butene was a major by-product from the reaction where the ratio between 1-butene and 2-butene approached equilibrium as the conversion increased. The oligomerization selectivity increased with increasing NH3 treatment temperature. Cobalt oxide on N-doped carbon synthesized at 800 ^oC has a 2.6 times increase in the oligomerization selectivity compared to previously reported catalysts where the N-doped support was prepared by NH_4OH aqueous treatments. The oligomerization selectivity increased with increasing 1-butene conversion. The total nitrogen content in the catalyst bulk phase increased from 1.13 to 2.21 wt.% with increasing ammonia treatment temperature from 200 ^oC to 800 ^oC. The oligomerization selectivity increased with pyridine-type N species.

Chapter 4. Summary and Future Work (I)

4.1 Summary of light olefin oligomerization over cobalt oxide on N-doped carbon

Chapter 2 and 3 present the effect of pretreatment temperature and nitrogen functionalities on the catalytic activity of cobalt oxide on N-doped carbon catalysts for light olefin oligomerization. High linear dimer selectivity (>70%) was observed for all the catalysts studied. 1-butene undergoes double bond isomerization and oligomerization simultaneous over this class of catalysts. The oligomerization yield decreases with the catalyst pretreatment temperature characterized by partial reduction of the cobalt oxide species. On the other hand, the oligomerization selectivity increased with increasing NH_3 treatment temperature characterized by increased pyridine-type N species. Cobalt oxide on N-doped carbon synthesized at 800 ^oC has a 2.6 times increase in the oligomerization selectivity compared to where the N-doped support was prepared by NH_4OH aqueous treatments.

The pretreatment temperature influences the catalyst activity by changing the overall 1-butene conversion, whereas the pyridine nitrogen promotes oligomerization selectivity over isomerization at similar overall 1-butene conversion levels.

4.2 Proposed future work for olefin oligomerization over heterogamous catalysts

One of the key challenges of this study is that the active surface species has not been identified. This is particularly challenging with a metal oxide, like cobalt oxide, where the nitrogen species on the support influences the catalytic chemistry. Currently it is not clear if the active phase is Co(II), Co(III), a cobalt hydride or some specific orientation on the cobalt oxide plane. Schultz *et al.* postulated that a cobalt hydride species could be the active site for ethylene, propylene, and 1-butene oligomerization on cobalt oxide on N-doped carbon catalysts.[24,25,78] *In situ* FTIR could be used to investigate the presence of Co-H vibrations. By substitution with D-labeled ammonia sources, identification this potential site could be further verified. Additionally, FTIR with probe molecules, such as CO, will allow the quantification of different cobalt oxidation states. The use of CO adsorption at low temperatures has been applied to cobalt ions in ferrierite to quantify the different cobalt oxidation states. Chakarova and Hadjiivanov observed distinct Co^{2+}-CO (bands at 2199 and 2196 cm^{-1}) and Co^{3+}-CO (2204 cm^{-1}) in the range of 100-300K.[79]

Although a positive correlation was observed between the surface atomic concentration of pyridine like nitrogen and oligomerization selectivity, a change of the cobalt phase has yet to be precisely characterized from the XRD, XPS or Co K-edge XAS. Researchers have proposed electron migration and charge transfer between the surface nitrogen species and supported metal or metal oxide. This charge transfer effect was observed in

N K-edge and Co L-edge XAS spectra. Future analysis of the bonding orbitals (N K-edge and Co L-edge) would likely provide more conclusive evidence of this proposed Co-N interaction. Nitrogen extended x-ray adsorption fine structure (EXAFS) region will provide insight into the N-Co coordination, which we expect to correlate with activity. Liang *et al.* successfully used a similar method to probe the C and O K-edge and Co L-edge to explain the enhanced oxygen reduction activity of Co_3O_4/graphene oxide doped with nitrogen.[80] Moreover, *In situ* XPS can be used in conjunction with XAS to further characterize the surface properties of the catalyst samples compared to the current *ex situ* XPS data. Jin *et al.* were able to use XPS to quantify the surface states of cobalt oxide N-doped carbon catalysts as bifunctional water splitting catalysts.[81] They postulated that the addition of N into the carbon support was able to donate electron density that could be the cause of the increased activity. The *in situ* XPS study could be done by pretreating all catalysts samples in an inert environment and transferred via a vacuum transfer module chamber (Thermo Fischer Scientific) to avoid contamination or reaction with air. This eliminates the influence of air on the cobalt oxide species because small shifts in binding energy are important in identifying the change of cobalt phase.

Albeit the 2.6 times increase in the oligomerization selectivity due to the introduction of nitrogen functionalities, only 1-2% additional nitrogen species were introduced with NH_3 treatment of activated carbon. Post synthetic treatment of carbon materials can only introduced limited amount of nitrogen functionalities because nitrogen-containing functional groups developed in such a way are often unstable and mainly distributed on

certain anchoring sites on the surface.[82] One can postulate perhaps N-doped carbon type support with even more nitrogen functionalities would lead to a greater increase of oligomerization selectivity and more measurable change to the cobalt phase. A number of other methods for the synthesis of metal or metal oxide catalysts supported on N-doped carbon materials have been reported in recent studies with improved catalytic activity, selectivity and stability. These methods include 1) N-doped mildly reduced graphene oxide, 2) soft templating method with nitrogen and carbon source to synthesize N-doped mesoporous carbon and 3) catalytic chemical vapor deposition (CCVD) of nitrogen-containing hydrocarbon over supported transition metal catalysts to synthesize N-doped nanocarbon. Future work could focus on synthesis of this class of metal oxide on N-doped carbon catalysts with these different methods and establish a universal correlation between catalytic activity and nitrogen species descriptor.

Cobalt oxide on N-doped, reduced-mildly oxidized graphene oxide (Co_3O_4/N-rmGO) has been recently reported to have high activity in electrocatalysis.[38-40] Liang *et al.* synthesized Co_3O_4/N-rmGO by a general two-step method. The first step involved growing Co_3O_4 nanoparticles on mildly oxidized graphene oxide (mGO) from cobalt acetate in NH_4OH solution. The second step involved hydrothermal reaction leading to crystallization of Co_3O_4 and reduction of mGO. This Co_3O_4/N-rmGO catalyst exhibited comparable oxygen reduction reaction (ORR) activity to a fresh, commercial, state-of-art Pt/C catalyst in alkaline solutions.

N-doped mesoporous carbon (NMC) can be synthesized by a soft-templating method. Wang *et al.* [41]studied PtCo/NMC catalysts for biophenolics upgrading. The NMC was prepared, using 3-aminophenol as both nitrogen and carbon source, via ordered assembly between 3-aminophenol/formaldehyde resin and polyethylene oxide (PEO), followed by pyrolysis. By controlling the polymerization rate, the selective formation of NMC with 2D hexagonal or 3D cubic symmetry was achieved. Bimetallic PtCo nanoparticles on the NMC were uniformly distributed with diameters of around 1.5 nm. Catalytic hydrodeoxygenation of lignin over the PtCo/NMC catalyst produced cycloalkanes.

Another synthetic route to obtain N-doped nanocarbon (N-NC) is based on the Catalytic Chemical Vapor Deposition (CCVD) of nitrogen-containing hydrocarbons over supported transition metal based catalysts.[42,43] Nitrogen-containing carbon nanotubes (NCNT) can be grown from acetonitrile, pyridine or N,N-dimethylformamide over supported Fe, Co or Ni catalysts. The work by Van Dommele *et al.*[43] showed that the C/N ratio increases with increasing synthesis temperature from 550ºC to 850ºC. They also reported that the type of nitrogen changed with increasing temperature from predominantly pyridinic N to quaternary N.

SECTION II: THE CHEMISTRY AND KINETICS OF POLYETHYLENE PYROLYSIS: A FEED STOCK TO PRODUCE FUELS AND CHEMICALS

Chapter 5. The Chemistry and Kinetics of Polyethylene Pyrolysis: A Feedstock to Produce Fuels and Chemicals

5.1 Introduction

Plastics are ubiquitous in many sectors of manufacturing due to their low cost and unique properties.[8,10,83] Plastics production has grown tremendously since 1950s making them the most abundantly produced man-made material.[10] Global annual plastic production has increased by 620% since 1975 and reached 288 million metric tons (Mt) in 2012.[8,9] As a result, the share of plastics in municipal solid waste increased from less than 1 wt.% in 1960 to more than 10 wt.% by 2005 in middle and high income countries. [10] It was estimated that between 1950 and 2015 a total of 8,300 Mt of plastics had been produced with 6,300 Mt of plastic waste. Only 9% of these plastic waste has been recycled and 12% incinerated, with 79% was accumulated in landfills or the natural environment.[10] Moreover, the rising global plastic pollution was paralleled by significant increase in plastic marine debris. [9,84] An estimated 4 to 12 Mt of plastic waste generated on land ended up in the marine environment in 2010 alone. Marine debris is one of the world's most pervasive pollution problems affecting the oceans. None of the commodity plastics produced from petroleum or natural gas are biodegradable.[9,10,84] The accumulation of near-permanent plastic waste contamination is a growing concern. There is a critical society need to develop economical technology that can efficiently re-use waste plastics as either higher value chemical feedstocks or lower value liquid transportation fuels.

Pyrolysis is a promising option for conversion of waste plastics into either fuels or commodity chemicals. Pyrolysis is the process of thermally degrading long chain polymer molecules into smaller molecules through heat and pressure. There has been growing interest in studying pyrolysis in converting biomass over the last 30 years. [85-88] Waste plastics have a lower oxygen content and higher carbon content than biomass, giving them the potential to produce higher yields of liquid hydrocarbons. Pyrolysis of plastic polymers can produce up to 80 wt.% of liquid oil.[85,88,89] Furthermore, pyrolysis technologies have lower capital costs and operating than gasification technologies.[90] Researchers have studied the influence of various operating parameters (including temperature, reactor type, residence time, pressure, catalyst, and fluidizing gas composition and flowrate) on the distribution of overall product yields for pyrolysis of a number of plastics.[8,91] However, there is no fundamental mechanistic model for plastic pyrolysis. Most of the models incorporate single-step reaction kinetics where the products are lumped into three main categories (char, tar and gas).[92] In addition, from the perspective of identifying value-added end-uses, the liquid oils produced from waste plastics have not been fully analyzed.

In attempts to develop a fundamental model for plastic pyrolysis in reactor systems, the first step is to describe the thermal degradation of polymers in terms of "intrinsic" kinetics, where heat and mass transfer limitations are not present. Thermogravimetric analysis (TGA), through measurements of mass volatilized as a function of temperature, is a commonly used method for measuring the kinetics of thermal

degradation reactions.[92-94] Simplified solid state reaction models have been proposed in the literature for modelling TGA of plastics, where the solid is considered as a single homogeneous species. However, these empirical functions fail to describe the fundamental polymer degradation mechanism with theoretical justifications.[95,96]

Among hundreds of plastic materials that are commercially available, poly-olefins contribute to more than 48% of the world plastic demand with 30% of the plastics being polyethylene (PE).[83] The thermal degradation of poly-olefins has been described by a single step model of the solid species in the form of Arrhenius n^{th} order rate equations.[92,93] Some researchers have proposed that these polymers degrade via random scission model, but no intrinsic model with specific kinetic parameters has been proposed nor have the models been used to predict the pyrolysis product yields.

In this chapter we develop a predictive model that describes both the activity and product selectivity for pyrolysis of PE. The intrinsic pyrolysis of PE are studied in a TGA. A random scission model, with two parallel first order reactions, is fit to the TGA data. PE pyrolysis in a fluidized bed reactor is studied at a temperature range of 500-600^{o}C and residence time of 12.4 – 20.4 s. The gas and liquid products analysis results are analyzed.

5.2 Experimental

5.2.1 TGA experiments

Thermogravimetric analysis (TGA) and derivative thermogravimetric (DTG) data were acquired using a TA Instruments SDT Q500 system. Nitrogen was used as the sweep gas. Experiments were conducted with different nitrogen flowrates (25-100 mL/min), different sample weights (5-20 mg), different particle sizes (150-355 μm) and two different molecular weights (Sigma-Aldrich). The properties of the two types of polyethylene are shown in Table 17. Both PE samples have density in the range of 0.910–0.940 g/cm^3 and are classified as low-density polyethylene (LDPE). PE with density range of 0.93 to 0.97 g/cm^3 is defined as high-density polyethylene (HDPE).

Table 17. Properties of polyethylene used in TGA analysis

	PE4000	PE35000
Weight average molecular weight (Mw)	4000	35000
Molar average molecular weight (Mn)	1700	7700
Density at 25 °C (g/mL)	0.920	0.906

5.2.2 PE4000 pyrolysis in the fluidized bed reactor

Thermal pyrolysis of PE4000 was performed in a fluidized-bed reactor system, as shown in Figure 19.[97] The fluidized bed reactor is a 316L stainless-steel 4.92 cm I.D. pipe with a freeboard height of 37 cm. Above the freeboard is a disengagement zone which expands to a 7.79 cm I.D. pipe. The reactor is filled with silica sand of which the static height is 15cm. The silica sand bed is supported by a distributor plate made from two layers of 304 stainless-steel cloth (200 mesh) glued to a stainless-steel screen for support. The main reactor body and space beneath the distributor plate (referred to as the plenum) were sealed together using bolted flanges with a graphite gasket. The reactor and plenum were heated to a target temperature of 500-600 °C using semi-circular ceramic heaters (WATLOW). The flanges joining the main reactor body and plenum were heated using a band heater. Heating zone temperatures were controlled by thermocouples located between the reactor body and heaters.

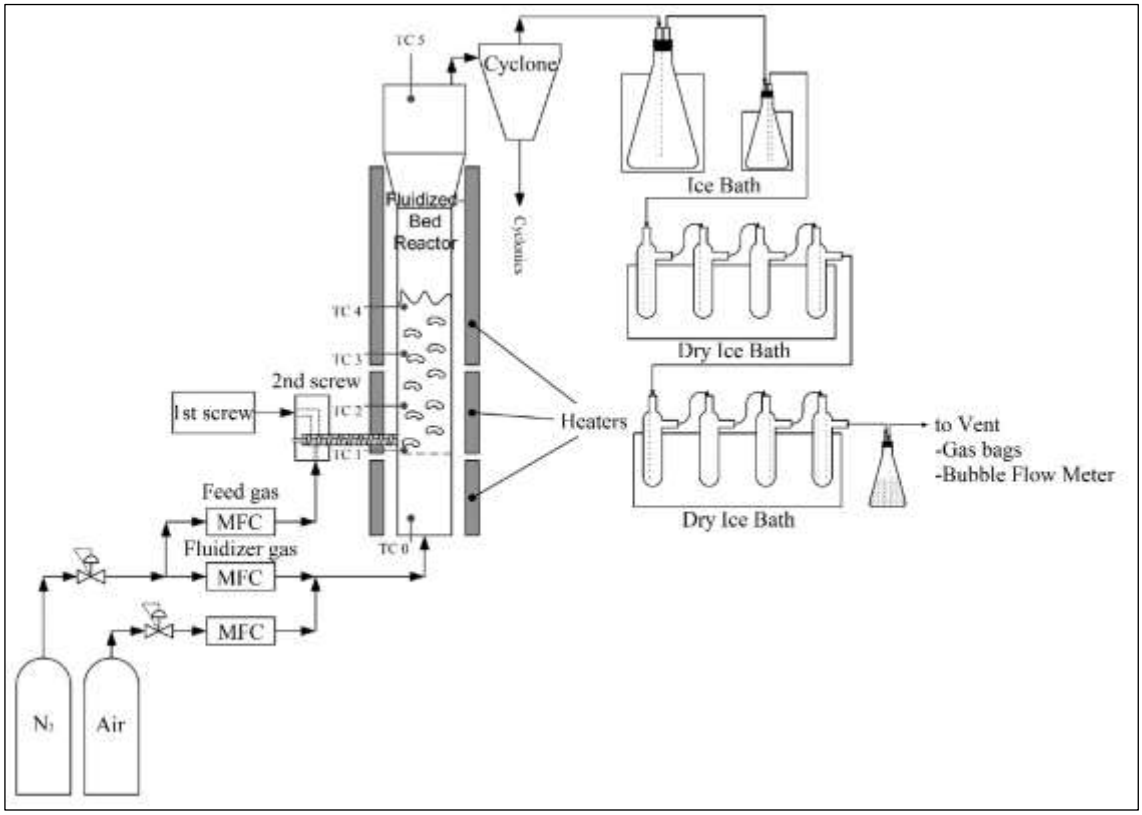

Figure 19. Schematic of fluidized bed reactor used for PE pyrolysis

A typical reaction was carried out over a duration of 1 hour time-on-stream. The operation conditions are summarized in Table 18. Eq. 13, 14, and 15 describe how the weight hourly space velocity (WHSV), sand contact time and residence time were calculated. The fluidized bed operating conditions were chosen to be similar to those used by other researchers investigating the pyrolysis of plastic wastes.[98-101] The silica sand was fluidized with nitrogen, the fluidizer gas, at a rate of 330-2000 standard cubic centimeter per minute (sccm) to achieve residence times of 12.4-20.4 s. Heating of the plenum allowed for pre-heating of the fluidizer gas to the reaction temperature before reaching

the sand. A stainless-steel auger equipped with a variable speed motor and rotary fitting fed PE4000 into the reactor from the side. Polyethylene feed was supplied to this auger via a sealed feed hopper (calibrated prior via balance and stopwatch). To maintain an inert environment and encourage the rapid delivery of feed to the reactor, the hopper and augur were swept with nitrogen, the feed gas, at a rate of 300 sccm. During the reaction, product gases exited the top of the reactor and were passed through a cyclone where entrained solids were removed. The solid-free vapors were condensed in two condensers maintained at 0 °C using an ice bath. The stream was then passed through eight condensers maintained at −78 °C using a dry-ice/acetone bath to condense residual organics. The non-condensable gases were then either vented, plumbed through a bubble flow meter, or sampled in Tedlar gas bags (Restek) for GC analysis. At the conclusion of PE feeding, the reactor was purged with nitrogen for another 30 min to ensure a complete purge of all volatile organic products. The liquid product was then collected from the condensers and analyzed by GC-FID.

Table 18. Operating conditions of FB reactor

	Other studies	This study
PE4000 feed rate (g/min)	0.2-3[98-100]	2.0
Silica sand particle size (μm)	70-140[98-100]	100-180
Static bed depth (cm)	10[98]	15
WHSV (h^{-1})	NA	0.27
Sand contact time (s)	NA	1350
Residence Time (s)	15[98]	12.4 – 20.4

$$WHSV\ (h^{-1}) = \frac{PE\ mass\ feed\ rate\ (g{\cdot}h^{-1})}{mass\ of\ sand\ (g)} \quad \text{(Eq. 13)}$$

$$Sand\ contact\ time\ (s) = \frac{mass\ of\ sand\ (g)}{PE\ mass\ feed\ rate\ (g{\cdot}s^{-1})} \quad \text{(Eq. 14)}$$

$$Residence\ time\ (s) = \frac{volume\ of\ reactor - volume\ of\ sand\ (cm^3)}{output\ volumetric\ flow\ rate\ at\ rection\ temperatures\ (cm^3{\cdot}s^{-1})} \quad \text{(Eq. 15)}$$

After the reaction, the reactor was cooled to room temperature and a small amount of bed material was taken out of reactor for characterization. The reactor temperature was then increased to 600 °C, and the carrier gas was switched to air to oxidize the char that

remained in the reactor. The sand was typically exposed to air for approximately two hours to ensure combustion of all organic species remaining in the reactor.

5.2.3 Product analyses

During the reaction, the gas product was collected in gas bags and analyzed with Refinery Gas Analyzer GC-2014 (Shimadzu). The column temperature was initially held at 40 ^{o}C for 2 min, then ramped to 120 ^{o}C at 30 ^{o}C/min, held at 120 ^{o}C for 4 mins, ramped to 150 ^{o}C at 30 ^{o}C/min and finally held at 150 ^{o}C for 4 mins.

The liquid products in all condensers were mixed, dissolved in dodecane (1:10 wt.) and analyzed in GC2010 Plus-FID (Shimadzu) with MXT-1 (5m×0.53mm×0.1μm) column. The column temperature was initially held at 40 ^{o}C for 5 min, then ramped to 415 ^{o}C at 15 ^{o}C/min, and finally held at 415 ^{o}C for 5 mins. The flame ionization detector (FID) was programmed to hold at 425 ^{o}C. The liquid product was also dissolved in hexane (1:10 wt.) so that the composition of C12 compound can be analyzed.

After the reaction, the reactor was purged and cooled down, then a small amount of silica sand was taken out of reactor for total organic carbon (TOC) measurement. The measurement was performed with TOC-V_{CPH} analyzer with SSM-5000A solid sample module. The sample was combusted at 900 ^{o}C in flowing oxygen in the solid sample module and the effluent was converted to CO_2 over catalyst and measured with a nondispersive infrared (NDIR) sensor. The equipment was calibrated to a potassium hydrogen phthalate prior to the measurements.

Nitric oxide ionization spectroscopy evaluation (NOISE) was carried out by Triton Analytics Corporations for the liquid product from PE4000 pyrolysis at 550 ^{o}C with a residence time of 17.9 s. In the NOISE analysis, samples are first separated by boiling points. This segregates molecules and helps distinguish compounds with traditional reporting categories. Boiling point fractions are then bombarded with "soft" NO^{+} ions. Mass spectrometry identifies each component and reports by boiling region and degree of saturation. The NOISE report gives percentages by boiling point and by Z-number (for C_nH_{2n+z}) where Z distinguishes between paraffins, cycloparaffins, mono-, di-, and tri-aromatics.

5.3 Results and Discussion

5.3.1 TGA of PE4000 and PE35000

Figure A6 shows the TGA and DTG results of PE35000 at nitrogen flowrate of 25-100 mL/min with fixed particle size (180-250μm), initial mass (10mg), and heating rate (10 ^{o}C/min). PE35000 begins to decompose at about 300 ^{o}C. Most of the mass loss occurs between 300 ^{o}C and 460 ^{o}C, with the maximum mass loss 87emolytic at about 440 ^{o}C. Different nitrogen flowrates have negligible influence on the TGA and DTG pattern, indicating minimal heat transfer limitations at these conditions.[102] A flow rate of 50 mL/min was chosen for the kinetic study. Figure A7 shows that no interparticle heat or

mass transfer limitation is present with initial mass ranging from 5 mg to 20 mg.[103] Initial sample mass of 10 mg was adopted for all other TGA experiments. Figure A8 shows the TGA and DTG results of PE35000 with different particles sizes with fixed initial mass (10mg), sweep gas flowrate (50mL/min) and heating rate (10 ºC/min). Particle to fluid transport can depend on both particle size and sweep gas flowrate. In this study, particle size has negligible influence on the TGA and DTG pattern, indicating particle to fluid heat or mass transfer limitations are not present in the studied range of particle sizes. Particle size of 180-250 μm was adopted for all other TGA experiments.

The TGA and DTG of PE4000 and PE35000 are shown in Figure 20. For both samples, most of the mass loss occurs between 300 ºC and 460 ºC, with the maximum mass loss rate at about 440 ºC. Decomposition patterns of the two samples are the same, suggesting that thermal decomposition mechanisms do not depend on molecular weight of the polyethylene. This pattern has been observed for other polymers. For example, Khairuddin *et al.*[104] observed similar decomposition patterns in TGA of polyethylene glycol (PEG) of different molecular weight (PEG400 and PEG600).

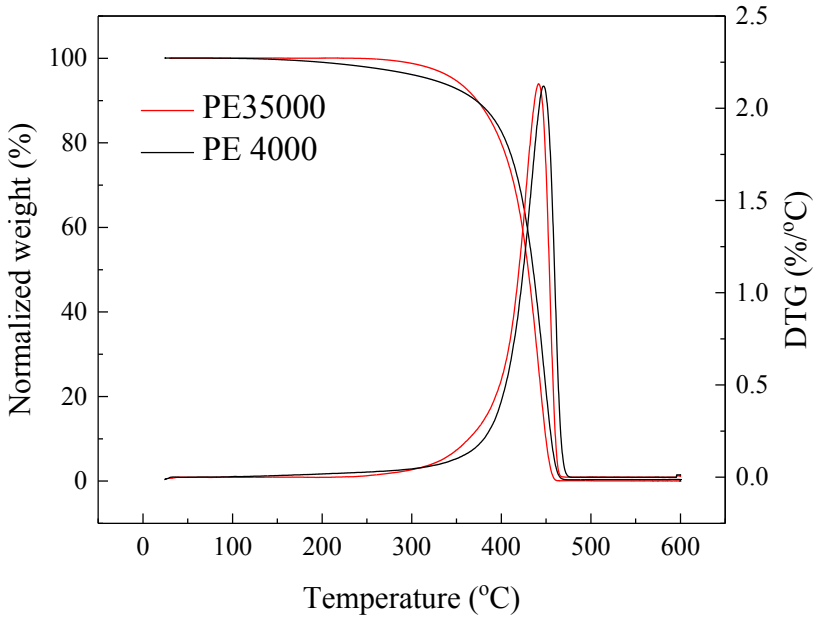

Figure 20. Thermal decomposition of PE4000 and PE35000 (particle size: 180-250 µm, initial mass: 10mg, sweep gas flow rate: 50mL/min, heating rate: 10 °C/min)

5.3.2 Pyrolysis of PE4000 in the fluidized bed reactor

Table 19 shows the product yields (gas, liquid and char products) for pyrolysis of PE4000 in the fluidized bed reactor at temperatures from 500 to 600 °C. Mass balance closure ranges from 87.1% to 98.2%. Gas product yield increases and liquid product yield decreases with increasing temperature at similar residence time. A similar trend was observed by Hernández *et al.*[105] for pyrolysis of HDPE in a fluidized bed reactor. At constant reactor temperature, 550 °C, longer residence time increases gas product yield and decreases the liquid product yield. The highest liquid yield of 81.2 wt.% was obtained

at the lowest reactor temperature, 500 °C. Williams *et al.*[98] reported thermal pyrolysis of LDPE in fluidized bed reactor at temperatures between 500 °C to 700 °C. Consistent with this work, they reported an 89.2 wt.% yield of oil and wax products at 500 °C and 15 s residence time.

Table 19. Mass yield of PE4000 pyrolysis products from fluidized bed reactor

Temperature (°C)		500	550	550	550	550	600
Residence time (s)		13.4	12.4	13.9	17.8	20.4	13.7
Product yield (wt.%)	Gas	8.2	18.0	23.4	26.3	27.3	56.8
	Liquid	81.2	73.9	72.7	65.3	64.7	28.5
	Char	<0.1	<0.1	2.1	2.1	2.7	1.8
	Total	89.4	91.9	98.2	93.7	94.7	87.1

Table 20 shows the composition of the gas phase products from pyrolysis of PE4000 in the fluidized bed reactor. The gas products were hydrogen, C2-C4 alkenes, C1-C4 alkanes and 1,3-butadiene. Both the C1-C3 gas and H_2 yields increased with temperature at similar residence times. The concentration of ethylene and propene increased when the temperature increased from 500 to 600 °C. Williams *et al*.[98] also demonstrated the increase in ethylene and propylene concentration as the pyrolysis temperature increases in the pyrolysis of LDPE. It was shown in their study that the increase was even more pronounced as the temperature increased from 650 to 700°C.

Table 20. Gas composition of PE pyrolysis from fluidized bed reactor

Reactor temperature (°C)	500	550	550	550	550	600
Residence time (s)	13.4	12.4	13.9	17.8	20.4	13.7
Carbon Yield (%)						
Methane	0.58	1.94	2.55	3.64	4.13	10.20
Ethene	1.49	5.86	6.84	9.14	9.64	17.74
Ethane	0.93	2.36	3.25	4.07	4.63	9.08
Propene	2.55	4.89	5.94	5.28	4.68	11.50
Propane	0.74	0.78	1.07	0.84	0.71	1.58
Butene	0.85	0.91	0.93	0.51	0.27	0.84
Butane	0.16	0.10	0.10	0.06	0.03	0.11
1,3-Butadiene	0.10	0.29	0.32	0.14	0.07	0.15
Others [a]	0.25	0.25	0.76	0.76	0.88	0.94
Sum	7.66	17.38	21.76	24.44	25.04	52.14
H_2 (vol.%)	27.77	13.04	26.62	25.16	29.07	37.39
Alkene to alkane ratio						
C2	1.6	2.5	2.1	2.2	2.1	2.0
C3	3.4	6.3	5.6	6.3	6.6	7.3
C4	5.3	9.1	9.3	8.5	9.0	7.6

a. The other species include CO and pentane.

The carbon yield of the liquid products for PE4000 pyrolysis at different temperatures and residence times is shown in Figure 21 and Figure 22. The liquid product comprises of a wide range of hydrocarbons with carbon number ranging from C4 to C60. Figure 21 illustrates that, at 500 ^{o}C and residence time of 13.4 s, the distribution is bimodal with local maxima at approximately C6 and C31. As temperature increases to 550 ^{o}C at similar residence time, the second maximum slowly shifts towards lower carbon numbers (C18) and becomes less pronounced, while the low carbon number maximum remains constant around C6. At 600 ^{o}C, the carbon yield only shows one maximum in the C6 region. These results indicate that at lower reaction temperatures two carbon number populations of products form. But, at higher reaction temperatures, the larger products further cleave to generate a unimodal distribution.

The carbon number distribution shifts slightly to lower molecular weight products as the residence time is increased as shown in Figure 22. This shows longer residence time also facilitates the cleavage of longer chain species to shorter pyrolysis products.

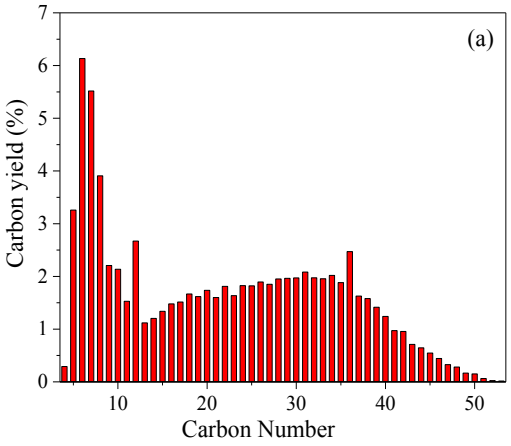
(a)
Carbon yield (%)
Carbon Number
0
1
2
3
4
5
6
7
10
20
30
40
50

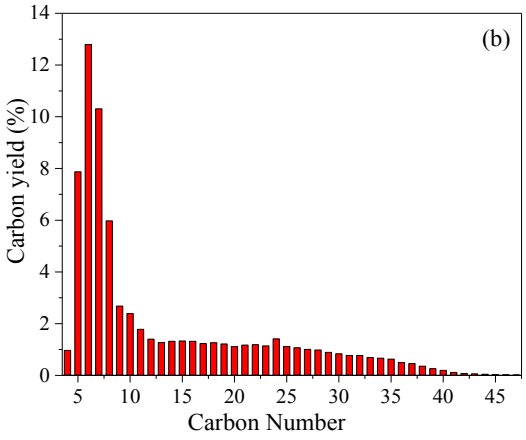
(b)
Carbon yield (%)
Carbon Number
0
2
4
6
8
10
12
14
5
10
15
20
25
30
35
40
45

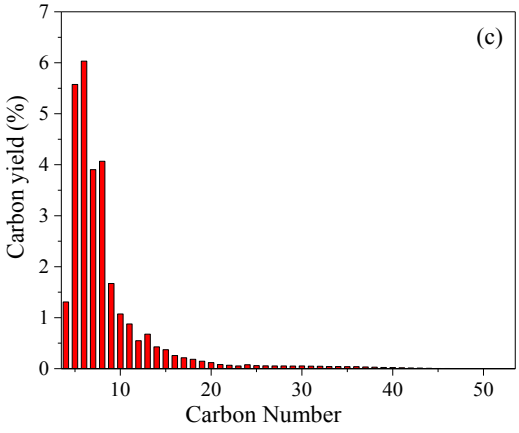
(c)
Carbon yield (%)
Carbon Number
0
1
2
3
4
5
6
7
10
20
30
40
50

Figure 21. Carbon yields of liquid products from PE pyrolysis at (a) 500 ºC, residence time of 13.4 s, (b) 550 ºC, residence time of 13.9 s and (c) 600 ºC, residence time of 13.7s

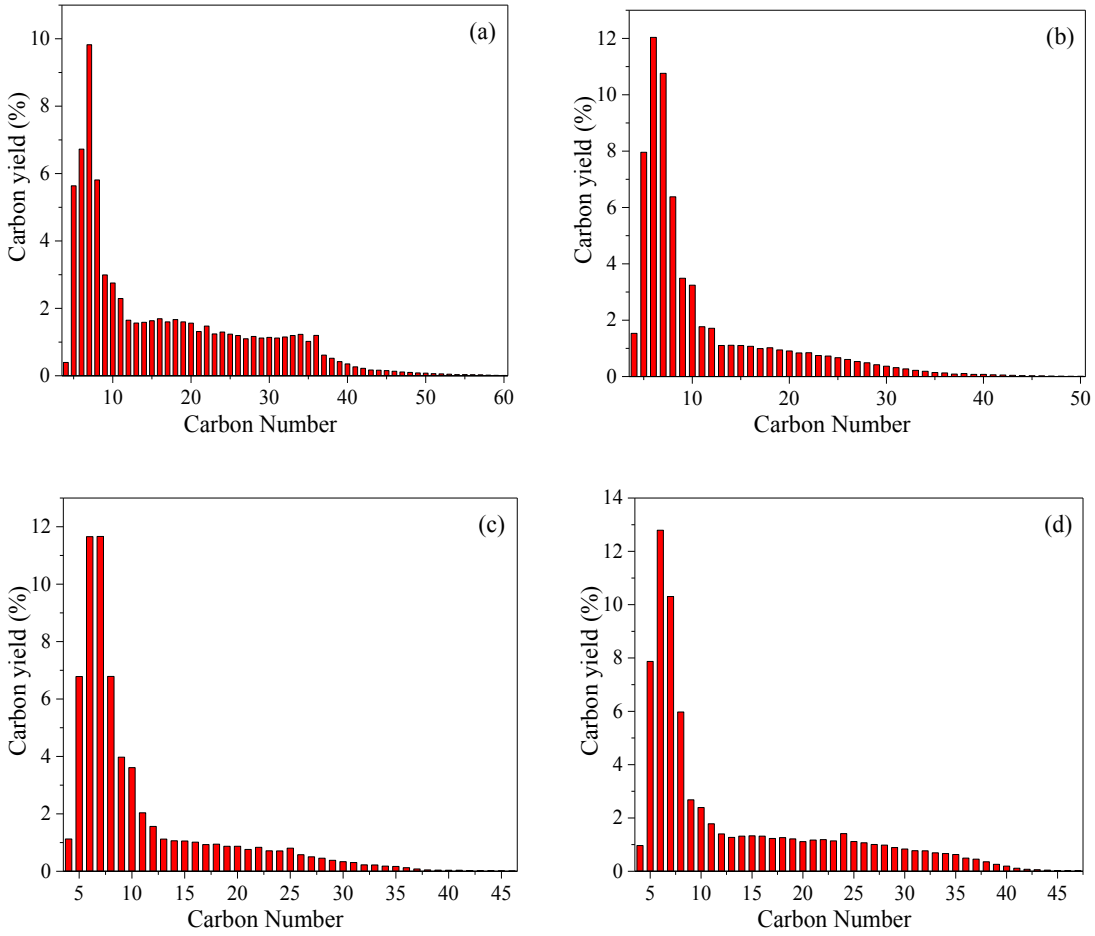

Figure 22. Carbon yields of liquid products at 550 ºC, residence time of (a) 12.4 s, (b) 13.9 s, (c) 17.8 s and (d) 20.4 s

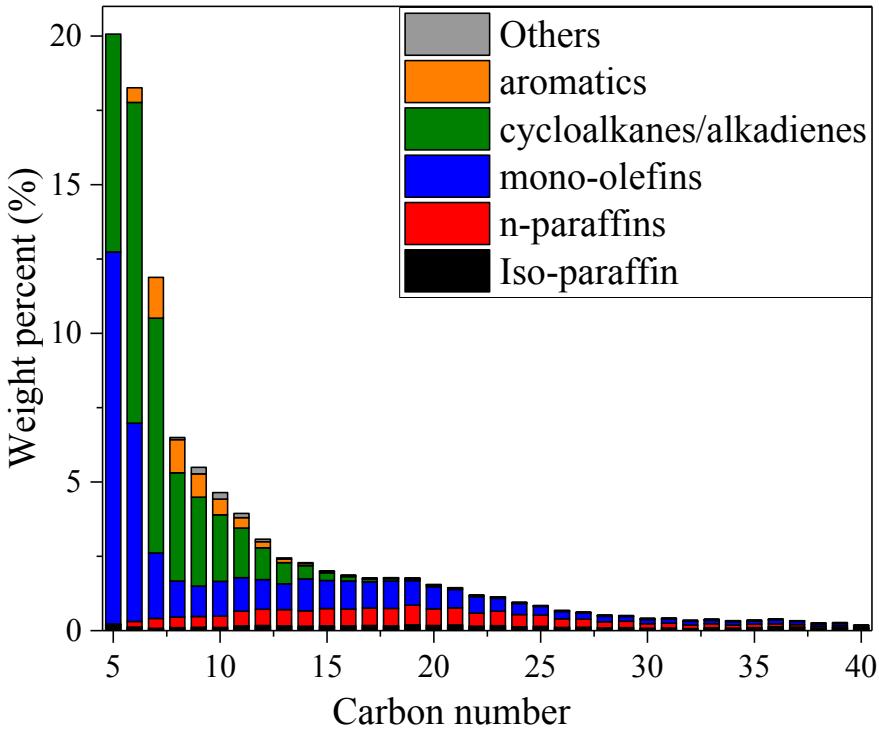

Figure 23. NOISE analysis of liquid product from PE4000 pyrolysis at 550 oC with a residence time of 17.9 s

Figure 23 shows the relative amounts of various chemical functionalities in the liquid product of PE4000 pyrolysis at 550 ^{o}C and residence time of 17.9 s, determined by NOISE analysis. NOISE is a GC-MS-based method that leverages the unique interactions of NO^{+} ions with different hydrocarbon functional groups for identification of the hydrocarbon groups.[106] This additional level of chemical information about the PE pyrolysis oil provides insight into the reaction mechanism and possible product uses. The analysis shows that the liquid product includes n-paraffins, iso-paraffins, mono-olefins, cycloalkanes/alkadiene and aromatics. The cycloalkanes and alkadienes cannot be

distinguished due to overlapping in their standard regions in the NOISE analysis. In the carbon number range of C5 to C13, product abundance decreases in the order of mono-olefin and cycloalkanes/alkadiene > n-paraffin >aromatics > iso-paraffins. In the carbon number range above C14, mono-olefins and paraffins are the most abundant products.

The NOISE liquid product distribution confirms that thermal pyrolysis of PE occurs via thermal degradation mechanism, as proposed by other researchers.[98,107] High-temperature pyrolysis causes 96emolytic chain scission at random positions along the backbone to form hydrocarbon radicals of any carbon number. Free radicals formed by chain scission can react and stabilize through inter- or intramolecular chain transfer, typically by abstraction of a hydrogen atom, either from its own chain or a neighboring molecule, to deliver a saturated product molecule. Polymer radicals can also stabilize by β-scission, which delivers an unsaturated product molecule and a new, smaller terminal free radical that continues in the reaction sequence. This process continues to produce hydrocarbon molecules which are saturated and have either one terminal carbon double bond or a carbon double bond at each end of the molecule.[98] Termination reactions occur when two free radicals combine to form one polymer chain.[108] Therefore, for products of each carbon number, alkenes and the corresponding alkadienes/cycloalkanes are present in large amounts as illustrated in Figure 23.

NOISE analysis also identified a smaller population of aromatic hydrocarbons in the liquid product. The aromatics region in Figure 23 consists only of single-ring aromatics (C_nH_{2n-6}, C_nH_{2n-8}, C_nH_{2n-10}) (Table A1). Neither naphthalene nor PAH was detected in the

liquid product. Formation of aromatic rings has been proposed to occur in secondary Diels-Alder reactions of alkanes and alkenes formed during pyrolytic random chain scission.[109,110]

5.4 Random scission model

5.4.1 Fitting a first-order random scission model to the TGA data

The pyrolysis of a number of polymers can be described by a random scission mechanism,[95,111,112] which assumes a random cleavage of the bonds along the polymer chains, producing fragments of shorter length which evaporate when they become small enough.[93,95,107,113,114] The rate of breakage is first order in the fraction of bonds broken along the initial chain (x) as defined in Eq. 16. In this equation, A is the Arrhenius pre-exponential factor, R is the gas constant, and E is the activation barrier to chain cleavage. In a random cleavage TGA experiment weight loss can expressed according to Eq. 17. α is the normalized mass loss, w_0 is the initial mass of polymer, w_f is the mass of residual char, w is the sample mass at an instant time, β is the heating rate β=dT/dt, N_0 is the initial number of linkages in the polymer chain, and L is the minimum length of the polymer that is not volatile.

$$\frac{dx}{dt} = Aexp(-\frac{E}{RT})(1-x) \qquad \text{(Eq. 16)}$$

$$\alpha = (w_0 - w)/(w_0 - w_f) = 1 - (1 - x)^{L-1}\left[1 + x\frac{(N_0\text{-}L)(L\text{-}1)}{N_0}\right] \qquad \text{(Eq. 17)}$$

Eq. 17 correlates the detected weight loss to the fraction of polymer bonds cleaved. The parameter L is difficult to obtain experimentally. Sánchez-Jiménez *et al.* [115] used a fixed L value and validated the fit between random scission model described by Eq. 17 and TGA data of polybutylene terephthalate (PBT). In this study, a fixed L value of 5 is implemented. Matlab's nlinfit function was used to vary A and E as parameters to fit the weight loss calculated from Eq. 16 and Eq. 17 with experimental TGA data. Figure 24 compares the actual TGA mass loss to the best fit single first-order random scission model, with E = 108.05 ± 1.5 kJ/mol and A = of 1.82×10^5 s^{-1} with 95% confidence interval of [1.38×10^5, 2.38×10^5]. The residuals are plotted in Figure A9. As shown in Figure 24 and Figure A9, the model does not fit the weight loss data well in the temperature ranges of 150-400 ºC and above 500 ºC.

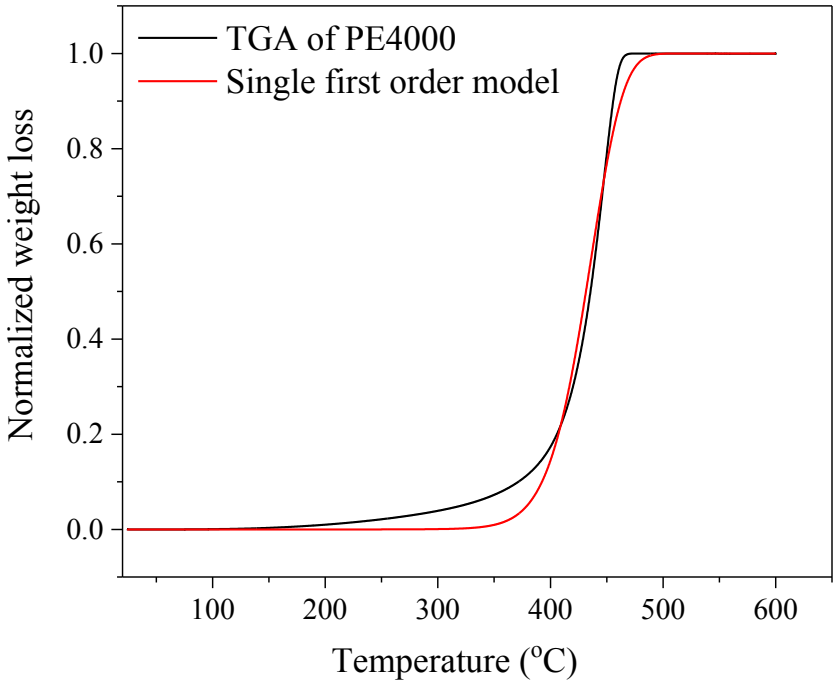

Figure 24. Comparison of weight loss curve of PE4000 and single first order random scission model

Peterson *et al.*[116] reported that the PE degradation kinetics are governed by different processes at the initial and final stages. At low temperatures/conversions, they observed a low activation process, which is likely associated with the cleavage events that occur at the weak links, such as peroxides, chain branches, carbonyls and unsaturated structures. Grassie *et al.*[117] stated that weak links in PE are probably peroxide groups formed during polymer preparation, storage and processing. Once these weak links are consumed, degradation is initiated by random scission at other locations along the chain, with an

activation energy of 240 kJ/mol. Therefore, we fit a parallel, two-step random scission model to our TGA results shown in Eq. 18and 19.

$$\frac{dx}{dt} = [A_1 exp(-\frac{E_1}{RT}) + A_2 exp(-\frac{E_2}{RT})](1-x) \quad \text{(Eq. 18)}$$

$$\alpha = 1-(1-x)^{L-1}\left[1 + x\frac{(N-L)(L-1)}{N}\right] \quad \text{(Eq. 19)}$$

Figure 25 compares the weight loss predicted by the model with two first-order reactions and that from TGA experiment. The parameters obtained from the fitting are A_1=3.0×10^{-3} s^{-1} (95% confidence interval: [2.9×10^{-3}, 3.2×10^{-3}]), E_1=16.5 ± 0.2 kJ/mol, A_2 = 4.0 ×10^{14} s^{-1} (95% confidence interval: [3.3×10^{14}, 4.9×10^{14}]), E_2=234.8 ± 4.0 kJ/mol. The combination of two parallel first order random scission model fits the TGA profile of PE4000 well across all temperatures with maximum absolute residual of 0.021 (Figure A10).

A similar approach was adopted to fit a model with two first order reactions to the TGA profile of PE35000. The values of A's (A_1=3.0×10^{-3}, A_2 = 4.0 ×10^{14} s^{-1}) were kept the same as PE4000 and the two activation energies were varied as parameters to minimize the weighted least squares. Activation energies of E_1=17.1 ± 0.02 kJ/mol and E_2=240.9 ±

0.03 kJ/mol were obtained. The fit of the model to the TGA of PE35000 and the residual of fit are shown in Figure A11 and Figure A12. The combination of two parallel first order random scission model also fits the TGA profile of PE35000 relatively well across all temperatures with maximum absolute residual of 0.027 (Figure A12) with similar activation energies for the two parallel first order reactions to those of PE4000. These results show that the random scission decomposition kinetics of PE are not strong functions of molecule size.

We used Akaike Information Criterion (AIC) to compare both models for the TGA of PE4000.[118-123] AIC estimates the quality of each model and provides a means for model selection. The AIC value is given in Eq. 20,[124] where k is the number of estimated parameters, n is the number of data points and RSS is the residual sum of squares. AIC evaluates the goodness of fit (assessed by the likelihood function) and includes a penalty for overfitting. A lower AIC value indicates a more preferred model in a given set of candidate models.

$$AIC = n\,ln(RSS/n) + 2k \qquad \text{(Eq. 20)}$$

AIC values of -2.46×10^4 and -3.82×10^4 were obtained for the single first-order model and two parallel first-order model, respectively. Hence, the random scission model with two parallel first-order reactions fits the TGA profile better.

Figure 26 compares the rate constants k_1 and k_2. At temperatures lower than 356 ^oC, k_2 is more than 10 times lower than k_1. With the increase of temperature, k_2/k_1 increases. When the temperature is above 393 ^oC, k_2 becomes larger than k_1. Peterson *et al.*[116] proposed that at the initial stage, degradation reaction occurs via breaking of weak links. This process has a lower activation energy compared to the later process. As weak links are consumed, the degradation shifts towards a random scission mechanism with an activation energy of about 240 kJ/mol.[116] Although the estimated pre-exponential factor for the first step is small, its estimation may be affected by other factors such as surface area which is not directly affected by the reaction mechanism.[125] For this reason the activation energies were the primary factors for the discussion of degradation mechanisms.[117,126-129] Table A2 shows the change of fitted parameters with L value. The lower activation energy changes with L whereas the higher activation energy that corresponds to the true random scission of polymer chain varies little with L.

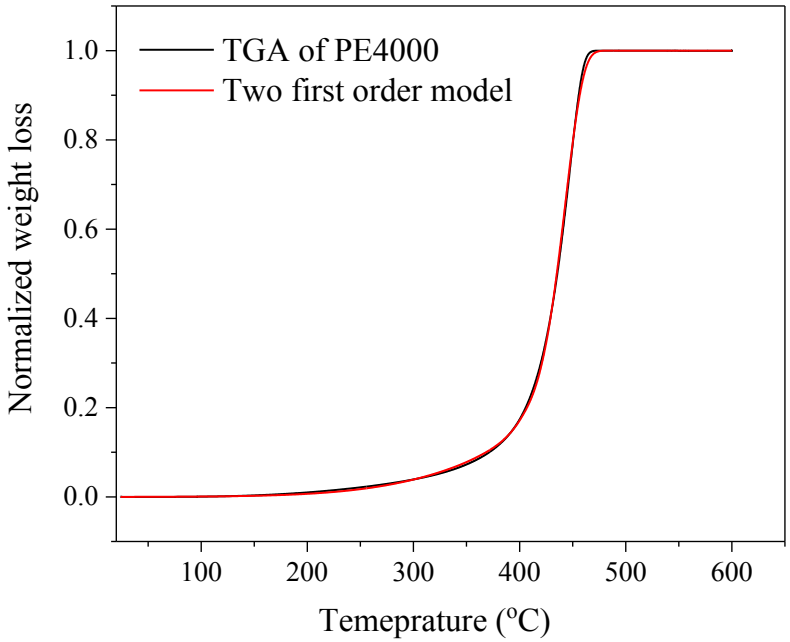

Figure 25. Comparison of weight loss curve of PE4000 and two first order random scission model

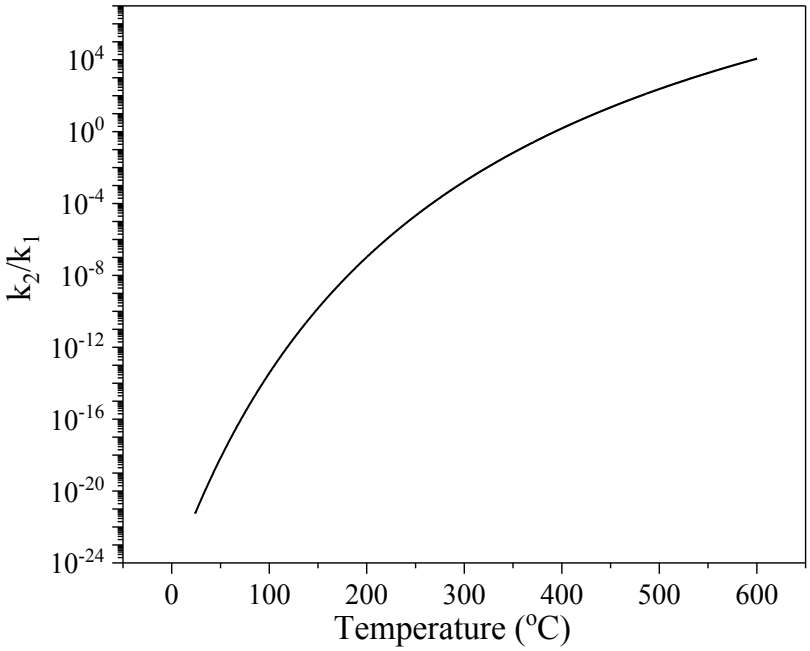

Figure 26. Ratio of k_2/k_1 as a function of temperature

5.4.2 Comparison of the product carbon distribution from the model and pyrolysis of PE4000 in the fluidized bed reactor

The weight fraction of a chain fragment in a random scission mechanism can be expressed in Eq. 21,[130,131] where n is the number of monomers in the chain fragment, w_n is the weight fraction of a chain fragment, and x is the fraction of bonds broken. x and N correlate via $x= (1- N/N_o)$, where N is the number of linkages. The random scission model with two parallel first-order reactions with parameters estimated from the TGA experiments (A_1=3.0×10^{-3} s^{-1}, E_1=16.5 kJ/mol, A_2 = 4.0 ×10^{14} s^{-1}, E_2=234.8 kJ/mol) was used to model the liquid product distribution in the fluidized bed reactor. Reaction time t was varied as parameter in the model to fit the product weight distribution to that from the pyrolysis in the fluidized bed. Figure 27 and Figure 28 show the fit between product weight distribution from pyrolysis of PE in the fluidized bed reactor (shown previously in Figure 21 and Figure 22) and from the model.

$$w_n = nx^2(1-x)^{n-1} \qquad \text{(Eq. 21)}$$

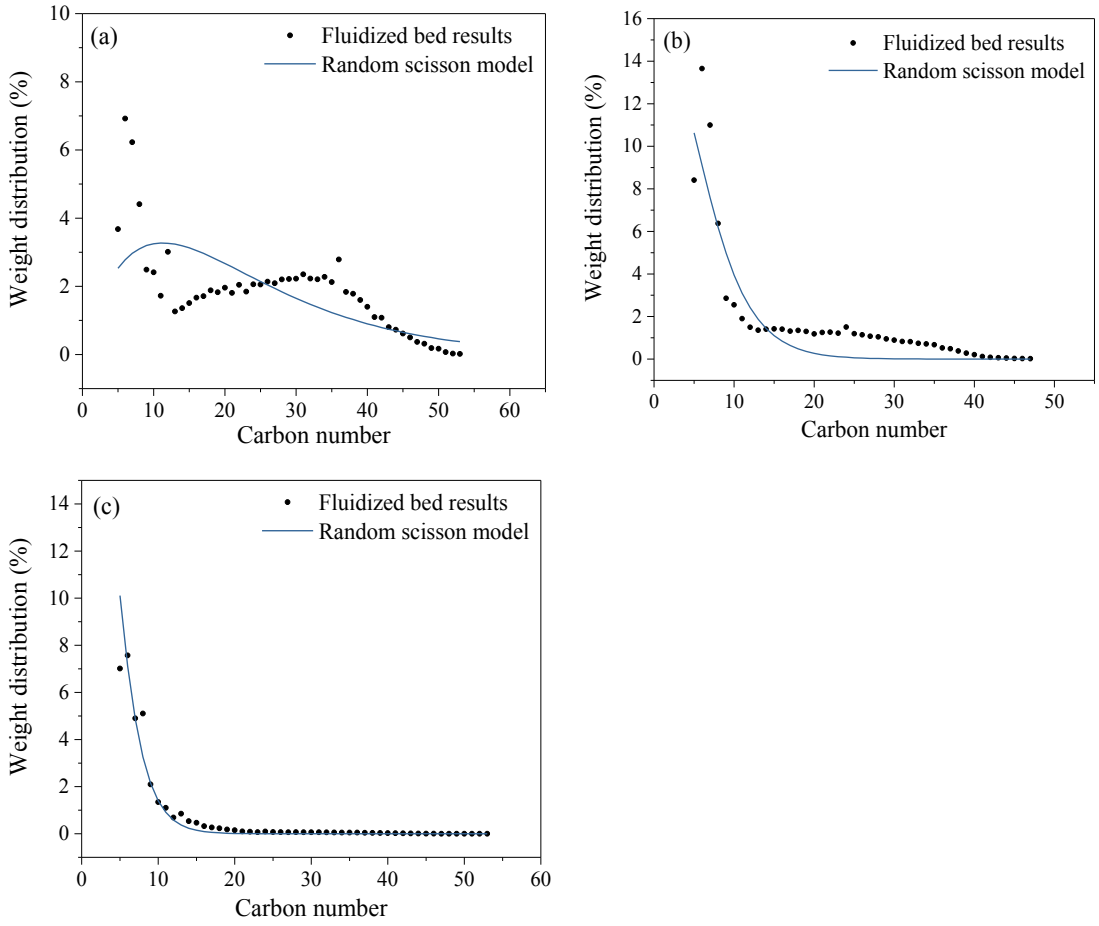

Figure 27. Product weight distribution from pyrolysis of PE4000 in the fluidized bed and random scission model at (a) 500°C, 13.4 s, (b) 550°C, 13.9 s, (c) 600°C, 13.7 s

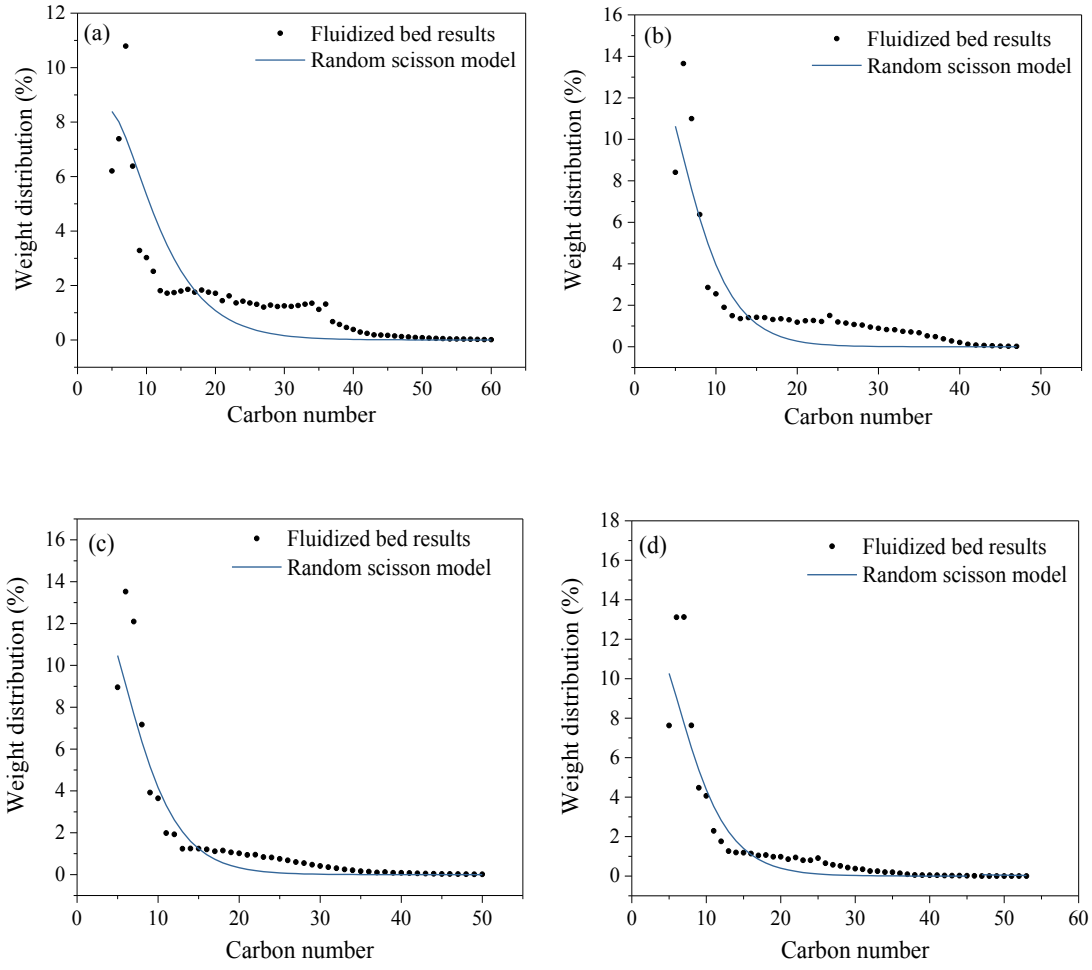

Figure 28. Product weight distribution from pyrolysis of PE4000 in the fluidized bed and random scission model at 550°C residence time of (a) 12.4 s, (b) 13.9 s, (c) 17.8 s, (d) 20.4 s

Figure 27 and Figure 28 show that the carbon number distributions, expected of pure random-scission, either decrease monotonically with carbon number (high conversions) or display a single maximum (low conversions). They do not have the bimodal distributions observed in many of the fluidized bed experiments. These differences likely reflect secondary, non-random reactions of the random scission radical fragments. For example, Yoichi *et al*. [94] proposed two non-random reaction paths that may occur during polymer pyrolysis: 1) chain-end scission by a back-biting reaction, where the chain-end radical sustains intramolecular hydrogen-abstraction via a cyclic transition state that can eliminate dimer or trimer products, with or without double bonds and 2) fragmentation of the chain-end radical to give a monomer via β-scission. [94,132,133] Both of these non-random routes would preferentially deliver C2, C3 and C6 fragments, and could, therefore, account for the low carbon number maxima in the experimental bimodal distributions.

5.5 Product potential

The aim of plastic pyrolysis is to valorize plastic wastes to produce fuels and chemicals. Mixed plastic waste pyrolysis using a fluidized bed reactor has been previously demonstrated in pilot scale by BP Chemicals, UK.[134] The pilot plant is a 50 kg h^{-1} plant and the derived products have been fed to conventional steam cracker and fluidized catalytic cracker petroleum processing units. The wax produced was mixed with the naphtha fraction of petroleum oil at inputs of up to 20 wt.%. The mixture was then fed to

a conventional steam cracker without significantly altering the existing process to produce ethylene and other alkenes which can be used to make new plastic polymers.[98] The oil/wax products from the BP Chemicals plastics pyrolysis plant were also demonstrated to recover gasoline and LPG after refined in the catalytic cracking processes.

The oil/wax products from the pyrolysis of PE in this work mainly consists of paraffins, olefins and cycloalkanes/aladinenes in the carbon range of C5–C40. The oil/wax products could thus be considered as a mixture of heavy naphtha (C7–C10), gasoline (C8–C10), light gas oil (C10–C22) and higher boiling point hydrocarbons (>C24).[135,136] Gasoline range hydrocarbons can be separated from the pyrolysis oil by fractional distillation.[135] More valuable chemicals, including benzene, toluene and other aromatic hydrocarbons could be obtained by refining the pyrolysis oil. Joo *et al.*[137] reported about 50 wt.% gasoline yield from mixed plastic pyrolysis by a three-step sequential process consisting of hydrotreating, hydrocracking and distillation. The gasoline product from their study was characterized by higher paraffins, lower aromatics and comparable research octane number compared to a mid-grade commercial gasoline, indicating a potentially more favorable gasoline from an environmental viewpoint.

In addition to oil/wax products, we also observed a significantly higher gas product yield with higher temperatures or longer residence times. Particularly, a high concentration of C2–C4 olefins is present in the gas products. These light olefins are important building blocks for the synthesis of fuels, lubricants and chemicals.[2] Reaction

conditions can be optimized to maximize the gas yield such as higher temperatures or longer residence times. Simon *et al*.[138] have also reported high yield of short olefins from pyrolysis of polyolefins with steam at 700ºC (20–31 wt.% ethylene, 14–18 wt.% propylene, 3–6 wt.% butene with additional 19–23 wt.% pyrolysis gasoline). Heterogeneous acid catalysts are able to oligomerize light olefins to branched oligomers as fuels additives.[139] Due to the current moderate oil prices, plastic waste pyrolysis technology is more likely to be economically competitive to produce higher value products such as lubricants and chemicals.[136] Homogeneous catalysts[140,141] and non-acidic heterogeneous catalysts[35,37,142] can oligomerize these light olefins to form higher carbon number linear olefins. C4–C8 linear alpha olefins are used as co-monomers in the production of polyethylene. C10–C14 linear alpha olefins are used to make detergent and plasticizer alcohols. C16–C18 alpha or internal olefins are used to produce oil filed chemicals, lubricant oil additives and surfactants. [2]

5.6 Conclusions

The intrinsic kinetics of PE pyrolysis were measured in TGA. The kinetic data was fitted to a kinetic model that consisted of two first-order random scission reactions where the first reaction had an apparent activation energy of 16.5 kJ/mol and the second reaction had an apparent activation energy of 234.8 kJ/mol. Pyrolysis of PE was studied in a fluidized bed reactor at temperatures ranging from 500 - 600 ^{o}C and residence times of 12.4 – 20.4 s. The gas products yield increased from 8.2 wt.% to 56.8 wt.% and the liquid products yield decreased from 81.2 wt.% to 28.5 wt.% as the temperature increased from 500^{o}C to 600^{o}C. The gas products include hydrogen, C1–C4 paraffins, C2–C4 olefins and 1,3-butadiene. The liquid products include n-paraffins, iso-paraffins, mono-olefins, cycloalkanes/alkadiene and aromatics. At lower carbon numbers, mono-olefins, paraffins and cycloalkanes/alkadiene are the most abundant products. With the increase of carbon number, mono-olefins and paraffins became the dominant products. The liquid products had a bimodal product distribution at lower temperatures or shorter residence times. The random scission model correlates to the overall product distribution trend and matches the product distribution better at longer residence times or higher temperatures. The scission model does not describe the bimodality generated from non-random scission mechanism at lower temperatures or shorter residence times. The gas and liquid products can be recycled into the petrochemical industry as feedstock to produce fuels and chemicals.

Chapter 6. Summary and Future Work (II)

6.1 Summary of PE pyrolysis study

A combination of experimental and modeling approach was used to study the pyrolysis of PE. The kinetic data from TGA were fitted to a kinetic model that consisted of two first-order random scission reactions. Pyrolysis of PE was studied in a fluidized bed reactor at temperatures ranging from 500 – 600 ^{o}C and residence times of 12.4 – 20.4 s. The gas products yield increased and the liquid products yield decreased as the temperature increased from 500^{o}C to 600^{o}C. The gas products include hydrogen, C1–C4 paraffins, C2–C4 olefins and 1,3-butadiene. The liquid products include n-paraffins, iso-paraffins, mono-olefins, cycloalkanes/alkadiene and aromatics. The liquid products had a bimodal product distribution at lower temperatures or shorter residence times. This study provides a framework for assessing pyrolysis-based approaches for converting polyethylene to valuable fuels and chemicals. The approach could be applied in studying the pyrolysis of other plastic wastes.

6.2 proposed future work for PE pyrolysis

Chapter 5 presents the results of PE thermal pyrolysis and introduced the products' potential to be recycled into the petrochemical industry as feedstock to produce fuels and chemicals. Among the product species, linear alpha olefins are of the highest market value. Linear alpha olefins are important building blocks for the synthesis of fuels, lubricants and chemicals.[2] Future work could focus on optimizing reaction conditions to maximize the olefin yield. For example, Simon *et al.*[138] have reported a high yield of short olefins from pyrolysis of polyolefins with steam at 700°C (20–31 wt.% ethylene, 14–18 wt.% propylene, 3–6 wt.% butene with additional 19–23 wt.% pyrolysis gasoline). Future work in process synthesis of plastic pyrolysis with light olefin oligomerization to produce high-value linear oligomers from plastic waste is also a promising direction.

Although conventional thermal pyrolysis converts plastic waste into liquid oil, gas and solid residue, the process is temperature dependent.[143,144] The liquid oil from thermal pyrolysis may contain residue and impurities. Moreover, the thermal pyrolysis of HDPE, LDPE and polypropylene (PP) is difficult to achieve desirable yield due to their cross chain hydrocarbon structures.[145] Therefore, catalytic pyrolysis could be investigated in the future to overcome these problems of thermal pyrolysis.

A range of catalysts have been investigated by other researchers including Red Mud, FCC, ZSM-5, HZSM-5, Y-zeolite, Fe_2O_3 , Al_2O_3, $Ca(OH)_2$ and natural zeolites. The use of catalysts can increase the quality of the pyrolysis liquid oil. ZSM-5 decreased the

nitrogen, phosphorous and sulfur contents in the liquid oil according to the study by Miskolczi *et al.* [146] Catalytic pyrolysis of HDPE and PP were studied in a continuous reactors and it was found that degradation of pollutants occurs in small internal pores of ZSM-5. Whyte *el al.* [147] found that the use of ZSM-5 reduced the amount of tar produced and achieved higher deoxygenation and organic liquid yield during pyrolysis of refuse-derived fuel (RDF). Miskolczi *et al.*[148] investigated catalytic pyrolysis of real municipal plastic waste (MPW). It was found that β-zeolite and MoO_3 are able to reduce the viscosity of pyrolysis oil from real municipal plastic waste (MPW), while Ni-Mo catalysts can modify the morphology of the chars.

Researchers have also found that use of catalysts gives similar product yield in plastic waste pyrolysis at lower temperatures and retention times compared to thermal pyrolysis.[144,149,150] The overall process is thus more economically feasible. For instance, an increase in cracking rate at lower temperature was observed by Lee *et al*. with HZSM-5 and HY zeolites.[151] Zeolite catalysts are efficient for C–C cracking reaction due to its high pore surface area that leads to acceleration in the thermal degradation of plastic polymers.[85]

APPENDIX

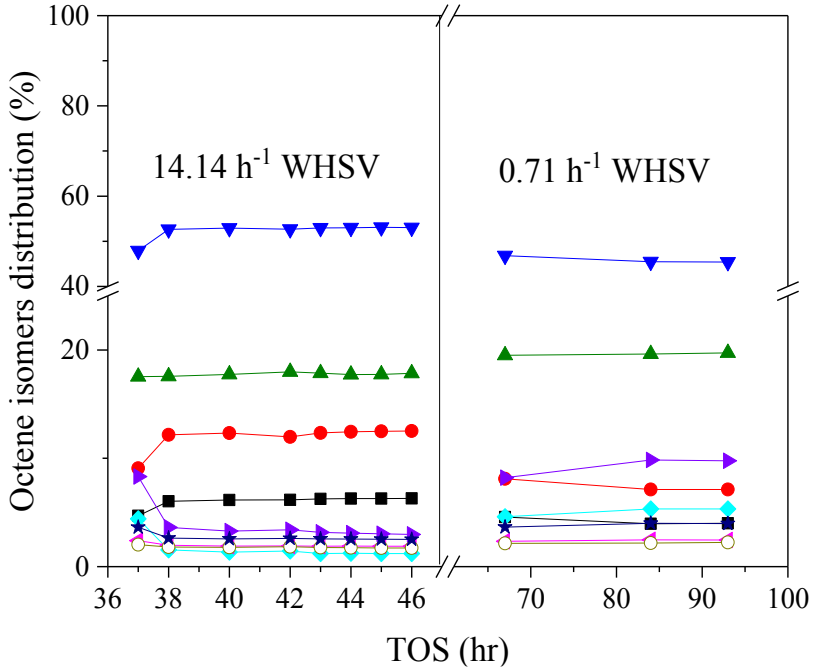

Figure A1. Octene isomers distribution with time on stream over 2A-CoOx/N-C-230, including: (▼) *trans*-3-octene, (▲) *trans*-2-octene, (●) *cis*-2-octene, (■) *cis*-5-methyl-2-heptene, (►) 3-methyl-2-heptene, (◆) *trans*-4-octene, (◄) *trans*-5-methyl-3-heptene, (○) *cis*-5-methyl-3-heptene and (★) *trans*-5-methyl-2-heptene at 80 ºC and 450 psig

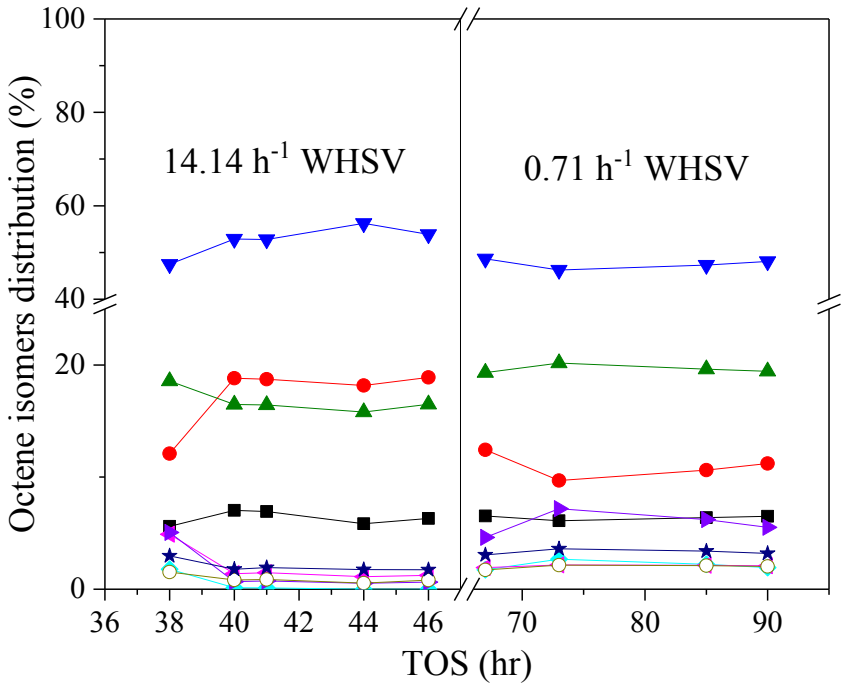

Figure A2. Octene isomers distribution with time on stream over 2NaOH-CoOx/N-C-230, including: (▼) *trans*-3-octene, (▲) *trans*-2-octene, (●) *cis*-2-octene, (■) *cis*-5-methyl-2-heptene, (►) 3-methyl-2-heptene, (◆) *trans*-4-octene, (◄) *trans*-5-methyl-3-heptene, (○) *cis*-5-methyl-3-heptene and (★) *trans*-5-methyl-2-heptene at 80 ^{o}C and 450 psig

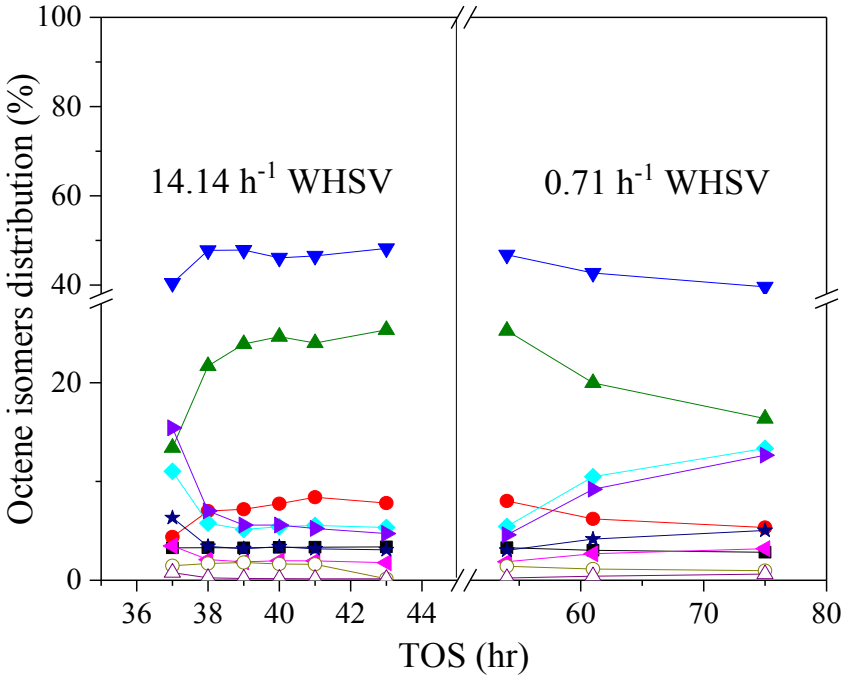

Figure A3. Octene isomers distribution with time on stream over 2A-CoOx/N-C-350, including: (▼) *trans*-3-octene, (▲) *trans*-2-octene, (●) *cis*-2-octene, (■) *cis*-5-methyl-2-heptene, (►) 3-methyl-2-heptene, (◆) *trans*-4-octene, (◄) *trans*-5-methyl-3-heptene, (○) *cis*-5-methyl-3-heptene and (★) *trans*-5-methyl-2-heptene at 80 ºC and 450 psig

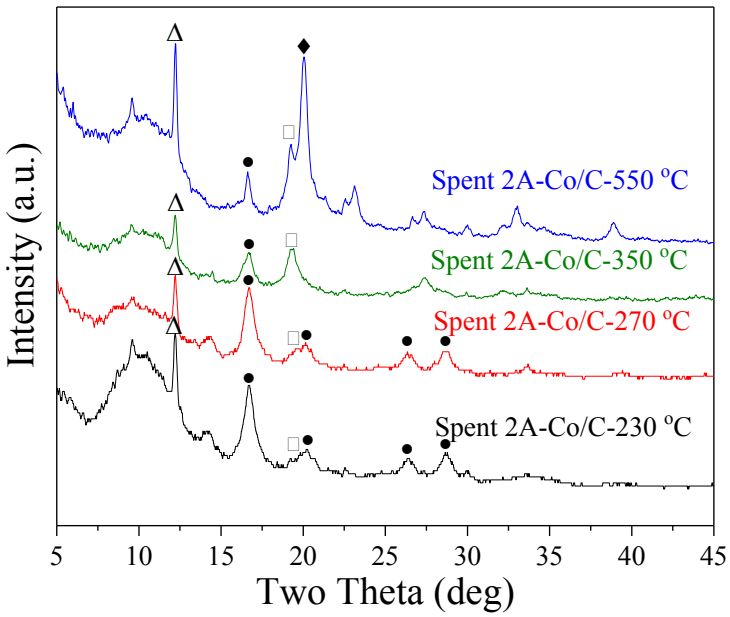

Figure A4. Mo-XRD patterns of the spent catalysts, with characteristic peaks of ▵graphite, ●Co_3O_4, □CoO, ◆Cubic Co

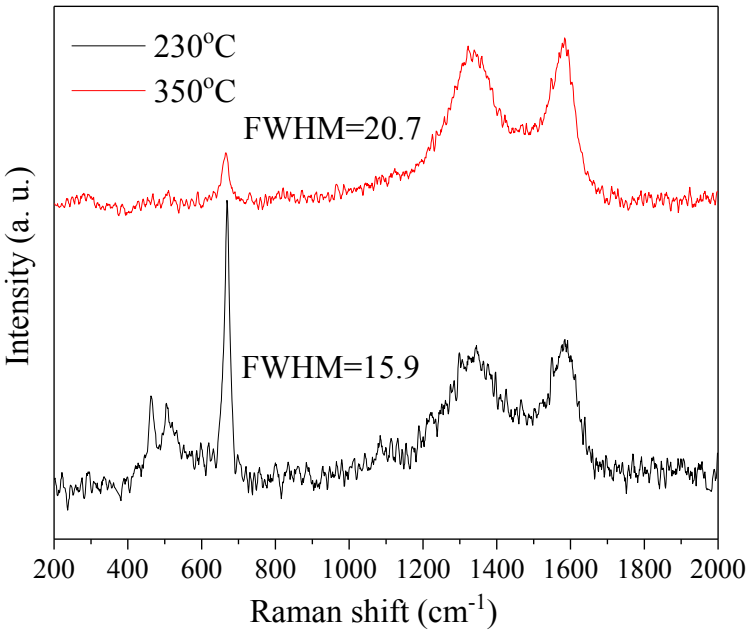

Figure A5. Comparison of CoOx signal at 690 cm^{-1} during pretreatment at 230 °C and 350 °C

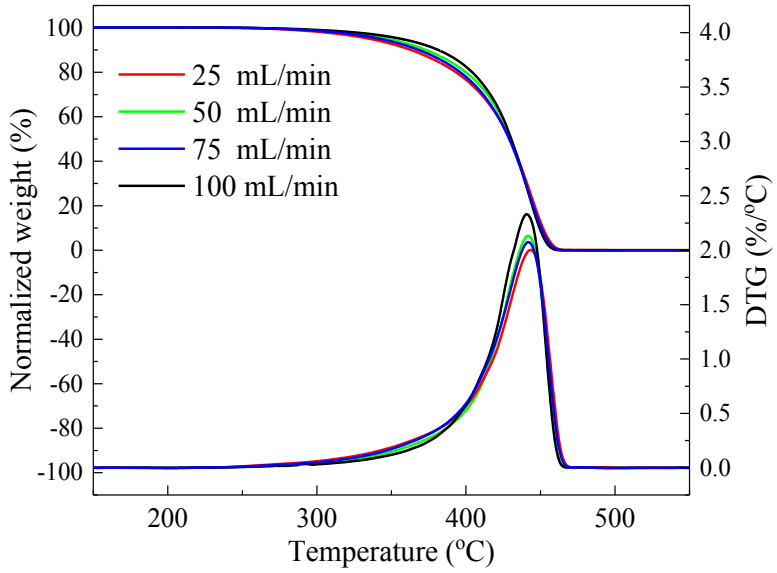

Figure A6. Thermal decomposition of PE35000 at different nitrogen flow rate (particle size: 180-250µm, initial mass: 10mg, heating rate: 10 °C/min)

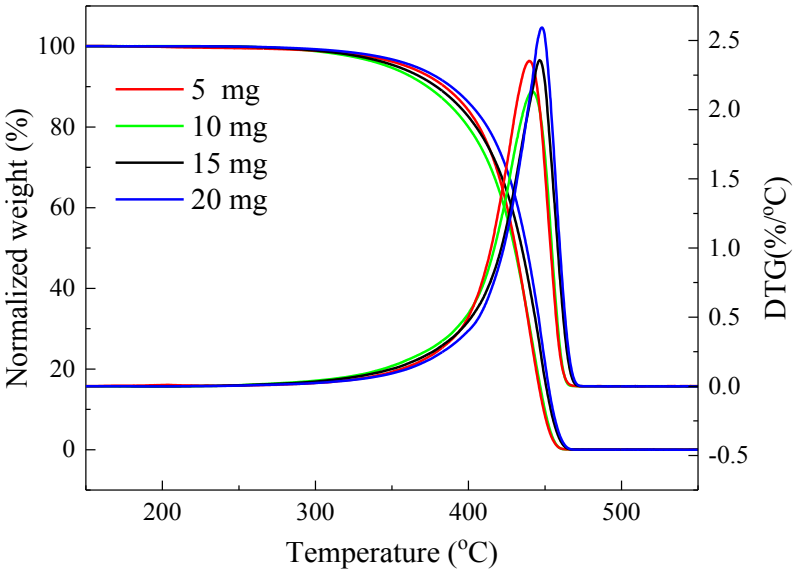

Figure A7. Thermal decomposition of PE35000 at different sample masses (particle size: 180-250µm, sweep gas flowrate: 50mL/min, heating rate: 10 °C/min.)

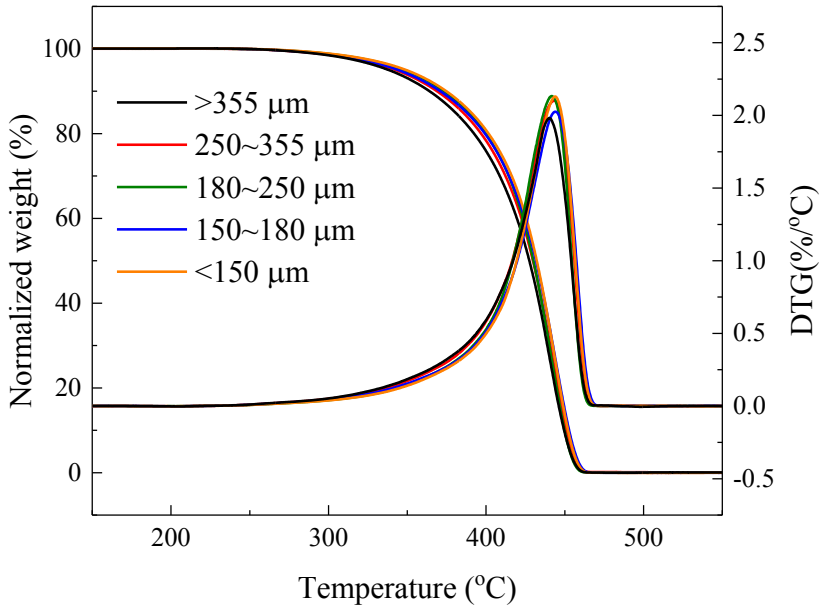

Figure A8. Thermal decomposition of PE35000 at different particle sizes (initial mass: 10mg, sweep gas flowrate: 50mL/min, heating rate: 10 °C/min)

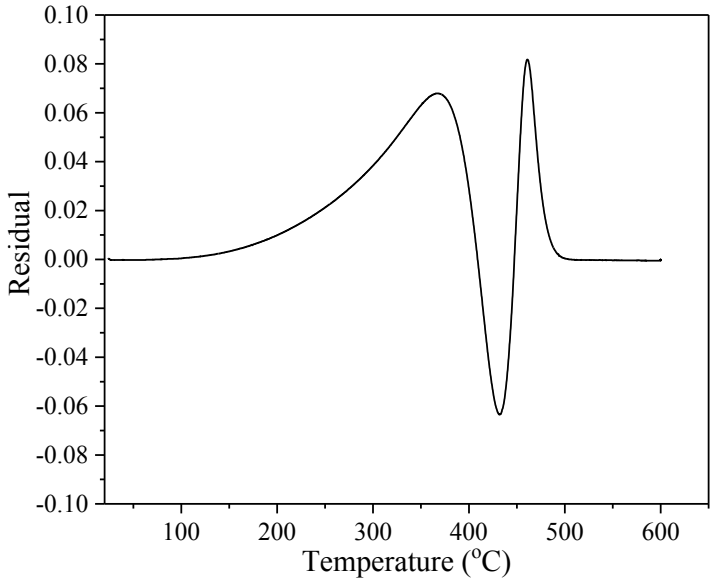

Figure A9. Residual of fit as a function of temperature for a single first order random scission model for TGA of PE4000

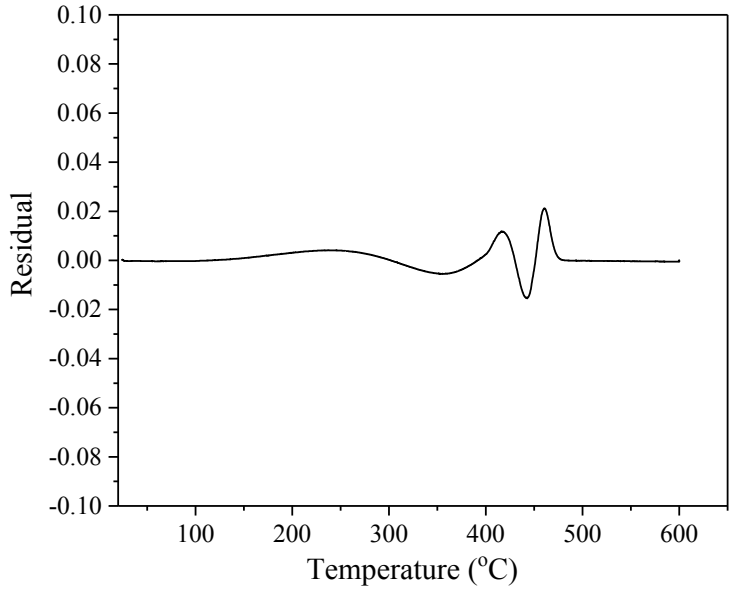

Figure A10. Residual of fit as a function of temperature for a random scission model with two parallel first order reactions for TGA of PE4000

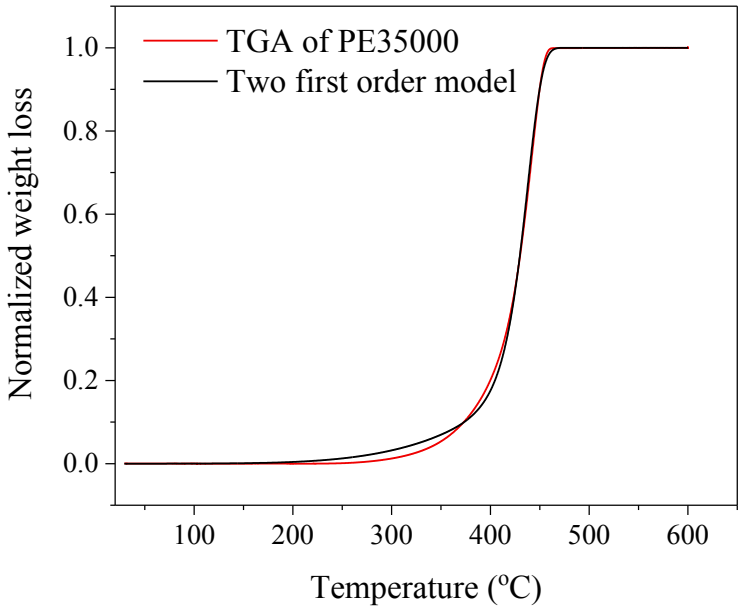

Figure A11. Comparison of weight loss curve of PE35000 and two first order random scission model

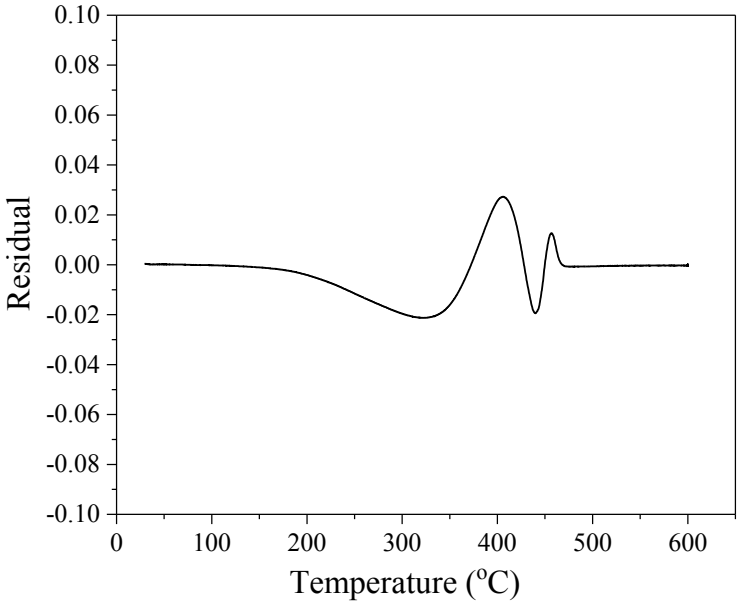

Figure A12. Residual of fit as a function of temperature for a random scission model with two parallel first order reactions for TGA of PE35000

Table A1. Z number summary from NOISE analysis

Z number	Weight percent (%)	Assignment	Weight percent (%)
+2 Iso	4.65	Total Paraffins:	16.32
+2 Normal	11.67		
+0 Olefins	38.35	Mono-olefins:	38.35
+0	32.16	Cycloalkanes	39.97
-2	7.56		
-4	0.25		
-6	4.47	Monoaromatics:	5.37
-8	0.78		
-10	0.12		
-12	ND [a]	Diaromatics:	0.00
-14	ND		
-16	ND		
-18	ND	Triaromatics:	0.00
-20	ND		
-22	ND		
-24	ND	Tetraaromatics:	0.00
-26	ND		
-28	ND		
-30	ND	Pentaaromatics:	0.00
-32	ND		
-34	<0.01		
		Total	100.00

a. ND: not detected.

Table A2. Fitted parameters for different L values

L	E_1 (kJ/mol)	A_1	E_2 (kJ/mol)	A_2
3	15.9	4.9×10^{-3}	241.9	2.5×10^{15}
5	16.5	3.0×10^{-3}	234.8	4.0×10^{14}
8	18.2	2.6×10^{-3}	242.8	9.2×10^{14}
10	19.2	2.4×10^{-3}	243.6	8.4×10^{14}
13	20.3	2.3×10^{-3}	239.8	3.3×10^{14}
15	21.1	2.3×10^{-3}	241.3	3.7×10^{14}

NOTATION

200A-CoOx/N-C: cobalt oxide on 200A-N-C catalyst

200A-N-C: nitrogen-doped carbon synthesized at 200^{o}C with NH_3

2A-CoOx/N-C: doubly ammoniated cobalt oxide on carbon catalyst

2D-GC-MS: two-dimensional gas chromatograph-mass spectrometer

400A-CoOx/N-C: cobalt oxide on 400A-N-C catalyst

400A-N-C: nitrogen -doped carbon synthesized at 400^{o}C with NH_3

600A-CoOx/N-C: cobalt oxide on 600A-N-C catalyst

600A-N-C: nitrogen -doped carbon synthesized at 600^{o}C with NH_3

800A-CoOx/N-C: cobalt oxide on 800A-N-C catalyst

800A-N-C: nitrogen -doped carbon synthesized at 800^{o}C with NH_3

AC: ammonium hydroxide treated carbon

AIC: Akaike Information Criterion

APS: Advanced photon source

AWC: nitric acid washed carbon

BET: Brunauer-Emmett-Teller

CCVD: catalytic chemical vapor deposition

DFT: density functional theory

DTG: derivative thermogravimetric

E_a: activation energy

EXAFS: Extended X-ray absorption fine structure

FID: flame ionization detector

FWHM: full width half-maximum

HDPE: high density polyethylene

HRTEM: High-resolution transmission electron microscopy

I.D.: inner diameter

ICP-AES: Inductively Coupled Plasma Atomic Emission Spectrometry

LAO: Linear alpha olefin

LCF: linear combination fit

LDPE: low density polyethylene

MAO: methylaluminoxane

Mt: million metric ton

NCB: number of chain branches

NDIR: nondispersive infrared

NEXAFS: Near Edge X-Ray Absorption Fine Structure

NOISE: Nitric oxide ionization spectroscopy evaluation

O.D.: outer diameter

OER: oxygen evolution reaction

ORR: oxygen reduction reaction

PE: polyethylene

sccm: standard cubic centimeter per minute

TEM: transmission electron microscopy

TGA: Thermogravimetric analysis

TOC: total organic carbon

TOF: turn over frequency

TOS: time on stream

WHSV: weight hourly space velocity

XANES: X-ray absorption near edge structure

XAS: X-ray Adsorption Spectroscopy

XPS: X-ray photoelectron spectroscopy

XRD: X-ray diffraction

BIBLIOGRAPHY

(1) U.S. Energy Information Administration Homepage. https://www.eia.gov. (accessed Sep 16, 2017).

(2) Greiner, E. O. C.; Blagoev, M.; Yamaguchi, Y. *Linear alpha-Olefins*, 2013.

(3) Schmidt, R.; Griesbaum, K.; Behr, A.; Biedenkapp, D.; Voges, H.-W.; Garbe, D.; Paetz, C.; Collin, G.; Mayer, D.; Höke, H. *Hydrocarbons*, 2014.

(4) Belov, G. P.; Matkovsky, P. E. *Petroleum Chemistry* **2010**, *50*, 283.

(5) Franken, J.; Kirschhock, C. E. A.; Mathys, G. M.; Martens, J. A. *Chemcatchem* **2012**, *4*, 1245.

(6) Chen, C. S. H.; Bridger, R. F. *Journal of Catalysis* **1996**, *161*, 687.

(7) Beltrame, P.; Forni, L.; Talamini, A.; Zuretti, G. *Applied Catalysis A: General* **1994**, *110*, 39.

(8) Sharuddin, S. D. A.; Abnisa, F.; Daud, W. M. A. W.; Aroua, M. K. *Energ Convers Manage* **2016**, *115*, 308.

(9) Jambeck, J. R.; Geyer, R.; Wilcox, C.; Siegler, T. R.; Perryman, M.; Andrady, A.; Narayan, R.; Law, K. L. *Science* **2015**, *347*, 768.

(10) Geyer, R.; Jambeck, J. R.; Law, K. L. *Science advances* **2017**, *3*, 1700782.

(11) *Pipeline & Gas Journal* **2013**, *240*.

(12) Bollmann, A.; Blann, K.; Dixon, J. T.; Hess, F. M.; Killian, E.; Maumela, H.; McGuinness, D. S.; Morgan, D. H.; Neveling, A.; Otto, S. *Journal of the American Chemical Society* **2004**, *126*, 14712.

(13) Keim, W. *Angewandte Chemie International Edition* **2013**, *52*, 12492.

(14) Sinn, H.; Kaminsky, W. *Advances in Organometallic Chemistry* **1980**, *18*, 99.

(15) Broene, R. D.; Brookhart, M.; Lamanna, W. M.; Volpe, A. F. *Journal of the American Chemical Society* **2005**, *127*, 17194.

(16) Small, B. L.; Brookhart, M. *Journal of the American Chemical Society* **1998**, *120*, 7143.

(17) Zhang, J.; Yan, Y.; Chu, Q.; Feng, J. *Fuel Processing Technology* **2015**, *135*, 2.

(18) Kim, Y. T.; Chada, J. P.; Xu, Z. R.; Pagan-Torres, Y. J.; Rosenfeld, D. C.; Winniford, W. L.; Schmidt, E.; Huber, G. W. *Journal of Catalysis* **2015**, *323*, 33.

(19) Bjørgen, M.; Lillerud, K.-P.; Olsbye, U.; Bordiga, S.; Zecchina, A. *The Journal of Physical Chemistry B* **2004**, *108*, 7862.

(20) Quann, R. J.; Green, L. A.; Tabak, S. A.; Krambeck, F. J. *Industrial & engineering chemistry research* **1988**, *27*, 565.

(21) Knifton, J. F.; Sanderson, J. R.; Dai, P. E. *Catalysis letters* **1994**, *28*, 223.

(22) Chauvin, Y.; Commereuc, D.; Hugues, F.; Thivolle-Cazat, J. *Applied catalysis* **1988**, *42*, 205.

(23) Shabaker, J. W.; Davda, R. R.; Huber, G. W.; Cortright, R. D.; Dumesic, J. A. *Journal of Catalysis* **2003**, *215*, 344.

(24) Schultz, R. G.; Schuck, J. M.; Wildi, B. S. *Journal of Catalysis* **1966**, *6*, 385.

(25) Schultz, R. G.; Engelbrecht, R. M.; Moore, R. N.; Wolford, L. T. *Journal of Catalysis* **1966**, *6*, 419.

(26) Alberty, R. A.; Gehrig, C. A. *Journal of physical and chemical reference data* **1985**, *14*, 803.

(27) Toch, K.; Thybaut, J.; Marin, G. *Applied Catalysis A: General* **2015**, *489*, 292.

(28) Green, D. W.; Perry, R., H. *Perry's chemical engineers' handbook*; McGraw-hill: New York, 2008.

(29) Carrero, C. A.; Keturakis, C. J.; Orrego, A.; Schomäcker, R.; Wachs, I. E. *Dalton Transactions* **2013**, *42*, 12644.

(30) Lee, J.; Burt, S. P.; Carrero, C. A.; Alba-Rubio, A. C.; Ro, I.; O'Neill, B. J.; Kim, H. J.; Jackson, D. H.; Kuech, T. F.; Hermans, I. *Journal of Catalysis* **2015**, *330*, 19.

(31) Tang, C.-W.; Wang, C.-B.; Chien, S.-H. *Thermochim Acta* **2008**, *473*, 68.

(32) Keely, W.; Maynor, H. W. *Journal of Chemical and Engineering Data* **1963**, *8*, 297.

(33) Makhlouf, M. T.; Abu-Zied, B. M.; Mansoure, T. H. *Journal of Nanoparticles* **2013**, *2013*, 1.

(34) Greenwood, N. N.; Earnshaw, A. *Chemistry of the Elements*; Butterworth-Heinemann: Oxford, 1997.

(35) Xu, Z.; Chada, J. P.; Zhao, D.; Carrero, C. A.; Kim, Y. T.; Rosenfeld, D. C.; Rogers, J. L.; Rozeveld, S. J.; Hermans, I.; Huber, G. W. *ACS Catalysis* **2016**, *6*, 3815.

(36) Chauvin, Y.; Commereuc, D.; Hugues, F.; Thivolle-cazat, J. *Applied Catalysis* **1988**, *42*, 205.

(37) Xu, Z. R.; Zhao, D. T.; Chada, J. P.; Rosenfeld, D. C.; Rogers, J. L.; Hermans, L.; Huber, G. W. *Journal of Catalysis* **2017**, *354*, 213.

(38) He, Q. G.; Li, Q.; Khene, S.; Ren, X. M.; Lopez-Suarez, F. E.; Lozano-Castello, D.; Bueno-Lopez, A.; Wu, G. *J Phys Chem C* **2013**, *117*, 8697.

(39) Jin, H.; Wang, J.; Su, D.; Wei, Z.; Pang, Z.; Wang, Y. *J Am Chem Soc* **2015**, *137*, 2688.

(40) Liang, Y.; Li, Y.; Wang, H.; Zhou, J.; Wang, J.; Regier, T.; Dai, H. *Nat Mater* **2011**, *10*, 780.

(41) Wang, G. H.; Cao, Z.; Gu, D.; Pfander, N.; Swertz, A. C.; Spliethoff, B.; Bongard, H. J.; Weidenthaler, C.; Schmidt, W.; Rinaldi, R.; Schuth, F. *Angewandte Chemie* **2016**, *55*, 8850.

(42) Amadou, J.; Chizari, K.; Houllé, M.; Janowska, I.; Ersen, O.; Bégin, D.; Pham-Huu, C. *Catalysis Today* **2008**, *138*, 62.

(43) van Dommele, S.; Romero-Izquirdo, A.; Brydson, R.; de Jong, K. P.; Bitter, J. H. *Carbon* **2008**, *46*, 138.

(44) Stöhr, B.; Boehm, H. P.; Schlögl, R. *Carbon* **1991**, *29*, 707.

(45) Belz, T.; Baue, A.; Find, J.; Günter, M.; Herein, D.; Möckel, H.; Pfänder, N.; Sauer, H.; Schulz, G.; Schütze, J.; Timpe, O.; Wild, U.; Schlögi, R. *Carbon* **1998**, *36*, 731.

(46) Arrigo, R.; Schuster, M. E.; Wrabetz, S.; Girgsdies, F.; Tessonnier, J. P.; Centi, G.; Perathoner, S.; Su, D. S.; Schlogl, R. *ChemSusChem* **2012**, *5*, 577.

(47) Arrigo, R.; Wrabetz, S.; Schuster, M. E.; Wang, D.; Villa, A.; Rosenthal, D.; Girsgdies, F.; Weinberg, G.; Prati, L.; Schlogl, R.; Su, D. S. *Physical chemistry chemical physics:* **2012**, *14*, 10523.

(48) Arrigo, R.; Havecker, M.; Wrabetz, S.; Blume, R.; Lerch, M.; McGregor, J.; Parrott, E. P.; Zeitler, J. A.; Gladden, L. F.; Knop-Gericke, A.; Schlogl, R.; Su, D. S. *Journal of the American Chemical Society* **2010**, *132*, 9616.

(49) Chizari, K.; Vena, A.; Laureritius, L.; Sundararaj, U. *Carbon* **2014**, *68*, 369.

(50) He, Q.; Li, Q.; Khene, S.; Ren, X.; López-Suárez, F. E.; Lozano-Castelló, D.; Bueno-López, A.; Wu, G. *The Journal of Physical Chemistry C* **2013**, *117*, 8697.

(51) Gong, K.; Du, F.; Xia, Z.; Durstock, M.; Dai, L. *Science* **2009**, *323*, 760.

(52) Qu, L.; Liu, Y.; Baek, J. B.; Dai, L. *ACS nano* **2010**, *4*, 1321.

(53) Su, Y.; Zhu, Y.; Jiang, H.; Shen, J.; Yang, X.; Zou, W.; Chen, J.; Li, C. *Nanoscale* **2014**, *6*, 15080.

(54) Arrigo, R.; Schuster, M. E.; Xie, Z. L.; Yi, Y. M.; Wowsnick, G.; Sun, L. L.; Hermann, K. E.; Friedrich, M.; Kast, P.; Havecker, M.; Knop-Gericke, A.; Schlogl, R. *ACS Catalysis* **2015**, *5*, 2740.

(55) Chen, L.; Wang, H. B.; Liu, C. Z.; Liu, X. C.; Xing, S. X. *J Alloy Compd* **2016**, *656*, 622.

(56) Ravel, B.; Newville, M. *Journal of synchrotron radiation* **2005**, *12*, 537.

(57) Collins, J.; Ngo, T.; Qu, D.; Foster, M. *Carbon* **2013**, *57*, 174.

(58) Worsley, K. A.; Kalinina, I.; Bekyarova, E.; Haddon, R. C. *Journal of the American Chemical Society* **2009**, *131*, 18153.

(59) Hu, H.; Zhao, B.; Itkis, M. E.; Haddon, R. C. *The Journal of Physical Chemistry B* **2003**, *107*, 13838.

(60) ShamsiJazeyi, H.; Kaghazchi, T. *J Ind Eng Chem* **2010**, *16*, 852.

(61) Yang, G.; Chen, H. L.; Qin, H. D.; Feng, Y. J. *Appl Surf Sci* **2014**, *293*, 299.

(62) Wang, X. Q.; Liu, C. G.; Neff, D.; Fulvio, P. F.; Mayes, R. T.; Zhamu, A.; Fang, Q.; Chen, G. R.; Meyer, H. M.; Jang, B. Z.; Dai, S. *Journal of Materials Chemistry A* **2013**, *1*, 7920.

(63) Munnik, P.; de Jongh, P. E.; de Jong, K. P. *Journal of the American Chemical Society* **2014**, *136*, 7333.

(64) Borg, Ø.; Walmsley, J. C.; Dehghan, R.; Tanem, B. S.; Blekkan, E. A.; Eri, S.; Rytter, E.; Holmen, A. *Catalysis letters* **2008**, *126*, 224.

(65) Wang, J.; Zhou, J.; Hu, Y.; Regier, T. *Energy & Environmental Science* **2013**, *6*, 926.

(66) Jansen, R. J. J.; van Bekkum, H. *Carbon* **1995**, *33*, 1021.

(67) Stańczyk, K.; Dziembaj, R.; Piwowarska, Z.; Witkowski, S. *Carbon* **1995**, *33*, 1383.

(68) Pels, J. R.; Kapteijn, F.; Moulijn, J. A.; Zhu, Q.; Thomas, K. M. *Carbon* **1995**, *33*, 1641.

(69) Boudou, J. P.; Chehimi, M.; Broniek, E.; Siemieniewska, T.; Bimer, J. *Carbon* **2003**, *41*, 1999.

(70) Buckley, A. N. *Fuel Processing Technology* **1994**, *38*, 165.

(71) Fustin, C. A.; Gouttebaron, R.; De Nadai, C.; Caudano, R.; Zerbetto, F.; Leigh, D. A.; Rudolf, P. *Surf Sci* **2001**, *474*, 37.

(72) Gabriel, G.; Sauthier, G.; Fraxedas, J.; Moreno-Mañas, M.; Martínez, M. T.; Miravitlles, C.; Casabó, J. *Carbon* **2006**, *44*, 1891.

(73) Batich, C. D.; Donald, D. S. *Journal of the American Chemical Society* **1984**, *106*, 2758.

(74) Kapteijn, F.; Moulijn, J. A.; Matzner, S.; Boehm, H. P. *Carbon* **1999**, *37*, 1143.

(75) Graupner, R.; Abraham, J.; Vencelová, A.; Seyller, T.; Hennrich, F.; Kappes, M. M.; Hirsch, A.; Ley, L. *Phys. Chem. Chem. Phys.* **2003**, *5*, 5472.

(76) Arrigo, R.; Havecker, M.; Schlogl, R.; Su, D. S. *Chemical communications* **2008**, 4891.

(77) Liu, Z. Q.; Cheng, H.; Li, N.; Ma, T. Y.; Su, Y. Z. *Adv Mater* **2016**, *28*, 3777.

(78) Schultz, R. G. *Journal of Catalysis* **1967**, *7*, 286.

(79) Chakarova, K.; Hadjiivanov, K. *Microporous and Mesoporous Materials* **2009**, *123*, 123.

(80) Liang, Y.; Li, Y.; Wang, H.; Zhou, J.; Wang, J.; Regier, T.; Dai, H. *Nat Mater* **2011**, *10*, 780.

(81) Jin, H.; Wang, J.; Su, D.; Wei, Z.; Pang, Z.; Wang, Y. *Journal of the American Chemical Society* **2015**, *137*, 2688.

(82) Shen, W.; Fan, W. *J. Mater. Chem. A* **2013**, *1*, 999.

(83) Andrady, A. L.; Neal, M. A. *Philos Trans R Soc Lond B Biol Sci* **2009**, *364*, 1977.

(84) Robards, M. D.; Gould, P. J.; Piatt, J. F. In *Marine Debris*; Springer: New York, 1997, p 71.

(85) Bridgwater, A. V. *Biomass and Bioenergy* **2012**, *38*, 68.

(86) Xue, Y.; Zhou, S.; Brown, R. C.; Kelkar, A.; Bai, X. L. *Fuel* **2015**, *156*, 40.

(87) Paulsen, A. D.; Mettler, M. S.; Dauenhauer, P. J. *Energ Fuel* **2013**, *27*, 2126.

(88) Czernik, S.; Bridgwater, A. V. *Energ Fuel* **2004**, *18*, 590.

(89) Vispute, T. P.; Zhang, H.; Sanna, A.; Xiao, R.; Huber, G. W. *Science* **2010**, *330*, 1222.

(90) Wright, M. M.; Daugaard, D. E.; Satrio, J. A.; Brown, R. C. *Fuel* **2010**, *89*, S2.

(91) FakhrHoseini, S. M.; Dastanian, M. *Journal of Chemistry* **2013**, *2013*, 1.

(92) Cozzani, V.; Nicolella, C.; Rovatti, M.; Tognotti, L. *Industrial & Engineering Chemistry Research* **1996**, *35*, 90.

(93) Ranzi, E.; Dente, M.; Faravelli, T.; Bozzano, G.; Fabini, S.; Nava, R.; Cozzani, V.; Tognotti, L. *J Anal Appl Pyrol* **1997**, *40*, 305.

(94) Kodera, Y.; McCoy, B. J. *Energ Fuel* **2002**, *16*, 119.

(95) Sanchez-Jimenez, P. E.; Perez-Maqueda, L. A.; Perejon, A.; Criado, J. M. *Polym Degrad Stabil* **2010**, *95*, 733.

(96) Staggs, J. E. J. *Polym Degrad Stabil* **2004**, *85*, 759.

(97) Yang, H. P.; Coolman, R.; Karanjkar, P.; Wang, H. Y.; Dornath, P.; Chen, H. P.; Fan, W.; Conner, W. C.; Mountziaris, T. J.; Huber, G. *Green Chemistry* **2017**, *19*, 286.

(98) Williams, P. T.; Williams, E. A. *J Anal Appl Pyrol* **1999**, *51*, 107.

(99) Conesa, J. A.; Font, R.; Marcilla, A.; Garcia, A. N. *Energ Fuel* **1994**, *8*, 1238.

(100) Scott, D. S.; Czernik, S. R.; Piskorz, J.; Radlein, D. S. G. *Energ Fuel* **1990**, *4*, 407.

(101) Kaminsky, W. *J Anal Appl Pyrol* **1985**, *8*, 439.

(102) Encinar, J. M.; Gonzalez, J. F. *Fuel Processing Technology* **2008**, *89*, 678.

(103) Ceranic, M.; Kosanic, T.; Djuranovic, D.; Kaludjerovic, Z.; Djuric, S.; Gojkovic, P.; Bozickovic, R. *J Renew Sustain Ener* **2016**, *8*.

(104) Khairuddin; Pramono, E.; Utomo, S. B.; Wulandari, V.; Zahrotul, A.; Clegg, F. *J Phys Conf Ser* **2016**, *776*, 012054.

(105) Hernández, M. d. R.; García, Á. N.; Marcilla, A. *J Anal Appl Pyrol* **2005**, *73*, 314.

(106) Routray, K.; Barnett, K. J.; Huber, G. W. *Energy Technology* **2017**, *5*, 80.

(107) Wallis, M. D.; Bhatia, S. K. *Polym Degrad Stabil* **2007**, *92*, 1721.

(108) Pacáková, V.; Leclercq, P. A. *Journal of Chromatography A* **1991**, *555*, 229.

(109) Cypres, R. *Fuel Processing Technology* **1987**, *15*, 1.

(110) Depeyre, D.; Flicoteaux, C.; Chardaire, C. *Industrial & Engineering Chemistry Process Design and Development* **1985**, *24*, 1251.

(111) Seeger, M.; Cantow, H. J. *Die Makromolekulare Chemie* **1975**, *176*, 1411.

(112) Seeger, M.; Gritter, R. J. *Journal of Polymer Science: Polymer Chemistry Edition* **1977**, *15*, 1393.

(113) Bruns, M. C.; Koo, J. H.; Ezekoye, O. A. *Polym Degrad Stabil* **2009**, *94*, 1013.

(114) Miranda, R.; Yang, J.; Roy, C.; Vasile, C. *Polym Degrad Stabil* **1999**, *64*, 127.

(115) Sánchez-Jiménez, P. E.; Pérez-Maqueda, L. A.; Perejón, A.; Pascual-Cosp, J.; Benítez-Guerrero, M.; Criado, J. M. *Cellulose* **2011**, *18*, 1487.

(116) Peterson, J. D.; Vyazovkin, S.; Wight, C. A. *Macromolecular Chemistry and Physics* **2001**, *202*, 775.

(117) Grassie, N.; Scott, G. *Polymer degradation and stabilisation*; Cambridge University Press: Cambridge, 1985.

(118) Akaike, H. *Engineering Technology & Applied Sciences* **1981**, 22.

(119) Aho, K.; Derryberry, D.; Peterson, T. *Ecology* **2014**, *95*, 631.

(120) Posada, D.; Buckley, T. R. *Systematic biology* **2004**, *53*, 793.

(121) Mazerolle, M. J. *Amphibia-Reptilia* **2006**, *27*, 169.

(122) Pan, W. *Biometrics* **2001**, *57*, 120.

(123) Bozdogan, H. *J Math Psychol* **2000**, *44*, 62.

(124) Burnham, K. P.; Anderson, D. R. *Model Selection and Multimodel Inference: A Practical Information - Theoretical Approach*; Springer-Verlag New York Inc., 2002.

(125) Vyazovkin, S.; Wolfgang;, L. *International Reviews in Physical Chemistry* **1995**, *14*, 355.

(126) Kelen, T. *Polymer Degradation*; Van Nostrand Reinhold Company: New York 1983.

(127) Schnabel, W. *Polymer Degradation: Principles and Prac-tical Applications*; Macmillan: New York, 1981.

(128) Reich, L.; Stivala, S. S. *Elements of Polymer Degradation*; McGraw-Hill: New York, 1971.

(129) Madorsky, S. L. *Thermal Degradation of Organic Polymers*; Interscience Publishers: New York, 1964.

(130) Jordan, K. J.; Suib, S. L. *Journal of Polymer Science Part A: Polymer Chemistry* **2000**, *38*, 3690.

(131) Odian, G. *Principles of Polymerization*; John Wiley & Sons, Inc.: New York, 2004.

(132) De Witt, M. J.; Dooling, D. J.; Broadbelt, L. J. *Industrial & Engineering Chemistry Research* **2000**, *39*, 2228.

(133) McCaffrey, W. C.; Cooper, D. G.; Kamal, M. R. *Polym Degrad Stabil* **1998**, *62*, 513.

(134) Scheirs, J.; Kaminsky, W. In *Feedstock Recycling and Pyrolysis of Waste Plastics: Converting Waste Plastics into Diesel and Other Fuels*; John Wiley & Sons, Ltd: Hoboken, 2006, p 435.

(135) Demirbas, A. *J Anal Appl Pyrol* **2004**, *72*, 97.

(136) Buekens, A. G.; Huang, H. *Resources, Conservation and Recycling* **1998**, *23*, 163.

(137) Joo, H. S.; Guin, J. A. *Fuel Processing Technology* **1998**, *57*, 25.

(138) Simon, C. M.; Kaminsky, W.; Schlesselmann, B. *J Anal Appl Pyrol* **1996**, *38*, 75.

(139) de Klerk, A. *Energ Fuel* **2006**, *20*, 1799.

(140) Tobisch, S.; Ziegler, T. *Journal of the American Chemical Society* **2004**, *126*, 9059.

(141) Breuil, P. A. R.; Magna, L.; Olivier-Bourbigou, H. *Catalysis letters* **2015**, *145*, 173.

(142) Zhao, D.; Xu, Z.; Chada, J. P.; Carrero, C. A.; Rosenfeld, D. C.; Rogers, J. L.; Hermans, I.; Huber, G. W. *ACS Catalysis* **2017**, *7*, 7479.

(143) Sadef, Y.; Nizami, A. S.; Batool, S. A.; Chaudary, M. N.; Ouda, O. K. M.; Asam, Z. Z.; Habib, K.; Rehan, M.; Demirbas, A. *Energ Source Part B* **2016**, *11*, 569.

(144) Miandad, R.; Barakat, M. A.; Aburiazaiza, A. S.; Rehan, M.; Nizami, A. S. *Process Safety and Environmental Protection* **2016**, *102*, 822.

(145) Achilias, D. S.; Roupakias, C.; Megalokonomos, P.; Lappas, A. A.; Antonakou, E. V. *Journal of hazardous materials* **2007**, *149*, 536.

(146) Miskolczi, N.; Angyal, A.; Bartha, L.; Valkai, I. *Fuel Processing Technology* **2009**, *90*, 1032.

(147) Whyte, H. E.; Loubar, K.; Awad, S.; Tazerout, M. *Fuel Processing Technology* **2015**, *140*, 32.

(148) Miskolczi, N.; Ates, F.; Borsodi, N. *Bioresource technology* **2013**, *144*, 370.

(149) Lopez, A.; de Marco, I.; Caballero, B. M.; Laresgoiti, M. F.; Adrados, A.; Torres, A. *Waste management (New York, N.Y.)* **2011**, *31*, 1973.

(150) Chen, D.; Yin, L.; Wang, H.; He, P. *Waste management (New York, N.Y.)* **2014**, *34*, 2466.

(151) Lee, K.-H. *J Anal Appl Pyrol* **2012**, *94*, 209.